JYU DISSERTATIONS 393

Sari Romppanen

Laser-Spectroscopic Studies of Rare Earth Element- and Lithium-Bearing Minerals and Rocks

UNIVERSITY OF JYVÄSKYLÄ
FACULTY OF MATHEMATICS
AND SCIENCE

JYU DISSERTATIONS 393

Sari Romppanen

Laser-Spectroscopic Studies of Rare Earth Element- and Lithium-Bearing Minerals and Rocks

Esitetään Jyväskylän yliopiston matemaattis-luonnontieteellisen tiedekunnan suostumuksella
julkisesti tarkastettavaksi kesäkuun 14. päivänä 2021 kello 12.

Academic dissertation to be publicly discussed, by permission of
the Faculty of Mathematics and Science of the University of Jyväskylä,
on June 14, 2021 at 12 o'clock.

JYVÄSKYLÄN YLIOPISTO
UNIVERSITY OF JYVÄSKYLÄ

JYVÄSKYLÄ 2021

Editors
Saara Kaski
Department of Chemistry, University of Jyväskylä
Päivi Vuorio
Open Science Centre, University of Jyväskylä

ISBN 978-951-39-8689-6 (PDF)
URN:ISBN:978-951-39-8689-6
ISSN 2489-9003

Permanent link to this publication: http://urn.fi/URN:ISBN:978-951-39-8689-6

ABSTRACT

Romppanen, Sari
Laser-spectroscopic studies of rare earth element- and lithium-bearing minerals and rocks
Jyväskylä: University of Jyväskylä, 2021, 66 p.
(JYU Dissertations
ISSN 2489-9003; 393)
ISBN 978-951-39-8689-6

This thesis is an interdisciplinary work, that forms a link between laser-spectroscopic and physical chemistry research to traditional geochemistry and mineralogy. The three laser-spectroscopic methods – laser-induced breakdown spectroscopy (LIBS), Raman spectroscopy, and laser-induced luminescence spectroscopy – are applied to analyse of the rare earth element (REE) and lithium-bearing mineral and rock samples collected from the European Union (EU) region. REEs and lithium were chosen as the scope of the study due to their importance to modern society and industry. The EU has determined these are critical raw materials due to their economic importance and supply risk from the EU's perspective.

The laser-spectroscopic methods presented here provide valuable information about minerals. LIBS produces a characteristic elemental emission spectrum from the mineral surface and detects all elements of the periodic table, including light and non-conductive elements. Thus, it is also very suitable for analysing precious lithium. Molecular structures and, thus, mineralogical information can be achieved with time-gated-Raman spectroscopy, which is also suitable for detecting luminescent minerals. The third compelling technique, laser-induced luminescence spectroscopy, reveals the minerals' luminescence activators occurring even in very small concentrations. Rare earth elements can commonly act as luminescence activators.

The most important characteristics of all these methods are rapid measurement time, minor (or lack of) sample preparation, the possibility of measuring solid samples, and less expensive equipment required when compared with many other techniques. Thus, all these techniques are highly suited to *in situ* and on-line measurement purposes, which was kept in mind while designing the analysis setups in the laboratory and the efficient data handlings.

Keywords: laser-induced breakdown spectroscopy, LIBS, Raman spectroscopy, laser-induced luminescence, time-resolving, rare earth elements, REE, lithium

TIIVISTELMÄ (ABSTRACT IN FINNISH)

Romppanen, Sari
Laser-spektroskopia harvinaisia maametalleja ja litiumia sisältävien mineraalien ja kivien määrityksessä
Jyväskylä: University of Jyväskylä, 2021, 66 p.
(JYU Dissertations
ISSN 2489-9003; 393)
ISBN 978-951-39-8689-6

Tämä väitöskirja on osa poikkitieteellistä tutkimusprojektia, jossa geokemiallisessa ja mineralogisessa tutkimuksessa hyödynnettiin laser-spektroskopian ja fysikaalisen kemian analyysimenetelmiä. Työssä käytettiin pääasiassa kolmea laser-spektroskopian menetelmää: laser-indusoitua plasmaspektroskopiaa (LIBS), aikaerotteista Raman-spektroskopiaa sekä laser-indusoitua luminesenssispektroskopiaa analysoitaessa harvinaisia maametalleja ja litiumia sisältäviä mineraali- ja kivinäytteitä. Harvinaiset maametallit ja litium on määritelty Euroopan Unionin näkökulmasta kriittisiksi alkuaineiksi tarpeellisuutensa ja saatavuusriskinsä vuoksi. Siksi ne ovatkin hyvin ajankohtainen tutkimuskohde ja näytteet on valikoitu kiinnostavista eurooppalaisista mineraaliesiintymistä.

Laser-spektroskopian tutkimustulokset antavat erilaista tietoa mineraaleista. LIBS-emissiospektri paljastaa mineraalin alkuainekoostumuksen ja se määrittää myös kevyet alkuaineet. Tämän vuoksi LIBS soveltuukin erinomaisesti myös litiummineraalien analysointiin. Aikaerotteinen Raman-spektroskopia tunnistaa myös luminesoivat mineraalit molekyylirakenteidensa perusteella. Laser-indusoitu luminesenssispektroskopia paljastaa hyvinkin pieninä pitoisuuksina olevat luminesenssin aktivaattorialkuaineet, joina harvinaiset maametallit hyvin yleisesti esiintyvät.

Laser-spektroskopia soveltuu erinomaisesti paikan päällä (*in situ*) tai linjastolla (on-line) tehtäviin mittauksiin, koska mittausaika on nopea ja näytekäsittely on minimaalista. Analyysi voidaan siksi tehdä suoraan mineraalin tai kiven pinnasta. Laser-spektroskopian laitteistot ovat myös halvempia verrattuna moniin muihin analyysilaitteistoihin. Nämä ominaisuudet ovatkin huomioitu myös tämän tutkimusprojektin laitteistojen suunnittelussa ja analyysitiedon käsittelyssä, jotta saatuja tuloksia voitaisiin mahdollisesti jatkojalostaa tästä eteenpäin.

Avainsanat: laser-indusoitu plasmaspektroskopia, LIBS, Raman-spektroskopia, laser-indusoitu luminesenssi, aikaerotteisuus, harvinaiset maametallit, REE litium

Author
Sari Romppanen
Department of Chemistry
Nanoscience Center
University of Jyväskylä
sari.romppanen@jyu.fi

Supervisor
Dr. Saara Kaski
Department of Chemistry
University of Jyväskylä
Finland

Co-supervisor
Dr. Heikki Häkkänen
Department of Biological and Environmental Science
University of Jyväskylä
Finland

Reviewers
Adj. Assoc. Prof. Russell Harmon
Department of Marine, Earth, and Atmospheric Sciences
North Carolina State University
United States

Adj. Prof. Mika Lastusaari
Department of Chemistry
University of Turku
Finland

Opponent
Prof. Michael Gaft
Department of Physics
Ariel University
Israel

PREFACE

The work presented here was performed at the Department of Chemistry of the University of Jyväskylä from 2014–2021; the experimental research was carried out in the Nanoscience Center Laser-Laboratory (Laserlab-NSC) facilities. Financial support by the Academy of Finland, the University of Jyväskylä, and the K. H. Renlund Foundation for this project is greatly appreciated. Several travelling possibilities to conferences and courses were enabled by the financial support achieved from many sources: The Erasmus+ mobility project, The Finnish Society of Sciences and Letters (The Sohlberg delegation), The International Union of Crystallography (IUCr), The European Mineralogical Union (EMU), and The Società Italiana di Mineralogia e Petrologia. These allowed me to educate myself, share my research, and create valuable contacts, and I am deeply thankful for them.

I want to express my deepest gratitude to my supervisor, Dr. Saara Kaski: Your guidance, encouragement, and, most of all, your patience, seemed to be inexhaustible resources. You are truly an inspiration, and I am thankful for everything. I am also sincerely grateful for co-supervisor Dr. Heikki Häkkänen: I truly admire your knowledge and enthusiasm about spectroscopy. Thank you for teaching me so much. I have been privileged to able to work with both of you during these years, and I am hopeful that it will still be possible for us to do science together.

I want to thank the reviewers of this thesis, Adj. Assoc. Prof. Russell Harmon from the North Carolina State University and Adj. Prof. Mika Lastusaari from the University of Turku, for their valuable feedback on this thesis. I would also like to express my appreciation for all the co-authors of the original publications for their contribution. I have learned so much from various fields of science during this interdisciplinary project. I also want to thank my former and current co-workers, at the Department of Chemistry and the Nanoscience Center for a great and inspiring working place and for their peer support during tough times. I am also grateful for my former co-workers and contacts from the geoscientific world who have helped me during this project.

I am privileged to have so many wonderful people in my life whom I have been lucky to be acquainted with during different steps of my life. I am thankful for my friends' support and, most of all, for giving me something else to think about than the scientific stuff. Additionally, I wish to extend my warmest thanks to my family, especially: *Äiti, kiitos kaikesta tuestasi*. Most of all thanks to my husband Ari, who has been always there for me; this immense work would not have been possible without your encouragement and support. And last, but most importantly, I am grateful for my beloved son Eino just for being such a marvelous boy.

Salo, April 2021,
Sari Romppanen

LIST OF ORIGINAL PUBLICATIONS

This thesis is based on the publications and a manuscript listed below. They are referred to by their Roman numerals (I–IV) in the following text.

I Sari Romppanen, Heikki Häkkänen & Saara Kaski, Singular value decomposition approach to the yttrium occurrence in mineral maps of rare earth element ores using laser-induced breakdown spectroscopy, Spectrochimica Acta Part B: Atomic Spectroscopy, **2017**, 134, 69–74.

II Sari Romppanen, Ilkka Pölönen, Heikki Häkkänen & Saara Kaski, Optimization of spodumene identification by statistical approach for laser-induced breakdown spectroscopy data of lithium-pegmatites, **2021**, *manuscript*.

III Sari Romppanen, Heikki Häkkänen, Jere Kekkonen, Jan Nissinen, Ilkka Nissinen, Juha Kostamovaara & Saara Kaski, Time-gated Raman and laser-induced breakdown spectroscopy in mapping of eudialyte and catapleiite, Journal of Raman Spectroscopy, **2020**, 51, 1462–1469.

IV Sari Romppanen, Heikki Häkkänen & Saara Kaski, Laser-induced time-resolved luminescence in analysis of rare earth elements in apatite and calcite, Journal of Luminescence, **2021**, 233.

The author has performed most of the spectroscopic measurements in papers I, II, and IV and had a major role in the data analysis and data handlings in papers II, III, and III. She wrote the first drafts of papers II, III, and IV and participated in writing paper I.

ABBREVIATIONS

CCD	Charge-coupled device
CF-LIBS	Calibration-free LIBS
CNMMN	The Commission of New Mineral and Mineral Names
CNMNC	The Commission on New Minerals, Nomenclature and Classification
CMOS	Complementary-metal-oxide semiconductor
CRM	Critical raw materials
CW	Continuous wave
EDS	Energy dispersive spectrometer
EPMA	Electron probe microanalyzer
EU	The European Union
FTIR	Fourier transform infrared absorption
pXRF	Field-portable X-ray fluorescence
HREE	Heavy rare earth element
ICCD	Intensified charge-coupled device
ICP-MS	Inductively coupled plasma mass spectrometry
ICP-AES	Inductively coupled plasma atomic emission spectrometry
ICP-OES	Inductively coupled plasma optical emission spectroscopy
IMA	International Mineralogical Association
IR	Infrared
IUPAC	The International Union of Pure and Applied Chemistry
LA-ICP-MS	Laser ablation inductively coupled plasma mass spectrometry
LIF	Laser-induced fluorescence
LIBS	Laser-induced breakdown spectroscopy
LREE	Light rare earth element
MREE	Medium rare earth element
Mt	Million tons
NAA	Neutron activation analysis
PCA	Principal component analysis
PDA	Photodiode array
PL	Photoluminescence
ppb	Parts per billion
ppm	Parts per million
REE	Rare earth element
REM	Rare earth metal
REO	Rare earth element oxide
SPAD	Single-photon avalanche diode
SVD	Singular value decomposition
UV	Ultraviolet
VCA	Vertex component analysis
wt%	Weight percent
XRD	X-ray diffraction
XRF	X-ray fluorescence

CONTENTS

1 INTRODUCTION

The aim of this work is to present both the suitability and the different ways of utilising three time-resolved laser-spectroscopic methods – laser-induced breakdown spectroscopy (LIBS), laser-induced luminescence spectroscopy, and Raman spectroscopy – to analyse the natural rare earth element (REE) and lithium-bearing ore minerals from the European region. REEs and lithium have been determined to be critical raw elements from the European Union's (EU's) perspective due to their economic importance and supply risk.[1] These elements are a topical research target at this moment for this reason. The term *ore* is very important to assimilate when raw materials are discussed, and it was already specified in 1909 by J. F. Kemp:

> "Ore is a metalliferous mineral, or an aggregate of metalliferous minerals, more or less mixed with gangue, which from the standpoint of the miner can be won at a profit, or from the standpoint of the metallurgist can be treated at a profit. The test of yielding a metal or metals at a profit seems to be the only feasible one to employ."[2]

This means that not only are metal-containing minerals specified as ore minerals but also that metal(s) must be extracted cost effectively. Metals are extracted from ores in beneficiation processes to produce raw materials for industrial uses. The recent definitions of the term ore also include utilisation of industrial minerals.[3] An industrial mineral is a non-metallic and non-fuel mineral with economic value.[4] Profitable and minable ore units are called oreshoots, orebodies, deposits, or ore reserves, while gangue means unwanted minerals or rock. Grade (the concentration of metal) and tonnage are the key factors in evaluating if the mineral deposit is an economic ore deposit. The homogeneity of the deposit is more important than its grade in the case of a non-metallic industrial mineral deposit. There are also other significant factors when specifying ore deposits, including possible by-products, metal prices, mineralogical form, undesirable substances, location, size and shape of the deposit, ore character, grain size and shape, and some environmental, political and cash flow affects.[3]

Different geological, geochemical, and geophysical methods are used in exploration, *i.e.*, in locating mineral and rock resources that then can be evaluated

and possibly exploited if it is profitable. The mining process extracts the ore from the ground and transports it to a mill. Ore minerals are separated from gangue at the mill, and concentrate is formed. This is taken to a smelter, where metals are extracted. This procedure is typically simpler in the case of industrial minerals.[3]

Laser-spectroscopic analysis can offer a way to analyse mineral-based samples of different kinds during the different steps of mineral exploration, mining, and processing. Exploration is performed in field circumstances, and it would be cost efficient to have a technique that could estimate the metal contents already *in situ*. It is essential in mining to reduce the waste rock amount and ensure the mineralogical and chemical contents of the minable ore units already at the mine site. It is important during mineral processing to be able to monitor the efficiency and quality of the processed products of the mill and smelter; an option for on-line analysis would be an asset. Laser-spectroscopic tools could offer a great option for all these processes. This thesis studies the possibilities of using these techniques in several ways for mineral analysis with a focus on the detection of REEs and lithium.

1.1 Minerals and rocks

The basis of the Earth's solid surface is in the arrangements of ions, atoms, or ionic groups held up by different chemical bonds. More precisely can be said that anions (negative-charged ion) and cations (positive-charged ion) in specific ratios construct minerals. One or more mineral(s) form a rock, and rocks build up the solid bedrock (Fig. 1). Soil occurs above the bedrock.[5]

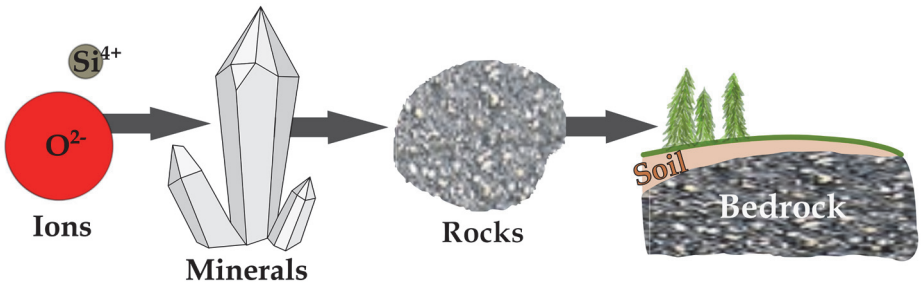

FIGURE 1. A formation process of bedrock from rocks, rocks from minerals, and minerals from ions.

The Earth's topmost layer until the mantle border in Mohorovičić discontinuity is called the crust. The Earth's oceanic crust is mainly basaltic and rather thin (~7 km), whereas continental crust is thicker (~40 km) and contains various rock types.[6] Silicon is the most abundant element in the continental crust after oxygen, and the crustal rocks and inorganic matter of soil are mainly composed of silicon rich silicate minerals (~95%).[7] Rock-forming elements represent the majority of the continental crust (Fig. 2). Rock/mineral analysis typically expresses the

contents of elements in percentage levels, commonly as wt% (weight percent) of oxides.[6,8] The trace element levels in rocks/minerals is less than 0.1 wt%.[9]

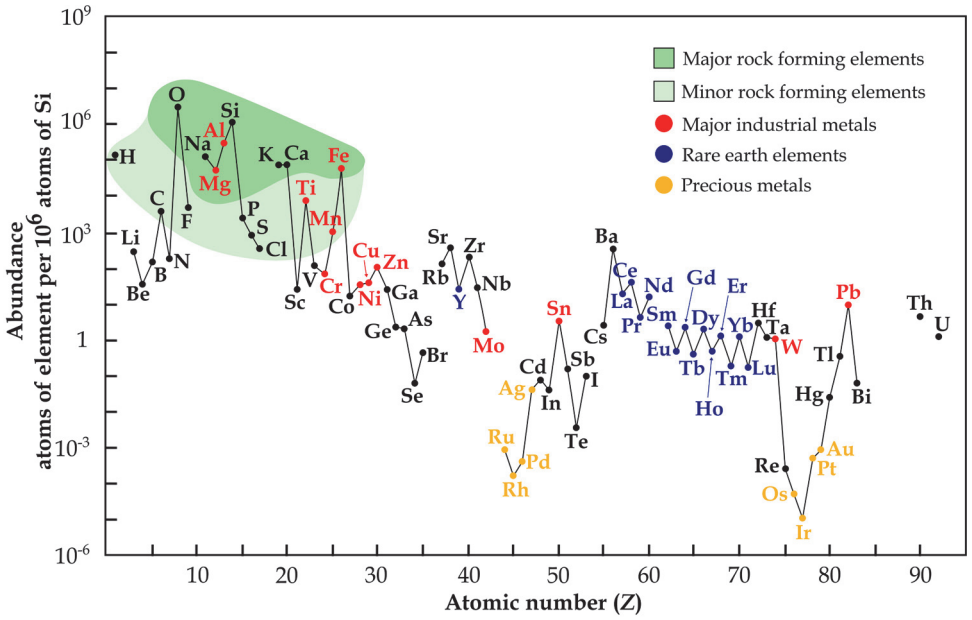

FIGURE 2. The abundance of elements related to the silicon in the Earth's upper continental crust. Major industrial elements are presented as elements with global production over 3×10^7 kg/year. Missing elements have no long-living or stable isotopes. Figure is modified from Ref.[10].

The Commission of New Mineral and Mineral Names (CNMMN) [a] of the International Mineralogical Association (IMA) define the term mineral as:

> "an element or chemical compound that is normally crystalline and that has been formed as a result of geological processes."[11]

CNMNC maintains and amplifies a list of recognised minerals, which consisted of 5688 minerals in March 2021.[12] There is a special procedure with guidelines, presented elsewhere, for identifying and accepting the minerals on this list.[13]

The mineral's chemical composition can be presented as a mineral formula. A mineral's structural arrangement is represented in structural formula as a minimum number of symmetrically different sites, *i.e.*, points, that an atom can occupy (or possibly occupy) in a unit cell.[14] A formula unit is not always the same as a general formula; these are $MgSiO_3$ and $Mg_2Si_2O_6$ for enstatite mineral, respectively. The general formula emphasises that there are two crystallographic sites for Mg in the enstatite mineral structure.[14] Trace elements are not presented in a mineral's formula and occur in minor amounts.[9] The occurrences and levels of the trace elements are mostly based on ionic radii and ionic charge: For

[a] In 2006, two commissions of the IMA – the Commission of New Mineral and Mineral Names (CNMMN) and the Commission on Classification of Minerals (CCM) – were joined together as the Commission on New Minerals, Nomenclature and Classification (CNMNC).[160]

example, Ni^{2+} has the same possibility as the similar-sized ion Mg^{2+} to enter into Mg-silicate minerals. Thus, these can typically contain small amounts of nickel.[15] Crystal structure and availability of chemical components during mineral crystallisation also affect the trace element content.[16,17]

Minerals can be divided into classes in several ways, *e.g.*, based on chemistry, crystal structure, association, occurrence, genetic history, or resource.[18] Many mineralogists favour the chemical classification: It refers not just to chemical composition, but it also helps to choose the most suitable analysis method for the whole mineral class simultaneously.[19] Dana classification,[20] one of the oldest, still extensively used classifications is based on work published by Dana in 1837[21]. There are also many others, such as Strunz classification[22], Strunz-Nickel classification[23], and the work of Deer, Howie & Zussman[24]. The hierarchical standardisation of mineral classification for IMA/CNMNC contains mineral class (1), mineral subclass (2), mineral family (3), mineral supergroup (4), mineral group(s) (5), and mineral subgroup / mineral series (6). Mineral classes (1) can be separated due to a main anion (*e.g.*, O^{2-}, S^{2-}), an anionic complex (*e.g.*, SO_4^{2-}, OH^-, CO_2^{2-}, PO_4^{3-} or $Si_xO_y^{z-}$) or a missing anion (native elements). The largest mineral classes include sulphides, sulphosalts, halides, oxides, hydroxides, arsenites, carbonates, nitrates, borates, sulphates, chromates, molybdates, tungstates, phosphates, arsenates, vanadates, silicates, organic compounds, and native elements. Mineral subclasses (2) are related only to silicates and borates that can be divided into neso-, soro-, cyclo-, ino-, phyllo-, and tectosilicates (or -borates) based on the bonding of $Si_xO_y^{z-}$ (or $B_xO_y^{z-}$) tetrahedra.[18] Fig. 3. shows the different silicate structures and silicon–oxygen tetrahedra bonding types.

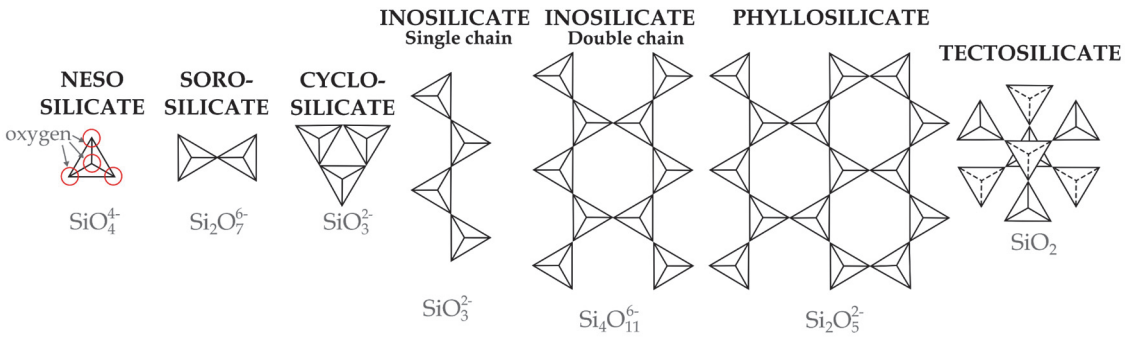

FIGURE 3. Silicate mineral structures. The SiO_4^{4-} tetrahedron has four oxygen atoms on the corners (marked with red circles) and one silicon atom in the centre. The repeat units are presented below the structural units. Tetrahedrons are pointing up, except in tectosilicate, where hexagonal tetrahedra rings on every other layer are pointing in the opposite direction. Figure is modified Ref.[9].

Similarity in mineral structure or/and chemical composition is the basis to form mineral families (3), like the feldspathoid family. A mineral supergroup (4) is formed by at least two mineral groups with structural and chemical similarities and whose members belong to the same mineral class. Mineral group (5) involves at least two minerals with same/fundamentally similar structure and chemical

composition, like eudialyte group. Minerals that are not included in mineral groups can be included in mineral subgroups/series (6).[18]

Rocks usually contain minor amounts of accessory minerals in addition to the main minerals. Studying those can reveal information about rock formation processes.[25] Minerals can also contain fluid inclusions consisting of vapor and gas trapped inside the mineral during formation. Fluid inclusions can offer information about the rock's pressure–temperature evolution.[26] Soil, however, consists of inorganic mineral material and organic matter.[27] The Finnish land area mainly consists of unsorted glacigenous soil, till, caused by several glaciations.[28]

Rocks are usually divided into three types regarding their genetic origin: igneous, sedimentary, and metamorphic rocks. Igneous rock is crystallised from magma in volcanic eruptions or in the Earth's crust or mantle. Sedimentary rock is formed from already existing rock when it is weathered, eroded, transported, deposited, buried, and, eventually, when it goes through lithification and diagenesis. Metamorphic rock is formed when a rock of any type is changed in texture, minerals, and/or structures related to exposure of high pressure or/and temperature.[8]

1.2 Critical raw materials

The European Union has presented a group of critical raw materials (CRM) that are important for modern technology and its economy. The criticality is based on its economic importance and supply risk from the EU's perspective and on the evaluation it has performed every 3rd year since 2008.[1] The newest evaluation (2020) listed 30 materials altogether as critical raw materials, including LREEs (light rare earth elements), HREEs (heavy rare elements), and lithium.[1]

1.2.1 Rare earth elements

Rare earth elements (REEs), or rare earth metals (REMs),[b] refer to the group of lanthanides, *i.e.*, lanthanoids,[c] scandium (Sc), and yttrium (Y).[29] The lanthanoids are a group of elements with atomic numbers (Z) of 57–71 (lanthanum–lutetium) (Table 1). Lanthanoids (Ln) mostly exist in oxidation state 3+, but 2+ and 4+ are also relatively common in some REEs. Europium especially tends to appear as Eu^{3+} and Eu^{2+}.[9] Ln^{III} are very similar in size and have comparable chemical properties: in nature those are found usually together.[9,30] Ionic radii are slightly decreasing from La^{3+} to Lu^{3+} (~ 0.21 Å).[9] Yttrium has an ionic radius corresponding to heavier REEs with which it usually occurs. Sc^{3+} has a smaller ionic radius and differs in chemical behaviour; thus, it is not seen in as high levels in REE minerals.[31]

[b] IUPAC prefers the term rare earth metal (REM).[29]
[c] IUPAC prefers lanthanoid over lanthanide since -ide is points to negative ions.[29]

TABLE 1 Rare earth elements and their chosen properties.[30,32,33]

Atomic number	Element	Symbol	Atomic weight[30,32]	Electron configuration[30,32]
21	Scandium	Sc	44.956	[Ar] $4s^2 3d^1$
39	Yttrium	Y	88.906	[Kr] $5s^2 4d^1$
57	Lanthanum	La	138.91	[Xe] $6s^2 5d^1$
58	Cerium	Ce	140.12	[Xe] $4f^1 6s^2 5d^1$
59	Praseodymium	Pr	140.91	[Xe] $4f^3 6s^2$
60	Neodymium	Nd	144.24	[Xe] $4f^4 6s^2$
61	Promethium	Pm		[Xe] $4f^5 6s^2$
62	Samarium	Sm	150.36	[Xe] $4f^6 6s^2$
63	Europium	Eu	151.96	[Xe] $4f^7 6s^2$
64	Gadolinium	Gd	157.25	[Xe] $4f^7 6s^2 5d^1$
65	Terbium	Tb	158.93	[Xe] $4f^9 6s^2$
66	Dysprosium	Dy	162.50	[Xe] $4f^{10} 6s^2$
67	Holmium	Ho	164.93	[Xe] $4f^{11} 6s^2$
68	Erbium	Er	167.26	[Xe] $4f^{12} 6s^2$
69	Thulium	Tm	168.93	[Xe] $4f^{13} 6s^2$
70	Ytterbium	Yb	173.04	[Xe] $4f^{14} 6s^2$
71	Lutetium	Lu	174.97	[Xe] $4f^{14} 6s^2 5d^1$

Despite the name, most of REEs are not rare in nature except for radioactive promethium. The abundance of REEs in the Earth's crust vary from the most common, cerium (66 ppm), to thulium (0.5 ppm).[30] REEs can be divided into LREEs (light earth elements) or the "cerium group", which is usually refers to elements from lanthanum to europium. HREEs (heavy rare elements) or the "yttrium group" include elements from gadolinium to lutetium and usually yttrium.[30] However, divisions are not always unambiguous together, *e.g.*, in EU reports to LREEs are listed La–Sm and to HREEs Eu–Lu.[1,9] Division can also be based on behaviour in a beneficiation process: light REEs (LREEs: La, Ce, and Nd), medium REEs (MREEs: Sm, Eu, and Gd) and heavy REEs (HREEs: Tb–Lu and Y).[34] A very common method in geochemical research is to examine the REE patterns' abundance versus atomic number (Z). The chemical data are typically normalised with chondrite (meteorite) values for this purpose to remove the zigzag pattern[9,35], which Fig. 2 also shows. Depletion or enrichment of all REEs or LREE related to HREE or positive/negative Eu is usually observed from the chondrite-normalized REE diagram.[9] For example, the author has previously detected, as documented in her Master's Thesis (Geology and mineralogy),[36] that relative REE-distribution patterns in samples of berries and a mushroom correlate to a local granitic bedrock.

The origin and REE naming are very much bound up to the Nordic countries, especially to Ytterby, a small Swedish village. Yttrium was the first one discovered by a Finnish chemist, J. Gadolin in 1797. Gadolin isolated an assumed new oxide from a mineral collected from Ytterby and it was named as yttria. However, it consisted of several metal oxides, and an yttrium oxide was isolated decades later from this mixture. Erbium, terbium, and ytterbium are also named after the Ytterby village. Gadolinium is named in honour of J. Gadolin, while

europium is named after Europe, scandium after Scandinavia, and holmium after *Holmia* (Stockholm in Latin). Most of the rare earth elements were discovered in the 19th century, but promethium was discovered much later from fission products of ^{235}U.[30]

All minerals contain REEs at some level but usually as trace elements.[35] LREEs tend to occur more in carbonates and HREEs mainly in oxides and in some phosphates. Silicates can host all REEs evenly, but due to very strong binding, extracting REEs needs much energy; thus, it is expensive.[37] Over 70 minerals are known, which include the essential concentrations of REEs. REEs can appear in high levels as in accessory or major minerals (*e.g.*, monazite, bästnasite) and concentrated on specific minerals (*e.g.*, apatite).[35] Table 2 lists the most important REE minerals in Europe; Fig. 4 presents examples of REE-bearing minerals from the Nordic countries.

TABLE 2 Main REE minerals in Europe with their chemical formulas and mineral classes (based on Dana classification[20]). The table is simplified from Ref.[38]. Mark * represents mineral group.

Mineral	General chemical formula	Mineral class
Aeschynite*	$REE(Ti,Nb)_2(O,OH)_6$	Oxide
Allanite*	$(REE,Ca)_2(Al,Fe)_3(SiO_4)\ (Si_2O_7)O(OH)$	Sorosilicate
Ancylite*	$LREE(Sr, Ca)(CO_3)_2(OH)\cdot H_2O$	Carbonate
Apatite*	$Ca_5(PO_4)_3(F,Cl,OH)$	Phosphate
Bastnäsite*	$REE(CO_3)F$	Carbonate
Britholite*	$(REE,Ca)_5(SiO_4)_3(OH,F)$	Nesosilicate
Brockite	$(Ca,Th,Ce)(PO_4)\cdot H_2O$	Phosphate
Burbankite	$(Na,Ca)_3(Sr,Ba,LREE)_3(CO_3)_5$	Carbonate
Cerite*	$(LREE,Ca)_9(Mg,Ca,Fe^{3+})(SiO_4)_3(SiO_3OH)_4(OH)_3$	Nesosilicate
Dollaseite*	$CaLREE(Mg_2Al)(Si_2O_7)(SiO_4)F(OH)$	Sorosilicate
Eudialyte*	$Na_{15}Ca_6Fe_3Zr_3Si(Si_{25}O_{73})(O,OH,H_2O)_3(Cl,OH)_2$	Cyclosilicate
Euxenite*	$(REE,Ca,Th,U)(Nb,Ta,Ti)_2O_6$	Oxide
Fergusonite*	$REENbO_4$	Oxide
Fluocerite*	$REEF_3$	Halide
Gadolinite*	$REE_2Fe^{2+}Be_2O_2(SiO_4)_2$	Nesosilicate
Monazite*	$REE(PO_4)$	Phosphate
Parisite	$CaLREE_2(CO_3)_3F_2$	Parisite
Perrierite*	$REE_4(Mg, Fe,Ti)_4O_8(Si_2O_7)_2$	Sorosilicate
Pyrochlore*	$(Na,Ca)_2Nb_2O_6(OH,F)$	Oxide
Steenstrupine	$Na_{14}REE_6Mn_2Fe_2^{3+}Zr\ (PO_4)_7Si_{12}O_{36}(OH)_2\cdot 3H_2O$	Cyclosilicate
Strontianite	$Sr(CO)_3$	Carbonate
Synchysite*	$CaREE(CO_3)_2F$	Carbonate
Törnebohmite*	$REE_2Al(SiO_4)_2(OH)$	Nesosilicate
Västmanlandite	$Ce_3CaMg_2Al_2Si_5O_{19}(OH)_2F$	Sorosilicate
Xenotime*	$(Y,HREE)PO_4$	Phosphate
Zircon	$ZrSiO_4$	Nesosilicate

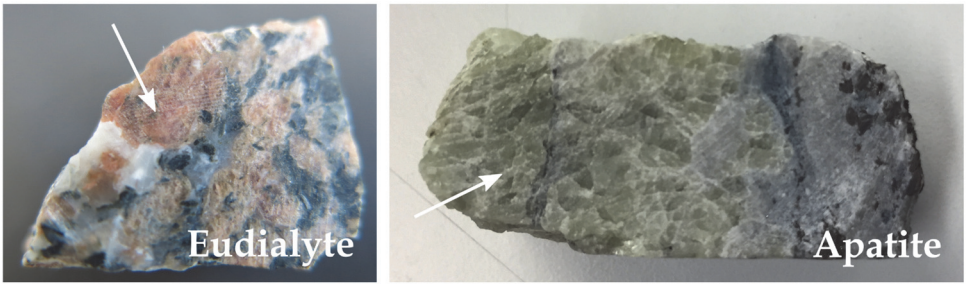

FIGURE 4. Eudialyte-rich sample from the Norra Kärr deposit, Southern Sweden (left) and REE-bearing apatite from Siilinjärvi, Eastern Finland (right).

A special system to name the REE minerals adds the predominant REE in a suffix after the mineral group name, *e.g.*, bastnäsite-(La) or bastnäsite-(Y). This type of naming was originally presented by Levinson[39] but was later also acquired by the IMA[13]. REEs have been produced from less than 20 minerals; from these, the most significant in decreasing order are bastnäsite, monazite, REE-bearing clays, xenotime, loparite, and parisite.[40] The REE-contents in these minerals vary: Bastnäsite-(Ce) 70–74, monazite-(Ce) 35–71, xenotime-(Y) 52–67, loparite-(Ce) 32–34, parisite-(Ce) 59 in wt% REO (rare earth element oxides).[41]

REE deposits can be separated into igneous, sedimentary, and secondary types. The essential REE deposits from igneous rocks occur in different kinds of carbonatite/alkaline rocks, but granite, alkaline granite, and alkaline suite rock related small REE deposits are also known. The most relevant sedimentary origin deposits are placer deposits and conglomerates. The weathering of REE-rich rocks forms secondary REE deposits that have low REE levels (total REE 0.05–0.2 wt%) but are easy to extract, *e.g.*, ion-absorption clay deposits.[37,40] One example of a carbonatite-type of REE deposit is Mountain Pass in the United States. The biggest REE deposit is Bayan Obo in China; its genesis is still uncertain, but it has a hydrothermal origin.[37]

China was the main lanthanoid producer globally in 2020, but the United States, Burma, and Australia also had rather high production levels. Production also occurred in Madagascar, Russia, Thailand, Vietnam, Brazil, and Burundi.[42] Scandium was mainly mined as a by-product in lanthanoid mines.[43] Yttrium was mainly produced in China and Burma in 2020.[44] The Bayan Obo deposit has huge REE resources estimated to be 48 Mt (million tons) 6 wt% REO.[45] The deposit at the other big mine site, Mountain Pass, has reserves of 16.7 Mt with grade 7.98 wt% REO.[46]

Several REE deposits are discovered in the Nordic countries. REE-bearing agpaitic nepheline syenites in Norra Kärr in Sweden[47] are considered a remarkable resource for yttrium, dysprosium, and terbium.[48] The highest REE potential in Finland exists in the Sokli carbonatite complex, calcsilicate rocks (skarn) in Korsnäs, and carbonatites in Kortejärvi–Laivajoki region. Other important REE occurrences include alkaline intrusions in Tana Belt (Vaulo and Mäkärä), Otanmäki and Katajakangas, hydrothermally altered systems in Kuusamo Belt, and pegmatite dykes and greisens in Central and Southern

Finland.[49] The Siilinjärvi carbonatite complex is also known to be enriched in REEs,[50–52] even though the deposit is mined only for phosphate from apatite.[38]

REEs are strategic and necessary raw materials for different fields of modern technology.[34] The biggest end use includes catalysts (~75 %) and they are also used in alloys (*e.g.*, magnets), metallurgical applications, glass, ceramics, and polishing.[42] Different household products, *e.g.*, computers, smartphones, DVD players, and TVs contain small, but essential, amounts of REEs.[40] REEs can be considered as "green metals", due to end uses in green technology fields, *e.g.*, in catalytic converters, energy-efficient fluorescent lights, and magnets in wind turbines and hybrid electric vehicles.[40,53] To give some specific examples of REE uses: Compact fluorescent lamps contain Eu, Tb, and Y[34] and Nd is needed in Nd-doped $Y_3Al_5O_{12}$ lasers (Nd:YAG). In addition, wind turbines include 150–200 kg of Nd and 20–30 kg of Dy per megawatt of generating capacity.[40]

1.2.2 Lithium

Alkali metal Lithium (Li) has an atomic number of 3 and an atomic weight of 6.941. The electronic configuration of lithium is [He]$2s^1$ and it is named after the Greek word for stone (λιθος).[54]

There is approximately 18 ppm lithium in the Earth's crust, and it tends to substitute magnesium, especially in ferromagnesian minerals.[54] Most of the lithium minerals are included in two mineral groups: complex Al-silicates and phosphates.[55] The most important Li-minerals in Europe are listed (Table 3).[56] The most essential lithium ore mineral is spodumene.[54,57,58] Examples of Finnish Li-minerals are shown in Fig. 5.

TABLE 3 The main lithium minerals in Europe[56] with their chemical formulas, mineral classes (based on Dana classification[20]) and theoretical lithium values. The table is simplified from Ref.[56].

Mineral	General chemical formula	Mineral class	Theoretical value (%)	
			Li metal	Li_2O
Amblygonite	$(Li,Na)Al(PO_4)(F,OH)$	Phosphate	4.69	10.1
Cookeite	$LiAl_4(AlSi_3O_{10})(OH)_8$	Phyllosilicate	1.34	2.9
Elbaite	$Na(Li_{1.5}Al_{1.5})Al_6Si_6O_{18}(BO_3)_3(OH)_4$	Cyclosilicate	1.89	4.07
Eucryptite	$LiAlSiO_4$	Nesosilicate	5.51	11.86
Ferrisicklerite	$Li_{1-x}(Fe_x^{3+}, Mn_{1-x}^{2+})PO_4$	Phosphate	4.40	<9.47
Holmquistite	$X(Li_2)(Mg_3Al_2)(Si_8O_{22})(OH)_2$	Inosilicate	1.85	3.98
Jadarite	$LiNaSiB_3O_7(OH)$	Nesosilicate	3.39	7.3
Lepidolite	$K(Li,Al)_3(Si,Al)_4O_{10}(OH,F)_2$	Phyllosilicate	3.58	7.7
Lithiophilite	$Li(Mn,Fe)PO_4$	Phosphate	4.43	9.53
Lithiophorite	$(Al,Li)Mn^{4+}O_2(OH)_2$	Oxide	0.57	1.23
Montebrasite	$LiAl(PO_4)(OH,F)$	Phosphate	4.69	10.1
Petalite	$LiAl(Si_4O_{10})$	Phyllosilicate	2.26	4.88
Polylithionite	$KLi_2Al(Si_4O_{10})(F,OH)_2$	Phyllosilicate	3.00	6.46
Sicklerite	$Li_{1-x}(Fe_x^{3+}, Mn_{1-x}^{2+})PO_5$	Phosphate	4.40	<9.48
Spodumene	$LiAl(Si_2O_6)$	Inosilicate	3.73	8.03
Triphylite	$Li(Fe,Mn)PO_4$	Phosphate	4.40	9.47
Zinnwaldite	$KLiFeAl(Al,Si_3)O_{10}(OH,F)_2$	Phyllosilicate	1.91	4.12

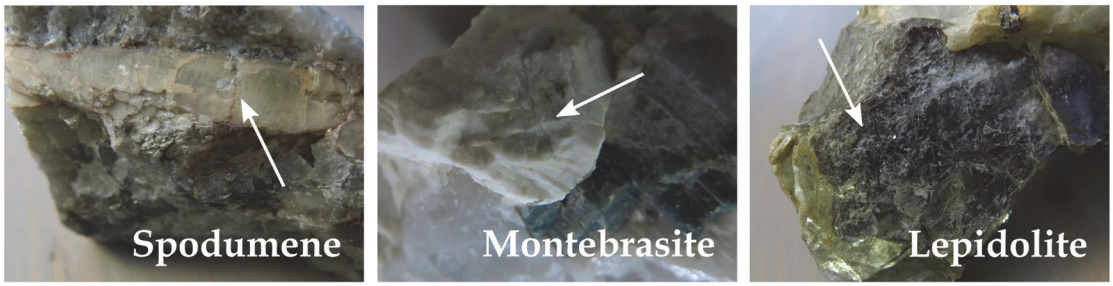

FIGURE 5. Examples of lithium minerals collected from Finland: spodumene from the Länttä deposit, Kaustinen (left), montebrasite from Viitaniemi, Eräjärvi (middle) and lepidolite from Viitaniemi, Eräjärvi (right).

The most important lithium deposits are brine lake deposits (salars) and pegmatites (hard rock occurrences). Spodumene pegmatites are coarse-grained igneous rock types whose mineralogy also includes quartz, feldspar, mica, and accessory minerals.[55] These are the mainly exploited lithium resource and coarse rock type makes it relative easily to process.[57] Other sources of lithium that can be mentioned are clays and seawater.[59–61] However, the lithium level is very modest in seawater (~170 ppb); thus, it is unlikely that lithium can be extracted cost effectively.[60]

Li-pegmatite deposits have grades of about 0.3–1.4 % Li at tonnages of 0.01–0.85 Mt Li.[58] Lithium concentrations in brines are much lower, about 200–1500 ppm Li, but the deposits are usually larger, with contents estimated as 0.1–10 Mt.[58] The main producers of lithium in 2020 listed in decreasing order are Australia, Chile, China, Argentina, Brazil, Zimbabwe, and Portugal. Only a few mineral and brine operations in these countries cover a majority of worldwide production: Australia (five minerals), Argentina & Chile (two brines), and China (two brines, one mineral). Several development projects of Li-productions are known to exist in different scales worldwide.[62] One of these is located in the Pohjanmaa region in Western Finland: the Kaustinen Li-pegmatite province.[63] Six known lithium deposits occur in the Kaustinen lithium province: Rapasaari, Länttä, Syväjärvi, Outovesi, Emmes, and Leviäkangas.[64] All of these are known to be hosted by lithium–caesium–tantalum (LCT) pegmatite.[64,65] In addition, there is a high Li-potential in LCT-pegmatites located in the Somero–Tammela region in Southern Finland. Several smaller Li-occurrences are also known across Finland.[65]

The biggest end use of lithium lies in the battery technology (~71%), particularly because the development of the electric cars has recently increased lithium production and consumption worldwide.[57,62,66] Mobile phones also contain typically Li-ion batteries.[66] Lithium is also used in several other target applications, *e.g.*, ceramics and glass, lubricating greases, polymer production, casting mould powders, and air treatment.[62]

1.3 Analytical methods in the geosciences

Analysis of REEs from minerals is quite challenging because they are chemically similar and commonly occur together in natural minerals, as presented earlier. The most suitable analysis techniques are ICP-MS, ICP-AES, XRF, and NAA[67], described next. The equipment for these techniques is rather expensive, and these methods usually operate only in laboratory environments.[68]

With inductively coupled plasma atomic emission spectrometry (ICP-AES or ICP-OES) and inductively coupled plasma mass spectrometry (ICP-MS), the dissolved sample is ionised in a hot temperature of inductively coupled plasma, which in rock analysis means long and rigorous sample preparations.[67] The ICP-AES instrument measures optical emissions from 20 to 30 elements simultaneously in ~60 seconds.[69] Detection limits depended strongly on the element with ICP-AES; for most of the REES (from Ce to Sm and from Tb to Er), detection limits as solids are ≥ 10 ppm, Yb and Lu ≤ 1.0 ppm, and 1–10 ppm for the rest (Eu, Gd, Tm, La, Y, and Sc). Lithium can be analysed at the detection limit of 1–10 ppm as a solid.[69] The ICP-MS instrument can measure elemental and isotopic ratios from almost all elements in ~60 seconds, but the instrument is more expensive than ICP-AES.[70] The ICP-MS instrument is also more sensitive compared to the ICP-AES and can obtain lower limits: most REEs have detection limits <0.01 ng ml^{-1} and for lithium 0.1–1.0 ng ml^{-1}.[70] REEs usually occur at low levels; because of this, the ICP-MS instrument is commonly preferred in REE analysis.[67] There are also other mass spectrometry-based methods in order to analyse solid mineral samples in a laboratory: LA-ICP-MS (laser ablation inductively coupled plasma mass spectrometry) and SIMS (secondary-ion mass spectrometry).[71,72] A laser pulse is used to ablate material in LA-ICP-MS, which is similar to the laser-spectroscopic method LIBS presented later.[71]

X-ray fluorescence (XRF) spectrometry is also very versatile in geoscientific studies, in which the core-level electrons (K, L, and M shells) of the minerals' elements are excited with primary X-ray radiation generated in an X-ray tube. Secondary X-ray emission (fluorescence) occurs when these return to the ground state, which reveals the chemical composition.[68] XRF is a fast technique that can be used to measure solid samples; it needs only minor sample preparation, and it is capable of performing measurements outside the laboratory (portable X-ray fluorescence, pXRF[73]). XRF is highly stable, and REEs can be analysed at detection limits of even 1–5 ppm in laboratory conditions except for yttrium, which can be detected as low as 0.1–1.0 pm. However, the technique lacks the ability to analyse light elements such as lithium.[68]

Neutron activation analysis (NAA) excites the nuclei of stable isotopes to radioactive isotopes with neutron flux from a solid sample surface. Almost all elements can be measured from ppb or ppm levels up to some percentages.[74] This technique is especially suitable in trace element analysis, and REEs can be analysed at detection levels of >1 ppm for yttrium, 1 ppb – 1 ppm for some (La, Ce, Pr, Nd, Gd, Er, and Tm), and <1 ppb for the rest (Sm, Eu, Tb, Dy, Ho, Yb, Lu,

and Sc). Lithium detection is possible with a limit of >1 ppm. However, major elemental lines can overlap the REE lines.[67]

Structural information can be achieved with molecular vibrational techniques, Raman spectroscopy and FTIR (Fourier transform infrared absorption), non-destructive techniques that are based on Raman scattering and IR absorption, respectively.[75] A complete description of mineral crystal (or powder) can be obtained with X-ray crystallography and X-ray diffraction (XRD).[68]

Fig. 6 presents several micro-scale techniques for solid samples common in the geosciences. Structural information is detected with techniques marked in pink; elemental composition is observed with the methods marked in orange; and the ones that can analyse an elemental and isotopic composition are marked in blue. Raman and LIBS are both laser-based techniques and are feasible for *in situ* and on-line purposes. SIMS (secondary-ion mass spectrometry) and the different applications of scanning electron microscopes (SEM) or scanning transmission electron microscope (STEM) are laboratory techniques. Therefore, LIBS, Raman and complementary laser-induced luminescence spectroscopy were used in this research, and the following chapter presents their basic principles.

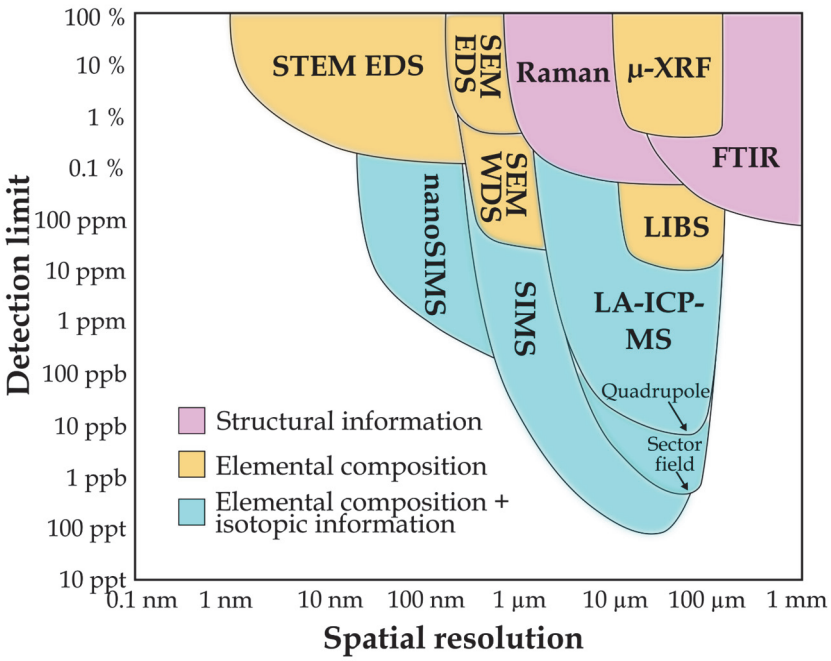

FIGURE 6. Several microbeam techniques commonly used in the geosciences are presented with a detection limit versus spatial resolution. Figure is modified from Ref.[75], which has partially adapted it from Ref.[76].

1.4 Laser-spectroscopy

Light is electromagnetic radiation, and it can be absorbed, transmitted, or scattered when it interacts with matter – *e.g.*, molecules, atoms, or ions. The

influence of these effects can be measured with spectroscopic methods.[77] Light is specified to be formed by a laser in laser-spectroscopy. The three presented techniques provide various information about the investigated minerals: The elemental composition can be achieved with LIBS; Raman spectroscopy reveals the mineral structure; and the occurrence of the luminescence activators can be discovered with laser-induced luminescence spectroscopy. Thus, these methods offer a fast way to achieve holistic information about a mineral sample. All these techniques are based on a setup of three main components: a light source (laser), a spectrometer, and a detector.

Laser ("light amplification by the stimulated emission of radiation") light has specific properties: monochromaticity, directionality, coherency, and brightness; therefore, it is advantageous in spectroscopic research.[77] Monochromatic laser light with a narrow line width enables the excitation of certain energy states with excellent precision. Coherency means that the photons are in the same phase. The Raman process is very weak, but the high-powered laser beam produces an intensive signal that improves the sensitivity of the detection. A collimated beam can travel long distances; thus, it enables remote measurements.[77–79] Active material inside the cavity specifies laser types: gas, solid-state, or liquid. Lasers can also be categorized relative to whether the laser light wavelength is in infrared (IR), visible, ultraviolet (UV), or X-ray spectral range. For example, Nd:YAG is a common solid-state laser in which neodymium-doped yttrium aluminium garnet crystal is the active material and forms a laser light at λ=1064 nm. The beam is partially converted in non-linear material in harmonic versions of Nd:YAG: second harmonic with λ=532 nm, third harmonic with λ=355 nm, and fourth harmonic with λ=266 nm. An example of a gas laser is the KrF excimer laser, in which an excited complex of noble gas Kr and halogen F forms laser light at λ=248 nm. A laser can be pulsed with a pulse duration of nanoseconds to femtoseconds in addition to constant lasing (continuous wave, CW, laser).[79,80]

The measured light can be collected with an optical fibre or directed straight to spectrometer through a narrow entrance slit. Light is dispersed inside a spectrometer to different wavelengths λ with diffraction angles θ with a prism or grating. This is presently done with a grating, in which a reflective surface is covered with grooves. The angular dispersion ($\Delta\lambda/\Delta\theta$) is connected to spectral resolution and is mostly based on groove density.[81] The most-used spectrometer system is probably the Czerny-Turner: A collimating mirror inside of it guides light to the grating, which separates the wavelengths. A refocusing mirror eventually directs dispersed light through the exit slit to the detector.[81] This is a common spectrometer type used in LIBS research.[82] The orders of the spectral lines can overlap with grating: For this reason, light with λ=266 nm can be observed with 2nd order in 532 nm and so on.[81,83] Echelle is another spectrometer type that contains a prism and a grating. The prism first disperses collimated light vertically to the grating, which disperses light horizontally; thus it disperses the light to a 2d area where it can be detected.[84,85]

A detector is a device that transforms light into digital form. Detectors can be divided into single channel and multichannel detectors. A multichannel detector, *e.g.*, charge-coupled device (CCD camera) or photodiode array (PDA), allows the simultaneous measurement of several wavelengths. An image intensifier can be installed in a CCD (ICCDs) to increase sensitivity.[81,86] Another specific type of detector is the single-photon avalanche diode (SPAD) with CMOS (complementary-metal-oxide semiconductor) technology, which is feasible for time-gated Raman detection.[87,88] The detector's suitability depends on required measurement type, spectral range, accuracy, signal-to-noise ratio, response time, *etc.*[81,86]

Other optical components are usually involved in a laser-spectroscopic setup: mirrors, apertures, fibres, filters, lenses, *etc.* The light can be directed with mirrors, apertures, and fibres. Different kinds of filters can be used to block the unwanted spectral area or laser light from the spectrometer. The laser beam can be, *e.g.*, focused or collimated with lenses. Fig. 7 presents an example of a laser-spectroscopic setup that can be used for LIBS measurement as schematics (left) and as a picture (right).

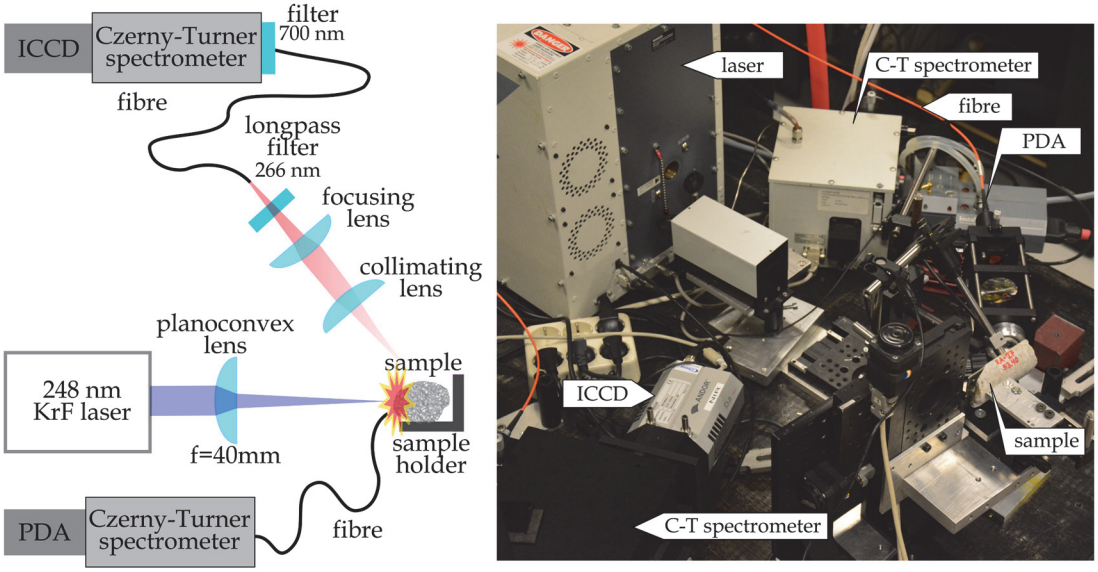

FIGURE 7. LIBS setup in tandem measurement from the same laser pulse (λ=248 nm) with two Czerny-Turner spectrometers and cameras (PDA: InGaAs array and ICCD camera) presented as schematics (left) and as a picture (right).

The focus in this research is on time-resolving forms of LIBS, Raman, and laser-induced luminescence techniques. In what follows, term delay means the time when the measurement starts after the laser beam hits the sample; gate refers to the measurement time (Fig. 8). A delay generator can be used to control the measurement time parameters in time-resolved measurements.

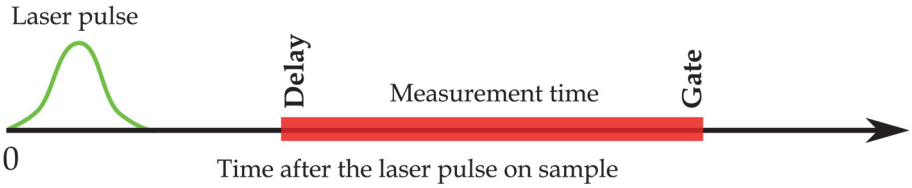

FIGURE 8. Schematics for definition of time-resolved laser-spectroscopic measurement parameters.

A spectrum can be formed from a laser-spectroscopic measurement, which presents the intensity of light versus wavenumber ($\tilde{\nu}$) or wavelength (λ). Raman spectra are usually presented with wavenumbers (cm^{-1}), and LIBS and laser-induced luminescence spectra are presented with wavelengths (nm). Intensity level is based on the amount of light: The place of the band, line, or peak on the x-axis depends on the discrete energy of emission or scattering.[77,78]

1.4.1 Laser-induced breakdown spectroscopy

Laser-induced breakdown spectroscopy (LIBS) is an analysis method that can be used to determine elemental compositions of solid, liquid, or gaseous substances. LIBS plasma is formed when the material is ablated with a focused and pulsed laser beam, and the power density on the surface is GW cm^{-2} level. LIBS measurement is based on collecting the light of the plasma emission, which depends on the chemical composition of the sampled spot (Fig. 9, a). LIBS is a semi-destructive analysis method, and small craters are formed in the ablation on a solid sample surface (Fig. 9, b).[82,89]

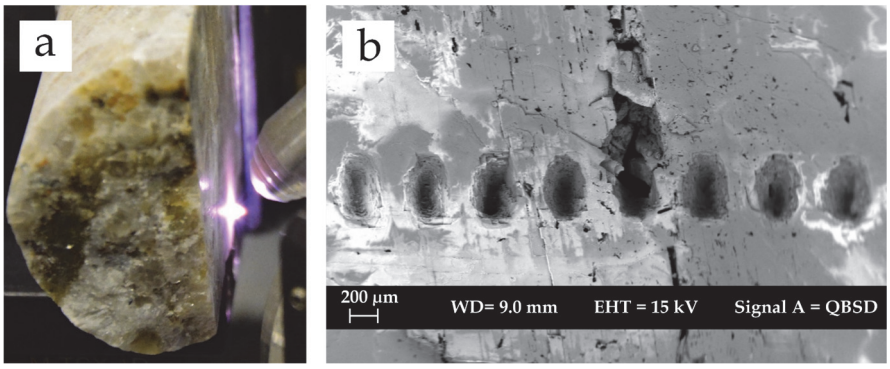

FIGURE 9. LIBS plasma on a lithium pegmatite sample (a) and LIBS craters on calcite sample surface (b) measured with a scanning electron microscope, SEM (Zeiss EVO-50XVP).

Plasma emission occurs immediately after (< 1 ns) the laser pulse, and LIBS spectrum changes as the function of time, which means that choosing the right measurement time parameters (delay & gate) influences the features of the obtained spectrum. The lifetime of LIBS plasma depends on the surrounding atmosphere, laser properties, and the investigated material. The spectrum is dominated at first by a wide, strong continuum formed from the free–free

transitions of electrons. Elemental lines can be seen more clearly after the plasma temperature and continuum drops.[82,89] The molecular emissions can also be detected on the LIBS spectrum with some samples: When the temperature decreases further, the molecules can be formed due to the atom combinations in the plasma. This means, that detection of molecular emissions is possible with rather long delay times.[89]

Different elements from various minerals have been measured with LIBS as low as tens of ppm.[90] The strength of LIBS is that elements of low atomic number can also be detected. The measurement itself is also very fast: LIBS needs only minor or no sample preparation, and the analysis can be performed directly from a solid mineral or rock sample surfaces.[73,91–95] Only a minor amount of sample is needed, which means that it also is very convenient for analysing small mineral grains or fluid inclusions.[93] Different aspects and examples of LIBS in geochemical research are presented widely in reviews[73,91–95], but it is notable that LIBS has been applied to geochemical analysis in real time and *in situ*.[73,93] The best-known examples of LIBS working in such mineral research must be the ChemCam analyser in the Mars Science Laboratory rover Curiosity[96] and in the Mars 2020 rover Perseverance[97].

LIBS can be used for either qualitative or quantitative geochemical analysis.[73,93] LIBS has high precision and accuracy in quantitative analysis when calibration is performed with samples of a very similar matrix, *e.g.*, Refs.[98,99]. However, finding proper reference standards can be challenging with heterogeneous rock samples.[73] Another way is to use calibration-free LIBS (CF-LIBS), *e.g.*, Refs.[100,101]. However, the CF-LIBS method needs further development before it can be a routine analysis method for heterogeneous rock samples, especially in the field.[73]

The self-absorption phenomenon can also make quantitative LIBS measurement challenging, especially when analysing high concentrations.[102,103] Self-absorption is especially strong in resonance lines, *i.e.*, emissions to ground state or close to ground state[89], that, *e.g.*, Li line 670.8 nm is known to be.[104] For example, Fig. 10 presents LIBS spectra of the Li-minerals spodumene, montebrasite, and lepidolite. Lithium has three intense lines in the measured spectral area: 610.4 nm, 670.8 nm, and 812.6 nm. It can be seen when the Li lines are compared with each other that in lepidolite line 670.8 nm is higher than the line 610.4 nm. This relationship is opposite in spodumene and the line intensities are nearly the same in montebrasite. The intensity of the line 670.8 nm can be seen to decrease in the middle on all spectra when the Li-mineral spectra are enlarged for closer observation of two lithium lines (Fig. 11). The explanation is that there is a high temperature and a huge density of excited atoms inside the LIBS plasma. However, the temperature at the edges of the plasma plume drops, and plasma contains more atoms occupying the ground state. The photons that correlate to resonance transitions can be absorbed by the atoms on the edges of plasma, and a dip is seen in the emission line.[89]

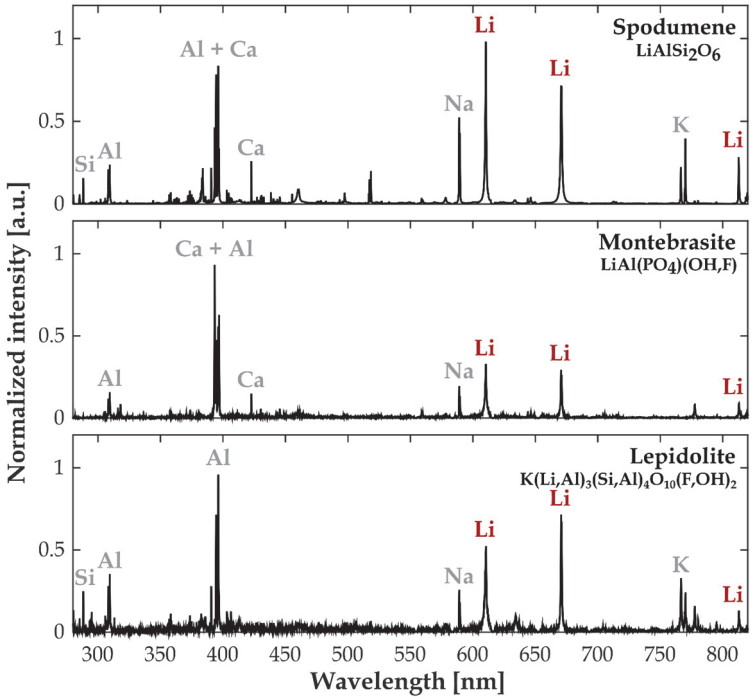

FIGURE 10. LIBS spectra (λ_{ex} 248 nm) of the Li-minerals: spodumene, montebrasite, and lepidolite. Delay and gate are 1 µs and all spectra are normalised to maximum. The most intensive lines are recognised to spectra.

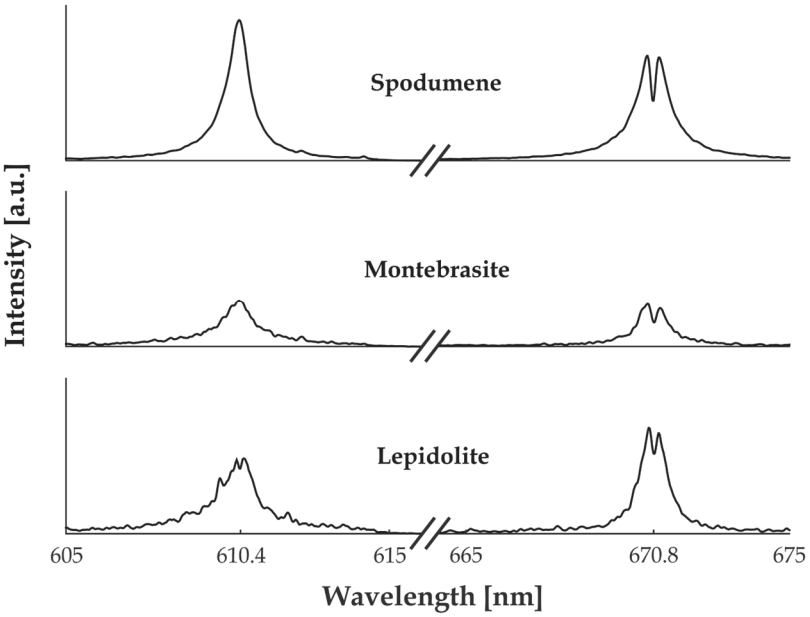

FIGURE 11. Enlarged spectra of Li-minerals' lithium lines 610.4 nm and 670.8 nm. Self-absorption is detected in 670.8 nm resonance Li line.

LIBS mapping, in which a map is measured as x number of spots in y number of rows, is a feasible tool for studying the spatial elemental and mineralogical differences of rocks. LIBS mapping is demonstrated here with a sample

containing the Li-mineral montebrasite ($LiAl(PO_4)(OH,F)$). The sample macroscopically comprises light-coloured phosphate mineral and quartz areas. The elemental compositions of these minerals significantly differ, so the intensity of one element's emission line(s) can be used to characterise the mineral location in the mapped area. For example, the integral of 214.9 nm P-line distinguishes phosphate areas from silicate (Fig. 12, a). However, it cannot solely be used to represent Li-phosphate montebrasite, because it is not exactly the same in comparison to a map constructed from the integral of 812.6 nm Li-line (Fig 12, b). Thus, elemental maps can be misleading for mineral recognition; instead, using of the whole spectral range is preferable.

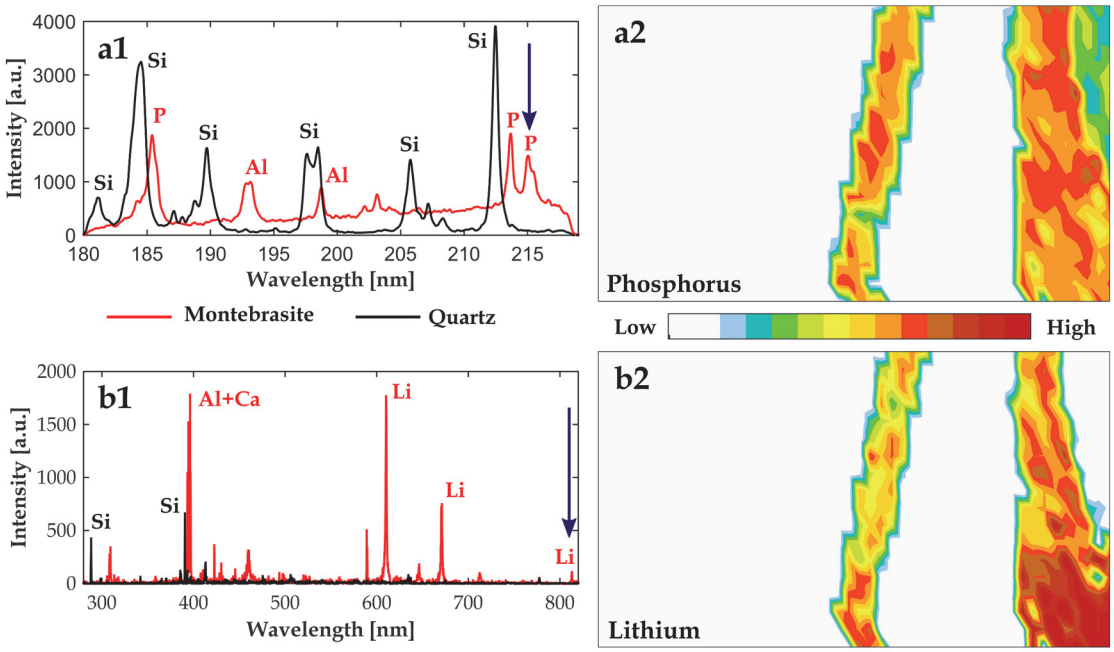

FIGURE 12. Examples of LIBS mapping in Li-bearing rock sample. Representative spectra for both recognized minerals, montebrasite (red) and quartz (black), are presented in narrow UV spectral (a1) and wide spectral (b1) range measurements. The elemental distribution maps for phosphorus (a2) and lithium (b2) emission lines were constructed from the emission lines marked with arrows to the spectra.

1.4.2 Raman spectroscopy

Most of the scattered light does not change frequency; it is called elastic Rayleigh scattering. However, a small amount changes the frequency (and wavelength); that phenomenon is known as inelastic Raman scattering. Frequency change is based on energy transfer coupled to the vibrational states; energy is transferred either from a photon to a molecule (Stokes) or from a molecule to a photon (anti-Stokes) (Fig. 13). Molecules at room temperature are usually accommodating the lowest vibrational level of the electronic ground state S_0; thus, Stokes scattering is much more common than anti-Stokes scattering.[77,78,105]

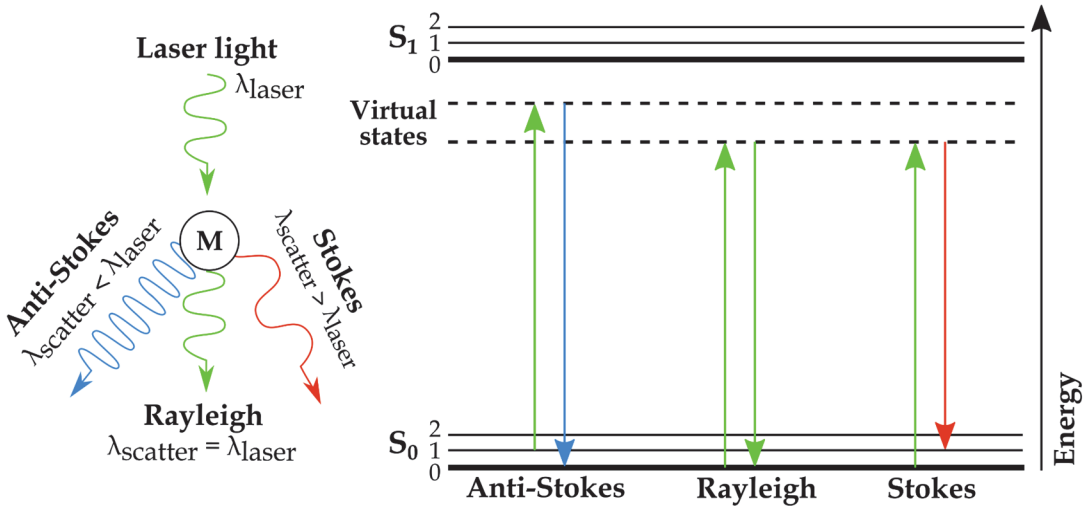

FIGURE 13. Raman scattering (anti-Stokes and Stokes) has changes in the wavelength of light (left). Scattering processes are presented in a simple energy level system (right), the figure modified from Ref.[105]. M stands for a matter in the figure.

Raman spectroscopy is a non-destructive and effective method for recognizing minerals and mineral structures.[106,107] A mineral is illuminated with laser light in Raman spectroscopy, which interacts with the sample molecules/crystal; the process depends on the polarisability of the molecule. The Raman spectrum represents the frequencies of molecular vibrations. These are called normal vibrations or normal modes and can be named in several ways, *e.g.*, related to group theory or Q notation.[107]

For example, modes of CO_3 are recognized in the Raman spectra of dolomite ($CaMg(CO_3)_2$) (Fig. 14, black) and calcite ($CaCO_3$) (Fig. 14, violet): L libration (E_g), ν_4 in-plane bend, ν_1 symmetric stretch (A_{1g}), and ν_3 antisymmetric stretch (E_g).[108-110] The last peak is expected to be a combination of modes ν_1 and ν_4 ($A_{1g}+E_g$).[110] The x-axis is given as Raman shift (cm^{-1}), which is the energy difference between the incident laser light (here λ_{ex} 266 nm) and the scattered light. These carbonates can be distinguished from each other because Raman shifts in dolomite are at higher wavenumbers compared with calcite. A smaller ion (here Mg) generally lowers interatomic distances and increases the vibrational frequencies of CO_3 vibrations in carbonates.[111] Minerals can also be recognised by utilising the extensive mineral Raman spectra library RRUFF.[112]

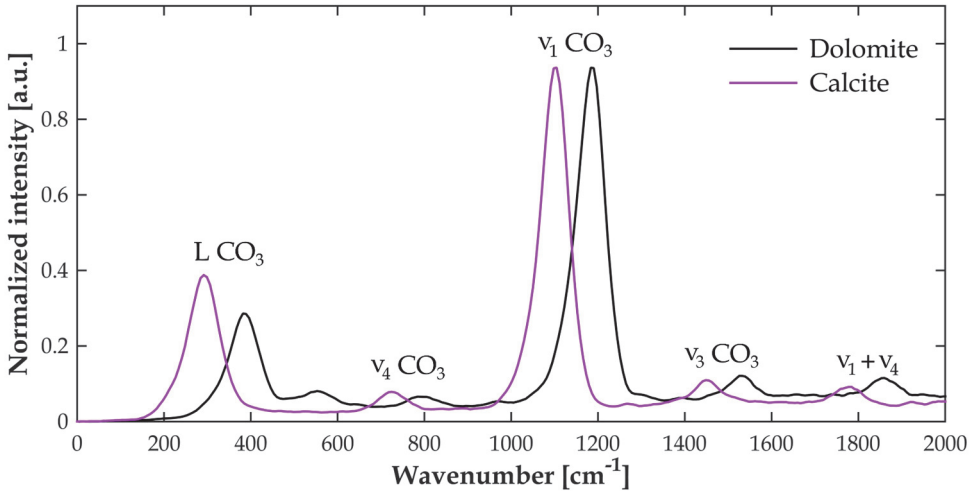

FIGURE 14. Raman spectra (λ_{ex} 266 nm) of dolomite $CaMg(CO_3)_2$ (black) and calcite $CaCO_3$ (violet) minerals presenting vibrations of CO_3.

Raman spectroscopy is a very informative technique for analysing minerals, especially due to its quick measurement time and lack of heavy and expensive sample preparation.[113] A very important feature is also the possibility of utilising Raman spectroscopy with lateral resolution in micro-scale.[107] Good examples of Raman spectroscopy in mineralogical studies are its applications for fluid inclusion[114,115] and gemological[116] studies. A possibility of working from a distance is presented in Ref.[117]; this ability is also utilised within the Raman spectrometer attached to the Mars 2020 rover Perseverance.[97] Other versatile uses of Raman spectroscopy in the geosciences are presented in Ref.[107] and various references therein.

The influence of luminescence is the most common problem in mineralogical Raman spectroscopic measurements. Intense luminescence can overlap Raman scattering partially or totally if the sample material absorbs the laser wavelength.[118] The Raman process is much weaker compared with luminescence, mostly because Raman scattering is a two-photon process in which one photon is absorbed and the second one is emitted at the same time, whereas luminescence is a one-photon process.[119,120] There are several ways to reject the luminescence in Raman spectroscopic measurements, *e.g.*, the change of the laser wavelength, to use time-gated Raman spectroscopy, or use bleaching *i.e.*, irradiate the sample surface for some time to decrease the luminescence.[118]

An example of the changing the wavelength can be seen in two Raman measurements of luminescent fluorapatite (Fig. 15). An intense luminescence band of Nd^{3+} is seen from the spectrum measured with wavelength 785 nm (Fig. 15, left). It is notable that this wavelength is typically used to reject luminescence, but it is not the best option in REE-bearing mineral samples. For comparison, if UV excitation is selected, luminescence activators are not excited and Raman peaks characteristic for fluorapatite can be clearly detected (Fig. 15, right). However, spectral resolution is much weaker with UV excitation: Note that the measured area is covering only the 15 nm spectral range. Minerals with similar

chemical structures, *e.g.*, silicates, would need interpretations based on the spectral fine structure. Therefore, in the case of luminescent minerals, time-gated Raman operating at 532 nm is the best analysis option.

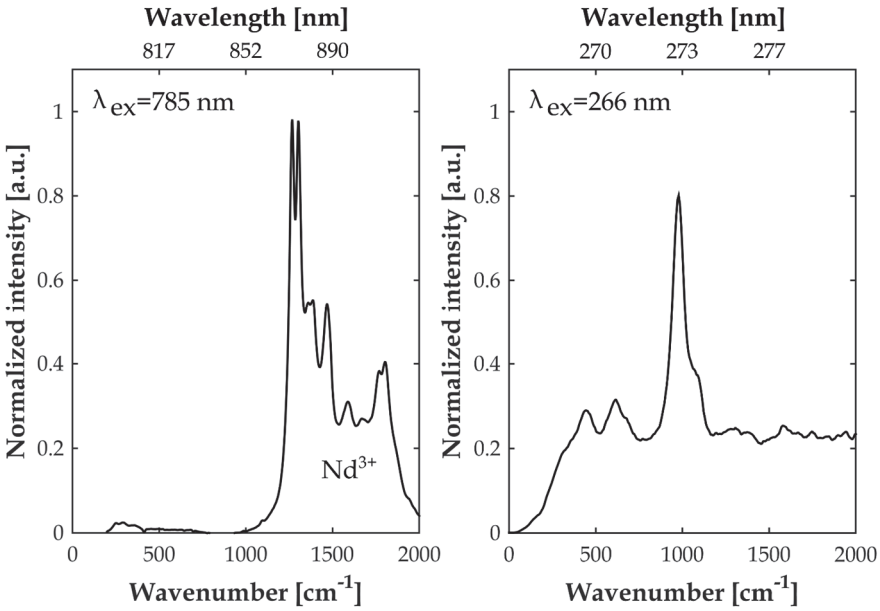

FIGURE 15. Raman spectra of fluorapatite measured with excitations 785 nm (left) and 266 nm (right). The left spectrum is dominated by a strong and intense Nd^{3+} luminescence band, while the spectrum comprises actual Raman bands on the right. Note that x-axes are presented in wavenumbers (lower scale) and wavelengths (nm) (upper scale).

1.4.3 Laser-induced luminescence spectroscopy

Luminescence is spontaneous radiative emission. There are several ways to generate luminescence emission in minerals, *e.g.*, with an electron beam (cathodoluminescence), ions (ionoluminescence), IR/UV radiation (photoluminescence), heat (thermoluminescence), or X-rays (X-ray excited luminescence).[121–123] This research uses a special type of photoluminescence, laser-induced luminescence spectroscopy. This method is often also called laser-induced fluorescence (LIF), especially in material science.[124]

Photoluminescence is observed when exciting radiation has first been absorbed by a luminescence activator. An excited state can be, *e.g.*, singlet (S_1) or triplet (T_1) state, while the ground state is typically singlet state (S_0). Luminescence emission can be divided into fluorescence ($S_1 \rightarrow S_0$) or phosphorescence ($T_1 \rightarrow S_0$); these processes are commonly presented in a Jablonski diagram (Fig. 16). Electrons of the excited singlet state are spin paired ($\uparrow\downarrow$), while orbital electrons have spins in the same direction ($\uparrow\uparrow$) in the excited triplet state and ground state. Fluorescence lifetime (τ) is commonly 10 ns, whereas phosphorescence lifetime is usually a millisecond or second scale.

Electronic transitions are very quick (~10^{-15} s), so the nuclei are unable to move considerably in this time (Franck-Condon principle).[125]

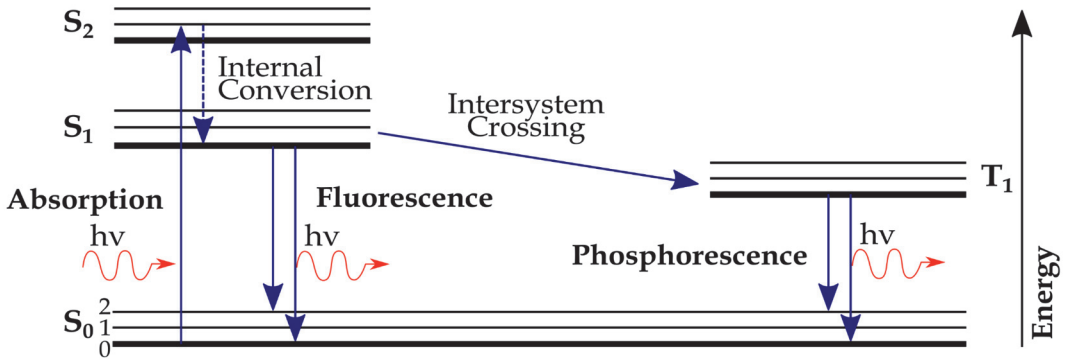

FIGURE 16. An example of a Jablonski diagram presenting the processes of fluorescence and phosphorescence. The figure is modified from Ref.[125]

In minerals, the excited electronic states and transitions are more complex than presented in Fig. 16. Therefore luminescence is generally divided into fast spin-allowed fluorescence and slow spin-forbidden phosphorescence processes.[121,124] Third luminescence type, afterglow, could also be separated, which is based on the emissions of trapped electrons.[121,124] In this thesis, general term luminescence is used in following.

Luminescence of minerals is typically based on the excitation of luminescence activators (*i.e.*, centres) in a mineral lattice. One of the most common activators in minerals is Mn^{2+}, which can replace Ca^{2+}, especially in phosphates, carbonates, and silicates. Table 4 and Fig. 17 provide examples of the luminescence activators in minerals.[121,122] There are several extensive publications that can be used to recognize mineral luminescence activators, *e.g.*, in Refs.[121,122,126,127].

TABLE 4 Luminescence activators in minerals detected in steady-state luminescence measurements. Table is simplified from Ref.[121].

Emission type	Transition / emission type
Lanthanoid ions:	4*f*–4*f* transitions
Nd^{3+}, Sm^{3+}, Sm^{2+}, Eu^{3+}, Gd^{3+}, Tb^{3+}, Dy^{3+}, and Yb^{3+}	Line
Lanthanoid ions:	5*d*–4*f* transitions
Ce^{3+}	Band
Eu^{2+}	Band
Yb^{3+} and Sm^{2+}	Band
Transition metal ions:	*d*–*d* transitions
Cr^{3+}	Line
	Band
Mn^{2+}, Fe^{3+}	Band
d^0 Complex ions:	Charge–transfer transitions
$(VO_4)^{3-}$, $(WO4)^{2-}$, $(MoO_4)^{2-}$, $(TiO_4)^{4-}$	Band
$(UO_2)^{2+}$	Band

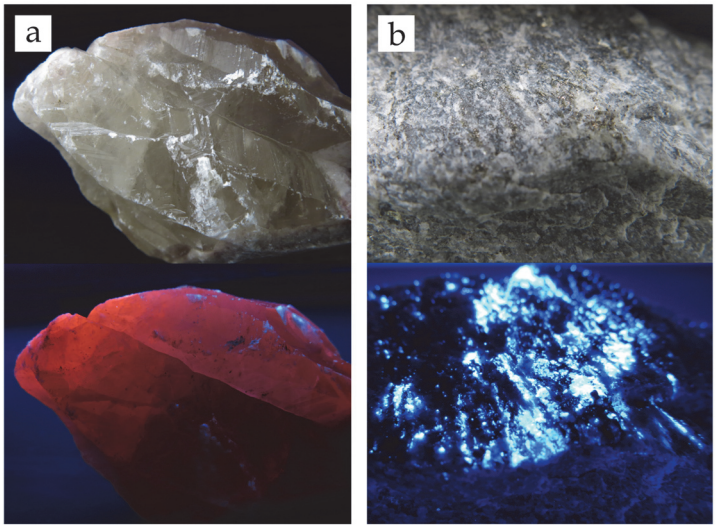

FIGURE 17. Luminescence of Mn^{2+} in calcite mineral sample (a) and $(WO_4)^{2-}$ in scheelite in a feldspar porphyry sample (b) detected in 254 nm UV light (lower). Corresponding areas are also presented in natural light (upper).

Not all minerals are luminescent because return to the ground state can be nonradiative.[121,122] Mineral luminescence can also include sensitising and quenching processes. A sensitiser is an ion that can absorb radiation and then transfer the energy to the activator.[128] Absorbed energy can also be transferred to a quencher that has a nonradiative transition to the ground state.[121,122] Rare earth elements are not just common activators but can also act as sensitisers. The most important quenchers in minerals are known as Fe^{2+}, Co^{2+}, and Ni^{2+}.[121,122]

Luminescence studies in the geosciences are functional, especially in discovering trace element information that includes site occupation and valence states in minerals. Ref.[124] presents multiple examples and references. Luminescence spectroscopy has also been found suitable for the exploration and mineral processing fields because it is capable of sorting and remote sensing.[124]

This research used time-resolved laser-induced luminescence, a highly sensitive technique, to detect REEs in minerals: for example, the luminescence has been successfully measured from mineral samples with ppm levels of REEs.[129] The lanthanoid ion 4*f*–4*f* transitions occur as sharp line emissions because 4*f* orbitals do not affect binding. Excitation does not change the internuclear spacings in a molecule very much, which causes sharp lines with modest Stokes shifts. Conversely, as a result of 5*d*–4*f* transitions such as Ce^{3+}, Eu^{2+}, Yb^{3+}, and Sm^{2+}, the larger Stokes shifts cause broad luminescence bands. (Fig. 18).[130] Lanthanoid 4*f*–4*f* transitions occur in almost at the same spectral range in spite of the host mineral, based on the electron structure of an incompletely filled 4*f* shell that is shielded by the surrounding orbitals (Table 1). However, the spectral range of 5*d*–4*f* transitions emission band shifts due to the host mineral's properties.[128] This is comparable to the occurrence of a Cr^{3+} emission, which is affected by the adjacent crystal field[121,128], or to an Mn^{2+} emission, which is greatly influenced by the luminescence host.[128]

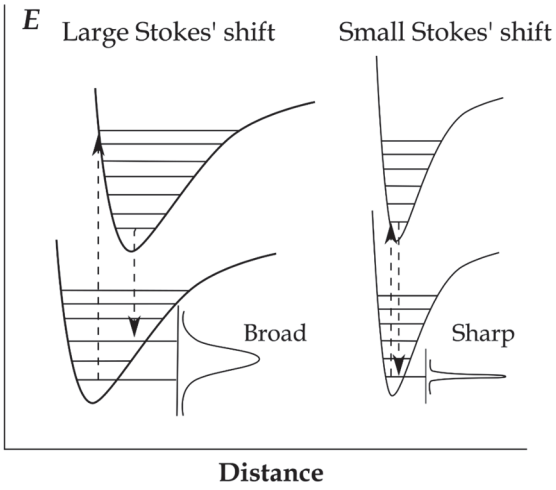

FIGURE 18. The shape of the luminescence emission line/band in the spectrum varies depending on the location of the potential energy curves at the internuclear distance axis. The transitions are presented vertically due to the Franck–Condon principle. Stokes shift relationships are presented as emission types: large (like lanthanoid 5*d*–4*f* transitions) and small (like lanthanoid 5*d*–4*f* transitions). Figure is simplified from Ref.[130].

Different luminescence activators have different lifetimes. For example, lanthanoid 4*f*–4*f* line emissions have much longer lifetimes than Ce^{3+} and Eu^{2+} 5*d*–4*f* band emissions. These can be separated with time-resolved laser-induced luminescence spectroscopy by choosing the relevant measurement time parameters.[121,122] Ce^{3+} with a very short lifetime can be included or excluded from the spectrum by choosing the right delay time, presented in Fig. 19, where the luminescence of Ce^{3+} in apatite can be seen at three chosen delay and gate times.

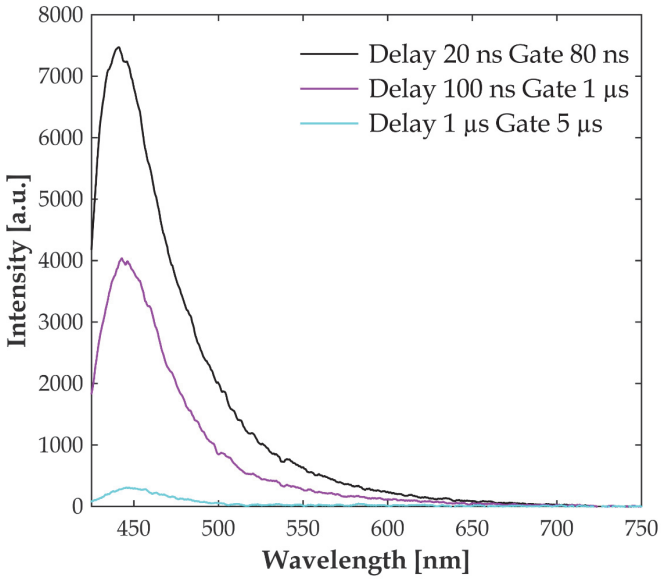

FIGURE 19. Luminescence decay of Ce^{3+} can be seen in time-resolved laser-induced luminescence spectra measured from a luminescent apatite sample (λ_{ex} 248 nm) with three chosen delay and gate times.

A luminescence emission spectrum shows luminescence intensity versus emission wavelength at a specific excitation wavelength. Meanwhile, the excitation spectrum displays the luminescence intensity versus the excitation wavelengths at the chosen emission wavelength.[121,122,128] For example, excitation (λ_{em} 486 nm; Fig. 20, black) and emission (λ_{ex} 218 nm Fig. 20, violet) spectra for Tb^{3+} luminescence in fluorapatite is presented. Natural mineral samples can contain several luminescence centres; therefore, the construction of an excitation spectrum is usually not as trivial as in Fig. 20 because the luminescence emission bands may be partially overlapping. Therefore, an emission–excitation matrix (or map), a 2d contour presentation of luminescence intensity related to emission and excitation wavelengths, enables the selection of the convenient excitation wavelength for the optimal detection of REEs.

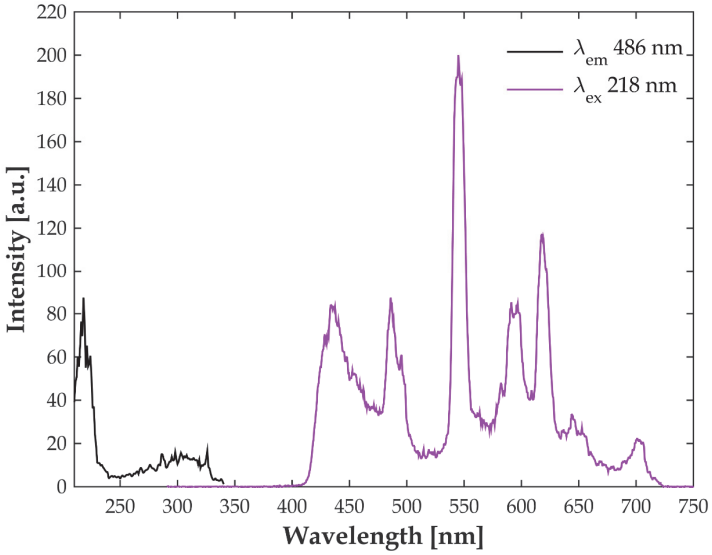

FIGURE 20. Excitation spectrum (210–340 nm) for Tb^{3+} emission 486 nm (black) and emission spectrum with excitation 218 nm (violet) in a natural fluorapatite sample are presented. Measurements are performed with delay 50 µs and gate 500 µs. Note that the emission spectrum also contains other luminescence centres as Tb^{3+}.

2 SAMPLES AND METHODS

2.1 Samples

The samples for this research were natural rare earth element (REE) and lithium-bearing rocks and minerals from the European region. REEs and lithium were selected as study material due to their criticality. The samples were sawed and some slightly polished to obtain a smooth surface for the measurements. This was especially convenient for the mapping measurements carried out in papers I, II, and III.

The rare earth element-bearing diamond drill core halves (papers I and III) comprised of nepheline syenite from the Norra Kärr Alkaline Complex. This rock type has been named also as grennaite, related to nearby town Gränna.[131] The Norra Kärr deposit is an important HREE project in South-central Sweden and is indicated to contain the resources of 58.1 Mt with 0.59 wt% REO and it is a source of the raw materials of yttrium, dysprosium, and terbium.[48] The chosen samples were collected from a so-called PGT domain, grennaite with pegmatite, in which the total REO is reported as 0.62 % and ZrO_2 2.01 %.[132] The main interest in these samples was in two complex Zr-silicate minerals, eudialyte and catapleiite, that contain REEs. Table 5 lists all the main minerals of these samples.

TABLE 5 The main minerals of the Norra Kärr deposit.[132]

Mineral	Chemical formula
Aegirine	$NaFeSi_2O_6$
Nepheline	$(Na,K)AlSiO_4$
Natrolite – Analcime	$Na_2Al_2Si_3O_{10} \cdot 2H_2O$ – $NaAlSi_2O_6 \cdot H_2O$
Microcline	$KAlSi_3O_8$
Albite	$NaAlSi_3O_8$
Anorthoclase	$(Na,K)AlSi_3O_8$
Eudialyte	$Na_{15}\ Ca_6(Fe,Mn)_3\ Zr_3Si(Si_{25}O_{73})(O,OH,H_2O)_3\ (OH,Cl)_2$
Catapleiite	$Ca/Na_2ZrSi_3O_9 \cdot 2H_2O$

In paper II lithium-bearing pegmatites from the Kaustinen lithium province in Finland were analysed. More precisely, the samples were collected from the Länttä and Rapasaari deposits. Pegmatite is a very coarse-grained rock type and the most interesting mineral within these samples was Li-mineral spodumene. This lithium province is known to be an economically important Li-source.[64] Table 6 presents all the main minerals of Li-bearing pegmatites of the Kaustinen area. Another target in paper II was to the discover how the grain size affects the LIBS analysis results. For this reason, two coarse-grained, one medium-grained, and one fine-grained samples were chosen for analysis.

TABLE 6 The main minerals of the Kaustinen Li-pegmatites.[133]

Mineral	Chemical formula
Spodumene	$LiAlSi_2O_6$
Quartz	SiO_2
Albite	$NaAlSi_3O_8$
K-feldspar	$KAlSi_3O_8$
Muscovite	$KAl_2(AlSi_3O_{10})(OH)_2$

In paper IV REE-bearing fluorapatite $Ca_5(PO_4)_3F$ and calcite $CaCO_3$ mineral samples from the Siilinjärvi ultramafic alkaline-carbonatite complex in Finland were analysed with laser-induced luminescence spectroscopy. These were selected as examples of common luminescent minerals[121,122], which are known to contain REEs in the Siilinjärvi deposit.[50] Apatite from the Siilinjärvi deposit is currently exploited only as phosphorus source.[49]

2.2 Experimental methods

All the main measurements were performed in the laser laboratory of the Nanoscience Center (Laserlab-NSC), University of Jyväskylä. The crucial equipment were the Raman, LIBS, and laser-induced luminescence setups, but this study utilised a variety of research instruments. The most important components are presented here, and the papers provide more precise details. The pulsed Nd:YAG laser with λ_{ex} 266 was exploited in paper II and the CW-laser with λ_{ex} 532 nm was used in paper III. The Nd:YAG laser with OPO at wavelength ranges of 210–340 nm and 405–535 nm was used in paper IV when the option of an excitation wavelength change in a wide spectral range was needed. LIBS measurements in papers I and III were executed with excimer KrF laser (λ_{ex} 248 nm). This laser was also the excitation source to compose laser-induced luminescence photos, which offered a way to use macroscopic recognition for luminescent minerals in papers I, II, and III. The lasers of this research operated with ns-scale pulse duration except for the time-gated Raman spectroscopy setup in the University of Oulu, which had a ps-laser.

The Czerny-Turner type spectrometer was used in all articles. The possibility to detect the second order lines was applied in the LIBS analysis of the lithium-bearing rocks (paper II), where the aluminium lines at 616.4 nm and 618.6 nm and the silicon line at 576.3 nm are 2nd order peaks for lines at 308.2, 309.3 nm, and 288.2 nm, respectively. Echelle spectrometer was utilized in the LIBS measurements of paper II.

The main detector type in this thesis was an ICCD camera, but a single-photon avalanche diode (SPAD) array was operated at the University of Oulu in paper III's time-gated Raman measurements.

3 RESULTS & DISCUSSION

Time-resolved applications of three laser-spectroscopic techniques were used to analyse REE and lithium-bearing natural mineral and rock samples. The work was performed in a laboratory environment with a focus on optimised performance when considering applications for *in situ* and on-line measurements. Analyses were performed directly from the rock or mineral surface, and samples needed only minor pre-treatment before analysis.

Papers I and II present the applications of LIBS for mapping the rock surfaces. Paper III states mineral identification with time-gated Raman spectroscopy, and paper IV describes the results of laser-induced time-resolved luminescence.

3.1 Laser-induced breakdown spectroscopy

The information on the whole LIBS spectrum (or part of it) can be used to detect differences and similarities between the spectra when the data are grouped using chemometric methods.[134] Several approaches to analysing the LIBS data of geological materials have been presented, including, *e.g.*, principal component analysis (PCA)[135–142], partial least squares discriminant analysis (PLS-DA)[135,141,143–145], K-means clustering[146,147], soft independent modelling of class analogy (SIMCA)[136,137,147], support vector machines (SVM)[144], and random forest (RF)[148] techniques. In papers I and II, the LIBS data of REE and lithium-bearing rock samples are grouped with different chemometric procedures. Fig. 21 shows simplified schematics of the LIBS analysis and the data treatment with statistical methods for evaluating the mineralogical composition.

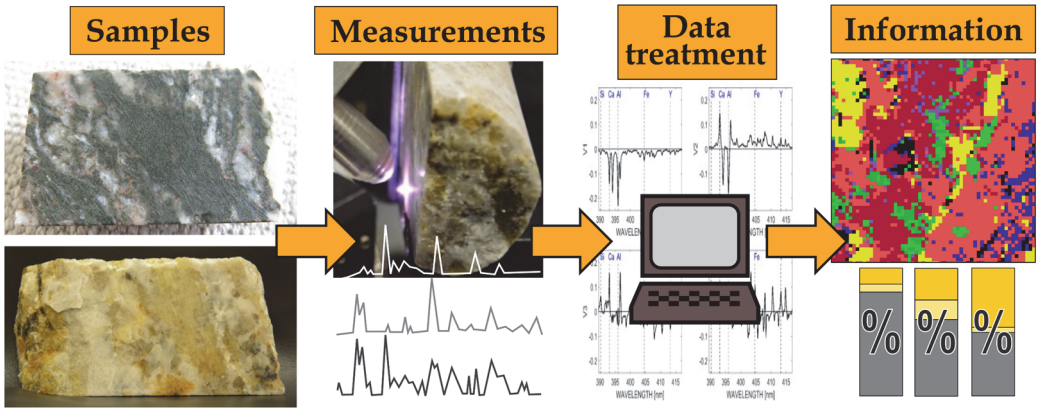

FIGURE 21. Simplified schematics of the presented statistical analyses to LIBS results.

Paper I presents the use of singular value decomposition (SVD) in detecting REE-bearing eudialyte and catapleiite minerals from the LIBS data of nepheline syenites. In Paper II Li-bearing pegmatites are analysed with LIBS and developed statistical approaches are used to recognise Li-mineral spodumene. This research utilises the methods of PCA (principal component analysis), K-means, DBSCAN, and vertex component analysis (VCA). The excellence of the presented statistical groupings is that no knowledge about the mineralogy of the measured rock sample is necessary before the data handling. The spectra of the formed groups can be recognised as minerals after the procedure. The knowledge of mineralogical information, elemental distributions, and macroscopic recognition can also be used for this task.

3.1.1 REE-bearing minerals eudialyte and catapleiite

In paper I three nepheline syenite samples from the Norra Kärr deposit in Sweden were measured with LIBS. The main interest was the REE-bearing minerals eudialyte and catapleiite. The most abundant REE is yttrium, and the ΣY_2O_3 content is ~3.2 % in eudialyte.[47]

Even though the results of the LIBS analysis of rare earth elements from geological samples have been previously reported, *e.g.*, Refs.[90,146,149,150], the REE emission lines in the LIBS spectra have usually been detected only from samples containing rather high percentage levels of REEs. The only lines of REEs found in the LIBS spectra from the Norra Kärr samples were the atomic lines of yttrium in eudialyte and slightly in catapleiite. The optimal spectral range 389–417 nm was selected for further analysis, because it also contained the strong lines of aluminium and calcium, and smaller lines of silicon, manganese, and iron.

The measured unprocessed LIBS data was treated with singular value decomposition (SVD) (Fig. 22). The matrix A is formed from the product of matrices U, S, and V when using SVD. Columns U and V are singular vectors, and the U and V are orthogonal matrices, while S is a diagonal matrix (singular values), presented in decreasing order.

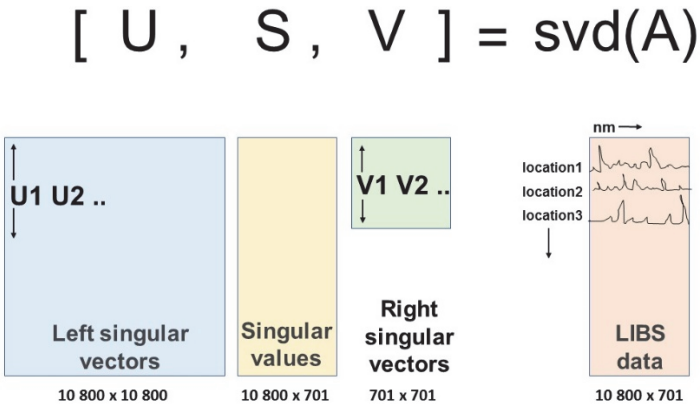

FIGURE 22. Schematics of the SVD variables. Reprinted with permission from *Spectrochim. Acta Part B At. Spectrosc.*, 2017, 134, p. 69. Copyright © 2017 Elsevier B.V.

SVD was performed with non-centred data; therefore, the first component presented an average spectrum while others are variations of it. Fig. 23 presents the SVD components V1–V4 that represented 99,5 percent of the variances. The components showed loads compared to zero, which means no contribution in that spectral area: The higher the positive/negative value, the higher is the contribution to that area. The most important chemical elements were marked with dotted lines to the components to clarify the outcome.

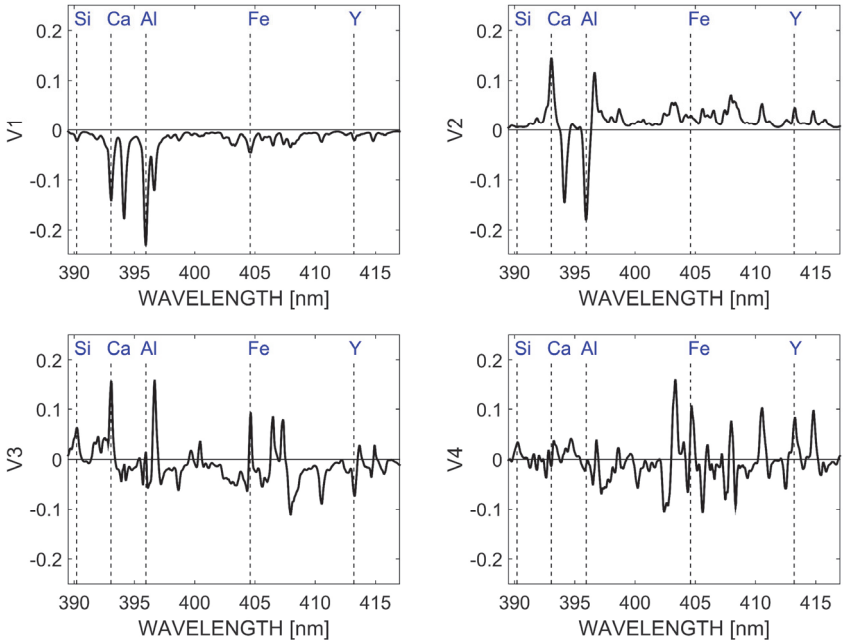

FIGURE 23. Singular vectors V1–V4 with the most representative lines marked. Reprinted with permission from *Spectrochim. Acta Part B At. Spectrosc.*, 2017, 134, p. 69. Copyright © 2017 Elsevier B.V.

The U matrices' values present the first four SVD components as maps. Values in U1 are negative compared with the values of V1, but U2, U3, and U4 contain positive and negative values (Fig. 24).

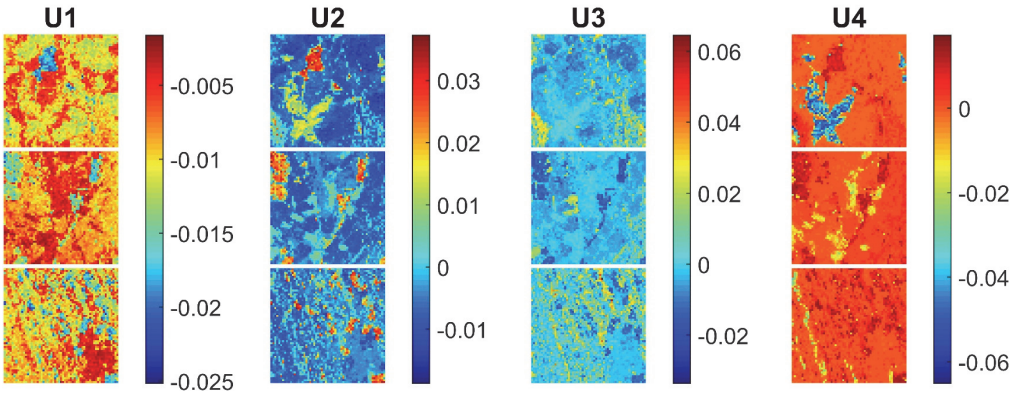

FIGURE 24. Left singular vectors U1–U4. Reprinted with permission from *Spectrochim. Acta Part B At. Spectrosc.*, 2017, 134, p. 69. Copyright © 2017 Elsevier B.V.

All the data points were classified with the signs of U2–U4 into eight ranges like +++, ++-, +-+, *etc*. The mapped areas can be presented with eight colours (Fig. 25, 1). These maps can be compared with photos of sample surfaces in natural light and in 248 nm UV laser light (Fig. 25, 2 & 3). The yttrium distribution based on the intensity of the line 412.8 nm is shown on the right (Fig. 25, 4).

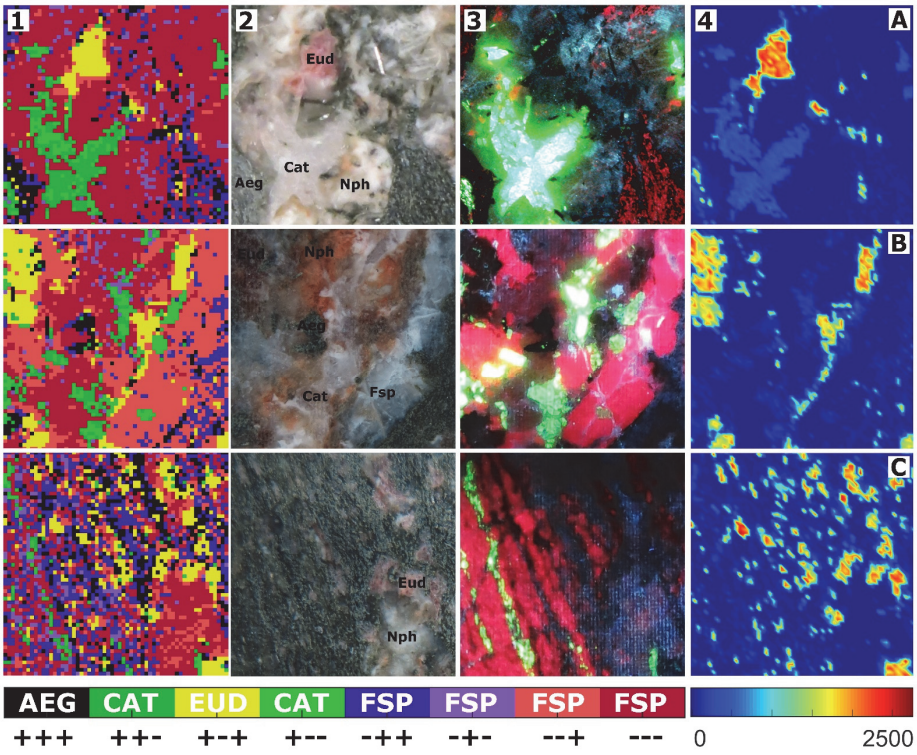

FIGURE 25. Mineral classification based on SVD (1), sampled areas in natural light with some minerals macroscopically identified (2) and in 248 nm UV laser light (3) and yttrium map, due to line 412.8 nm intensity (4). Catapleiite with $(UO_2)^{2+}$ intense green luminescence can be detected in the UV laser photo (3). Mineral abbreviations: Aeg=aegirine, Cat=catapleiite, Eud=eudialyte, and Fsp=feldspar minerals. Reprinted with permission from *Spectrochim. Acta Part B At. Spectrosc.*, 2017, 134, p. 69. Copyright © 2017 Elsevier B.V.

The blue and red ranges (-++, -+-, --+, and ---) were recognised as feldspar and feldspathoid minerals on the basis of the original LIBS spectra. The yellow areas contained elements that suggested these areas were eudialyte, which correlates to the photos and to the yttrium distribution map. The green areas can be assumed to be catapleiite due to their elemental compositions and intense green luminescence. However, Raman spectroscopy would offer a way to ensure these conclusions because the chemical composition of the minerals in the Norra Kärr deposit are much similar.

3.1.2 Li-bearing mineral spodumene

LIBS is an especially sensitive method for analysing light elements, including lithium.[73] LIBS analysis of lithium in different minerals can be found in Refs.[102,103,151,152]. Paper II presents LIBS measurements and the statistical investigation of the data from lithium-bearing spodumene pegmatites. Four representative samples with various grain sizes from two lithium deposits in the Kaustinen area were selected. The first stage of the study LIBS analysis was performed with a wide spectral range (280–820 nm) to investigate the most prominent area for effective spodumene separation.

The data handling procedure, developed by co-author Dr. Ilkka Pölönen, includes data reduction with principal component analyses (PCA); K-means, DBSCAN, and vertex component analysis (VCA) were subsequently used to discover the mineralogical differences in the spectra. The basic idea of PCA is to form new variables, principal components (PCs), from the data without losing much variance information.[153] Anomalous spectra, *i.e.*, outliers, were detected with PCA and DBSCAN and replaced with spectra formed mathematically from the neighbouring spectra. Some accessory minerals, *e.g.*, Nb-Ta oxide, were discovered when the outlier spectra were examined separately.

In VCA each spectrum in the data set is expressed as a linear combination to n most dissimilar spectra, *i.e.*, endmembers.[154] The endmembers can be assumed, in the case of minerals, to present the chemically simplest forms of the main minerals within the data set. Five spectral endmember groups were formed from LIBS data on pegmatite. The endmembers were recognised as spodumene, quartz, K-feldspar/muscovite, and albite and a group of calcium rich minerals when their emission lines were inspected.

A map based on VCA was constructed to visualize the spodumene distributions. This was compared to areas estimated to be spodumene by using a model spectrum-based lsqnonneg fitting and locations where the lithium line 812.6 nm intensities were relatively high (Fig. 26). The results obtained are comparable, and VCA also detects the spodumene regions macroscopically. Only slight differences can be seen, the most likely based on areas on the grain borders where a laser beam can hit two minerals simultaneously.

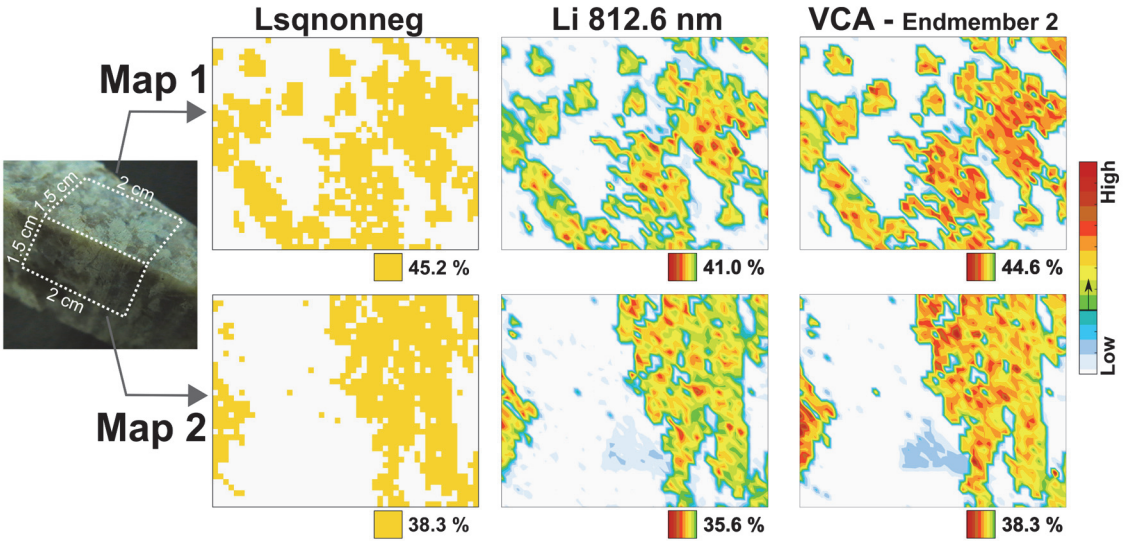

FIGURE 26. Spodumene distribution maps constructed from LIBS data measured from two perpendicular surfaces (Map 1 & Map 2) of the same coarse-grained sample with three different methods: lsqnonneg, lithium distribution, and vertex component analysis (VCA).

Two cluster analyses were performed from the prereduced data of Maps 1 and 2. K-means recognised *n* non-overlapping clusters from the data. The number of clusters must be chosen beforehand. All the data points will be divided into clusters.[155] The other used cluster analysis, DBSCAN, forms groups around the densest areas of the analysed data points. The neighbour size, *i.e.*, the radius of the neighbourhood for the data points as well as number of neighbours, *i.e.*, minimum number of points to each cluster must be selected in the construction of DBSCAN grouping.[156]

Statistical groups were recognised to minerals based on mean spectrum of each cluster, *i.e.*, centroids and verified with macroscopical examination. Centroid spectrum which was recognised as spodumene is presented as red and the other colours represented the rest of the minerals of spodumene pegmatite samples (Fig. 27). Spatial mineralogical distributions in the K-means and DBSCAN maps were rather similar and in centroid spectra only small differences were seen. The main difference in data groupings can be seen in the projections were the unclassified data (violet) of DBSCAN. These spectra locate in mineral grain borders in maps: These occur at the edges in the clusters in projections (Fig. 27, centre) and most likely represent the intermediate spectra of two minerals. Another difference was K-bearing minerals (orange group) that were only recognised in K-means clustering.

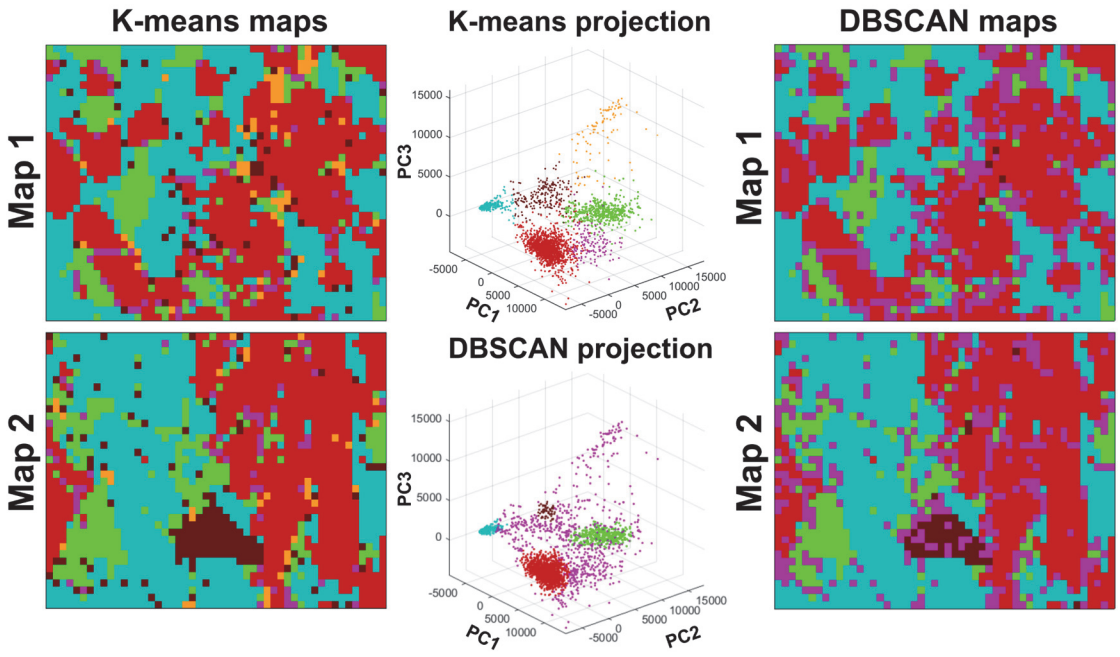

FIGURE 27. K-means maps (left) and DBSCAN maps (right) presented from the LIBS data of Maps 1 and 2. Projection for the data with both methods is presented in the centre. Colours present recognized minerals of beryl (brown), spodumene (red), albite (green), quartz (turquoise), K-feldspar/muscovite (orange), and combination of two minerals (K-means) or unclassified spectra (DBSCAN) (violet).

On the second stage of this research, a narrow spectral area (560–815 nm) with only the most significant emission lines was measured. The idea was to test the feasibility of the developed statistical approaches for *in situ* types of applications when the data processing must be smooth, *i.e.*, the data size should be decreased without losing important information.

The LIBS data measured from coarse-, medium-, and fine-grained samples (Maps 3–5) were treated similarly as in the first stage; the detected outliers were replaced, and the data dimensions were decreased with PCA. Three VCA endmembers were detected and identified as spodumene, albite, and quartz. The VCA for spodumene was compared with lsqnonneg and lithium distribution (Fig. 28); as a result, the narrow spectral area for VCA also seemed to be effective for the spodumene recognition in all samples.

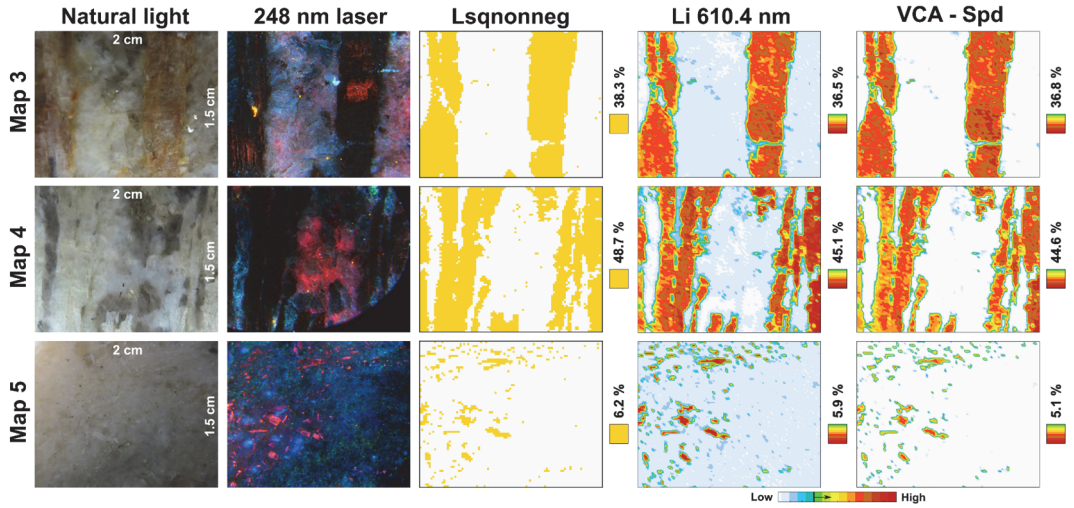

FIGURE 28. VCA spodumene occurrence compared with lsqnonneg spodumene detection and lithium distribution map in coarse-, medium-, and fine-grained samples.

The spodumene areas are presented as red and the number of cluster groups found from different data sets (Maps 3, 4, and 5) was observed to change (Fig. 29) when using K-means and DBSCAN clusterings. Both clustering methods were relatively efficient in spodumene recognition with the coarse- and medium-grained samples (Maps 3 and 4), but the recognition of spodumene was not working correctly with the fine-grained sample (Map 5), especially in the case of the K-means approach. As a result, the VCA would be the most efficient method for the recognition of spodumene locations in Li-pegmatite samples with a narrow spectral range.

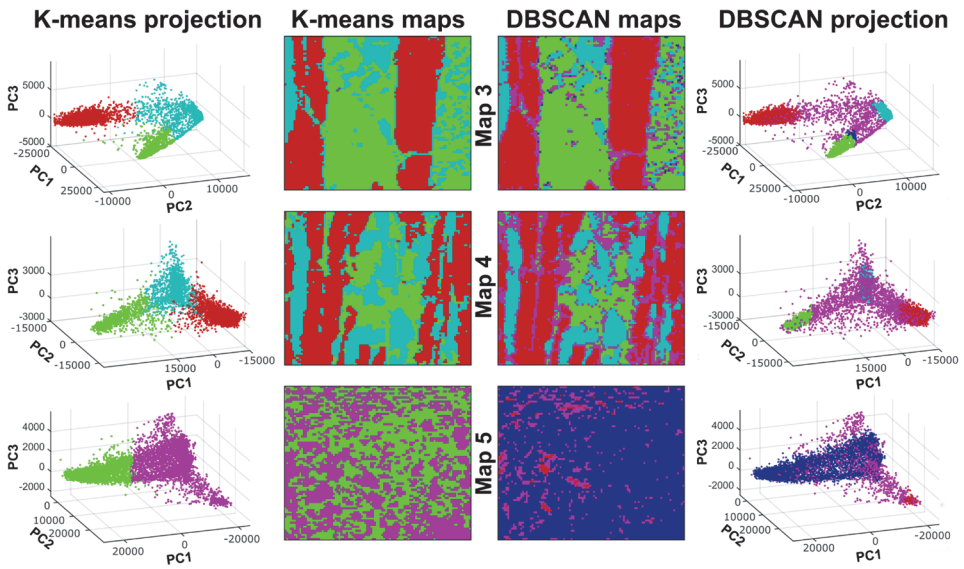

FIGURE 29. Cluster analyses results of K-means and DBSCAN for coarse-, medium-, and fine-grained samples (Maps 3–5). The colours present the recognised minerals of spodumene (red), albite (green), and quartz (turquoise). Violet presents the combination of two minerals, while navy blue in Map 5 was interpreted as the combination cluster of albite and quartz.

3.2 Time-gated Raman spectroscopy

Raman mapping of the REE-bearing nepheline syenite (PGT grennaite) sample with traditional CW-Raman spectroscopy is challenging due to its luminescent minerals. These can be detected from the laser-induced luminescence images from the sample surface (Fig. 25), where an intense green luminescence was observed in the catapleiite mineral and recognised as originating from the luminescence activator $(UO_2)^{2+}$. The areas that were also seen with intense red luminescence were most likely related to the occurrence of Mn^{2+}.

The strong luminescence background either disturbs or hinders the recognition of mineral Raman spectra. An example of luminescence in the investigated samples can be seen in CW-Raman measurements (λ_{ex} 532 nm) (Fig. 30).

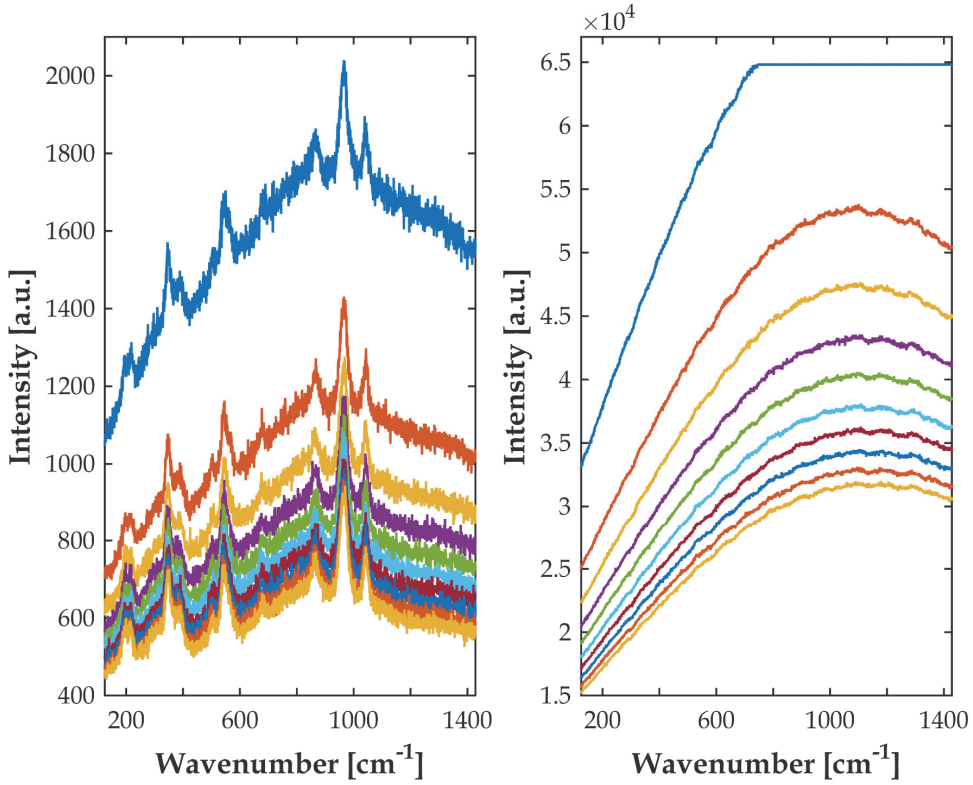

FIGURE 30. Examples of CW-Raman measurements (λ_{ex} 532 nm) performed from the REE-bearing nepheline syenite sample from the Norra Kärr REE deposit. The example on the left presents a measurement with a strong luminescence background disturbing the detection of the Raman modes, while luminescence dominates the whole spectra on the right. All the spectra were measured with 0.1 s (200 mW) per spectrum to demonstrate the influence of bleaching.

The luminescence intensity drops in some cases when the sample is illuminated a longer time with a laser, *i.e.*, bleached. Fig. 30 presents this (left) where a baseline correction should be enough to enhance the quality of the spectrum. The observed luminescence is so intense and strong with another mineral (Fig. 30,

right) that bleaching has no effect. However, when the focus is on *in situ* and on-line measurement purposes, the time-consuming bleaching and data treatment are not good options.

Time-gated Raman offered a solution in paper III to luminescence reduction in the analysis of the Norra Kärr nepheline syenite samples. Different time responses of Raman and luminescence photons are utilised with this technique by using fast pulsed ps-laser and time-gated detection with a single photon avalanche diode (SPAD) detector. A time-gated Raman spectrometer was developed and operated at the University of Oulu by the co-authors; the details of the technique are presented elsewhere.[88]

The main minerals in the Norra Kärr deposit are different silicates (Table 5). Silicates, as presented earlier, have very similar crystal structures (Fig. 3). Therefore, the obtained time-gated Raman spectra were not varying strongly from each other. The statistical methods presented earlier in articles I and II to represent mineralogical changes in mapped areas were not working efficiently because of this. Fig. 31 shows the time-gated Raman spectra of the cyclosilicates catapleiite and eudialyte. It is notable that eudialyte had about a one magnitude lower Raman intensity than the other minerals.

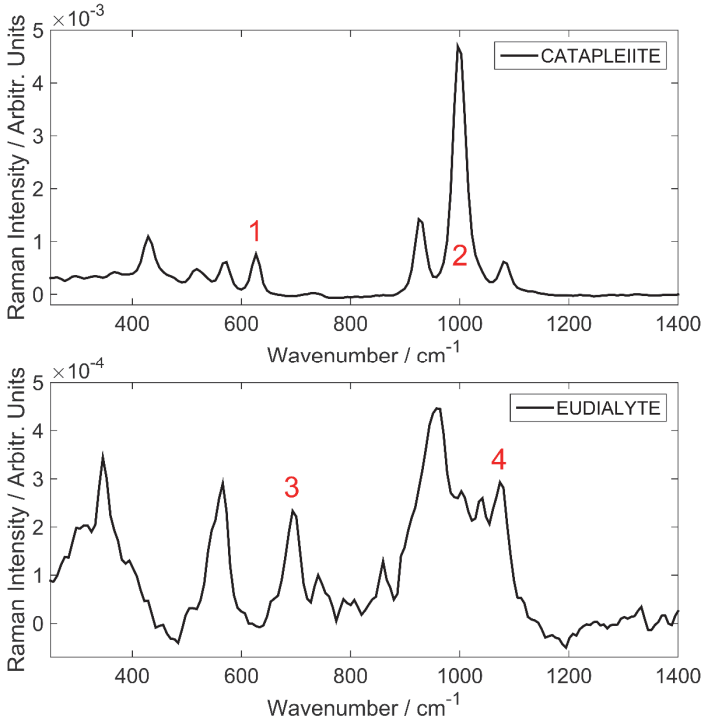

FIGURE 31. Time-gated Raman spectra of catapleiite and eudialyte. Reprinted with permission from *J. Raman Spectrosc.*, 2020, 51, p. 1462. Copyright © 2020 John Wiley & Sons, Ltd.

The sum intensities of peaks marked as 1 and 2 in the catapleiite spectrum and 3 and 4 for the eudialyte spectrum (Fig. 31) were used to construct occurrence maps for both minerals (Fig. 32.). These peaks had minimal interference from overlapping the other silicates' peaks.

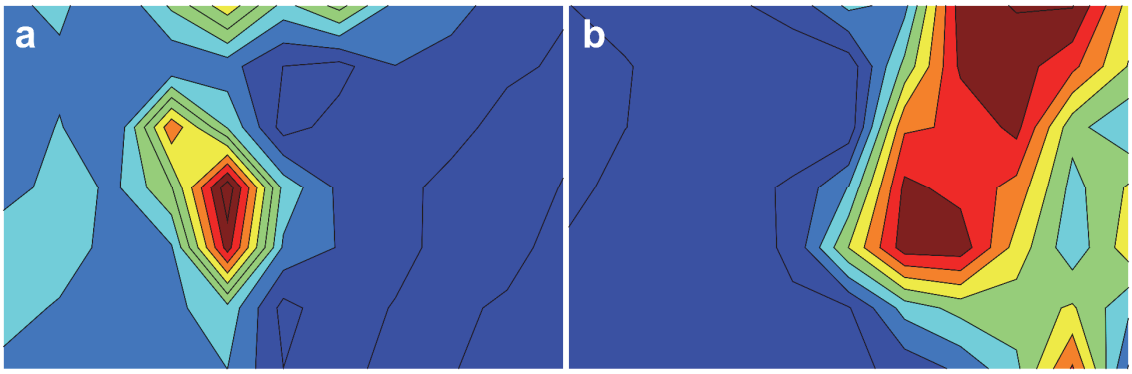

FIGURE 32. Time-gated Raman maps for eudialyte (a) and catapleiite (b), based on peaks presented in Fig. 31. Reprinted with permission from *J. Raman Spectrosc.*, 2020, 51, p. 1462. Copyright © 2020 John Wiley & Sons, Ltd.

The same area was also measured with LIBS for comparison. The grey areas were interpreted as eudialyte and the green areas as catapleiite in the mineralogical map constructed with the SVD approach developed in Paper I (Fig. 33, a). The yttrium distribution map based on the intensity of LIBS line 410.2 nm supported this, because areas of high Y content correspond to the grey eudialyte occurrence (Fig. 33, b). Slightly increased yttrium areas were found in the catapleiite regions. Both LIBS maps correlate to the mineralogical information achieved from the time-gated Raman analysis.

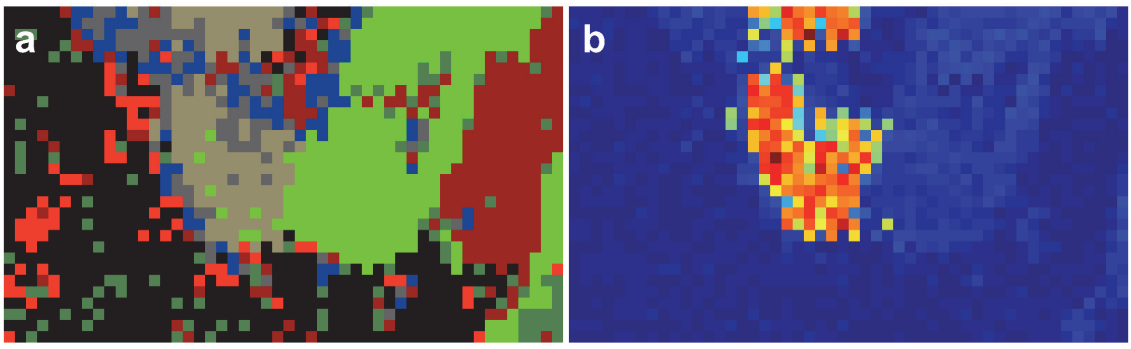

FIGURE 33. LIBS maps constructed with SVD (a) and yttrium line intensity (b) representing mineralogical areas. Reprinted with permission from *J. Raman Spectrosc.*, 2020, 51, p. 1462. Copyright © 2020 John Wiley & Sons, Ltd.

Beneficial information of the investigated sample could be obtained very quickly using time-gated Raman for mineralogical detection and LIBS for chemical analysis. These methods could also be combined in the same setup,[157] and time-gated Raman measurement does not have problems with ambient light.

3.3 Laser-induced luminescence spectroscopy

Paper IV describes the laser-induced luminescence analysis of REE-bearing fluorapatite $Ca_5(PO_4)_3F$ and calcite $CaCO_3$ samples from the Siilinjärvi ultramafic alkaline-carbonatite complex in Finland. The research was performed by changing the excitation wavelength 1 nm at the time in ranges 210–340 nm and 405–535 nm to find the optimal excitation wavelengths for REE luminescence detections. The spectrum was dominated by the strong broad luminescence bands of Ce^{3+} and Eu^{2+} in some excitation ranges. Time-resolved measurements with delay 50 µs and the gate width 500 µs were used to avoid this, which enabled simultaneous detection of several REE peaks, presented as an emission-excitation map in Fig. 34.

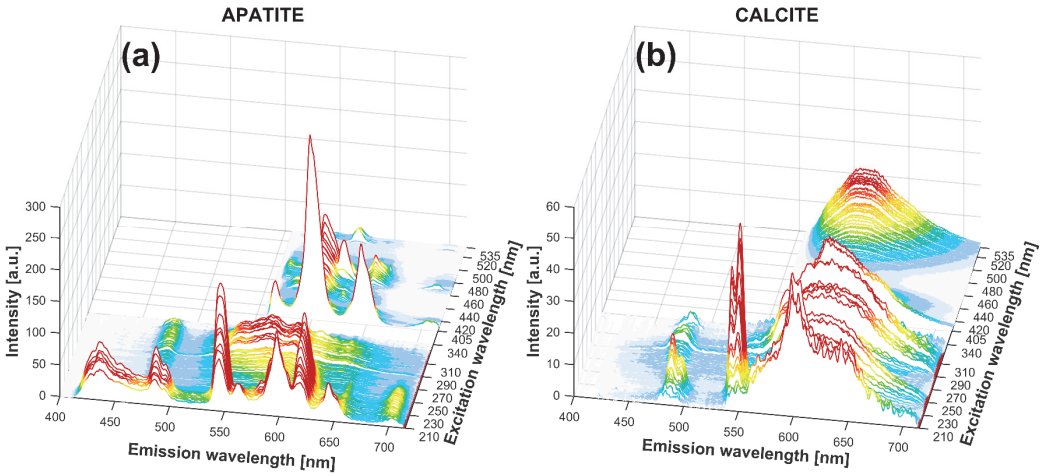

FIGURE 34. Time-resolved luminescence measurements performed in apatite (a) and calcite (b) in the excitation wavelengths of 210–340 nm and 405–535 nm. Reprinted with permission from *J. Lumin.*, 2021, 233. Copyright © 2021 Elsevier B.V.

The luminescence centres of Tb^{3+}, Sm^{3+}, Eu^{3+}, Dy^{3+}, and Nd^{3+} were recognised. A broad Mn^{2+} luminescence band was also observed in both minerals, and especially calcite, in wide excitation ranges, it was blocking the detection of some REE luminescence peaks. Several suitable excitation ranges for different REEs were presented. Examples of the luminescence of Tb^{3+} in apatite and calcite are presented with optimal λ_{ex} 218 nm and 226 nm, respectively (Fig. 35). Another example is that Sm^{3+} luminescence peaks can be detected occurring from two Ca sites in apatite crystal structure, depending on the laser wavelength (Fig. 36). A similar kind of situation was observed with Eu^{3+} in apatite.

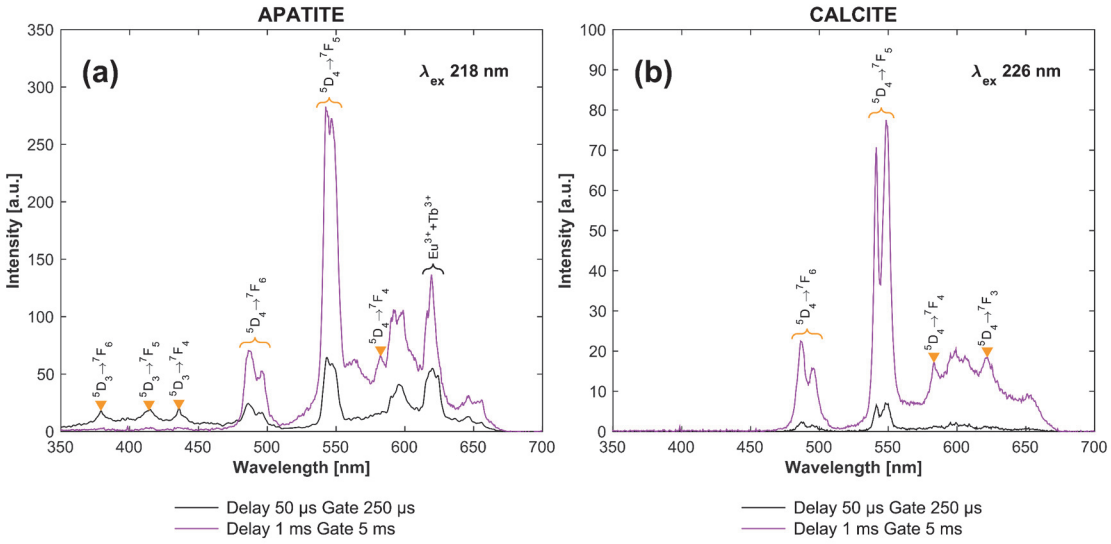

FIGURE 35. Tb^{3+} luminescence in apatite and calcite with the most suitable excitations. Reprinted with permission from *J. Lumin.*, 2021, 233. Copyright © 2021 Elsevier B.V.

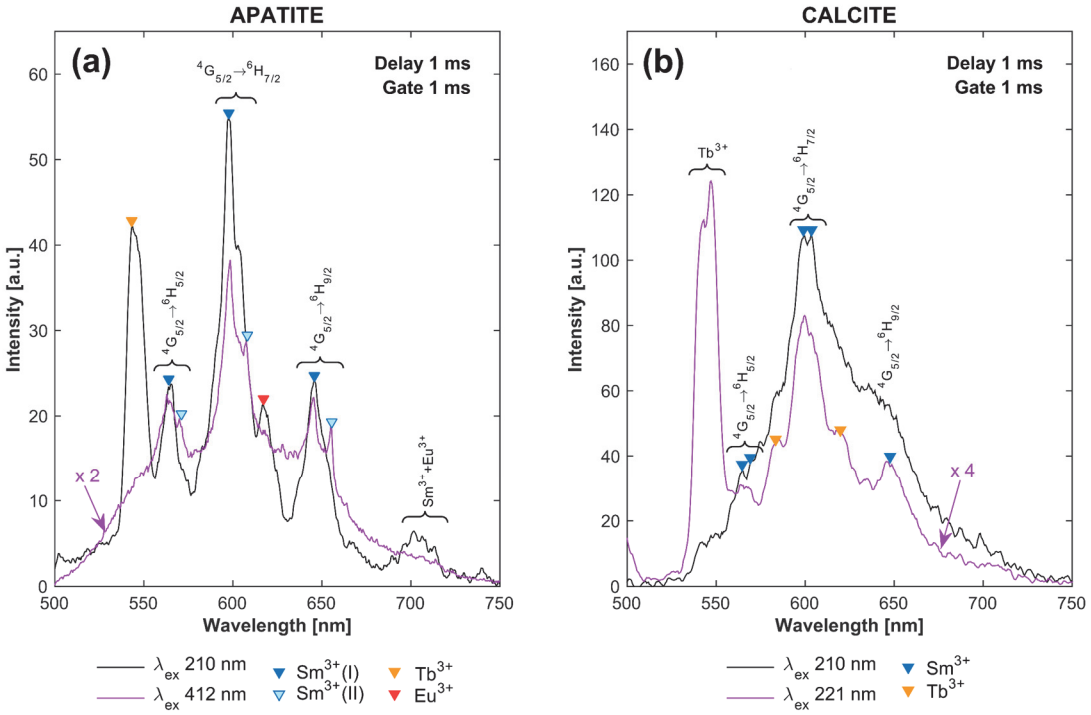

FIGURE 36. Sm^{3+} luminescence peaks in apatite observed in Ca I and Ca II sites in apatite by choosing the right excitation wavelength (a, violet). Sm^{3+} luminescence occurs strongest in calcite with λ_{ex} 210 nm, but intense Mn^{2+} band is blocking the observation of it (b, black). With λ_{ex} 221 nm Mn^{2+} luminescence is decreased and Sm^{3+} peaks can be observed more clearly (b, violet). Reprinted with permission from *J. Lumin.*, 2021, 233. Copyright © 2021 Elsevier B.V.

A main result of this paper is that the excitation range ~220–230 nm seems to be optimal for both minerals, because several REEs show strong luminescence, and disturbance of the Mn^{2+} band is minor. Measurement with a non-gated spectrometer was performed at the optimised terbium excitation to demonstrate this (Fig. 37). The peaks of Eu^{3+} and Sm^{3+} can also be detected from both minerals and Nd^{3+} in apatite. The increase in the background at the beginning of the spectral area within the apatite spectrum is related most likely to the luminescence of Ce^{3+}, but the REE^{3+} peaks can be clearly seen.

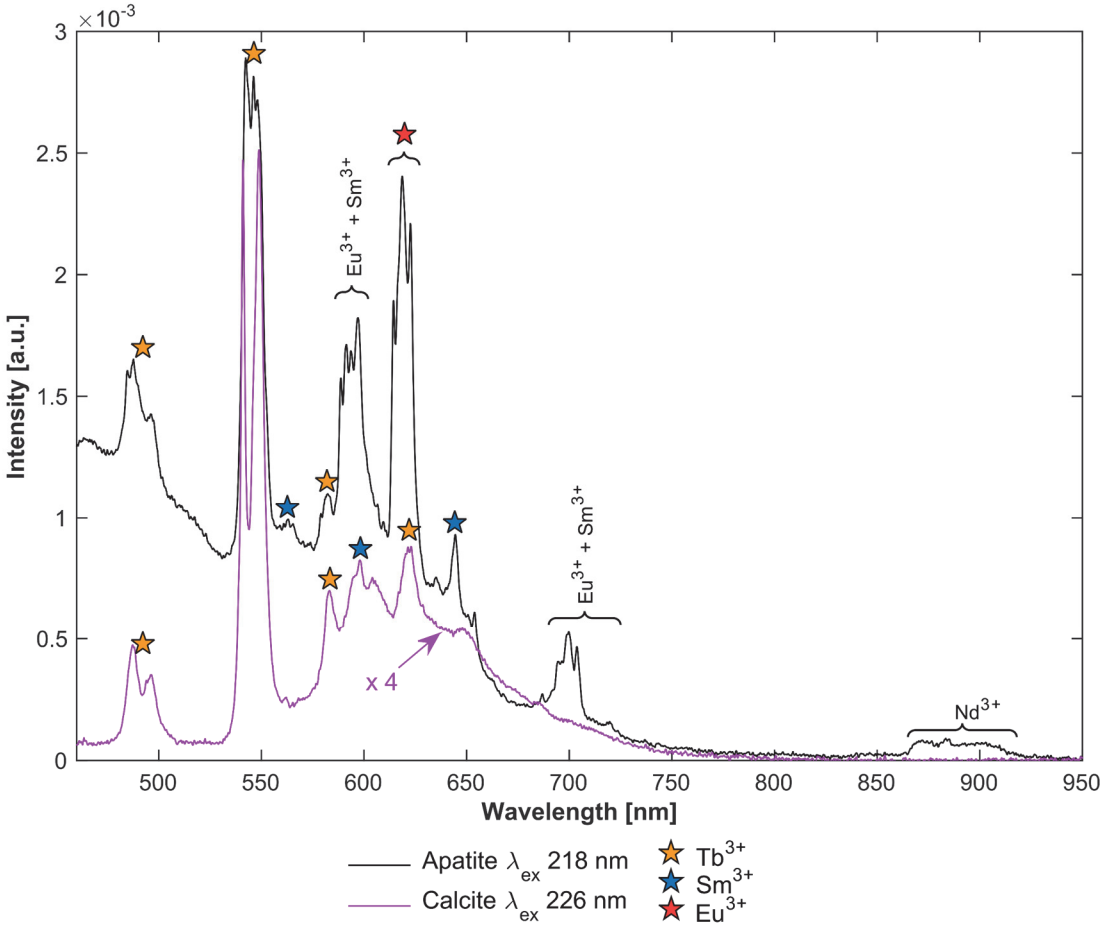

FIGURE 37. Non-gated luminescence measurements for apatite and calcite with the best excitations for Tb^{3+} luminescence. The luminescence peaks of Sm^{3+} and Eu^{3+} can be detected in both minerals and Nd^{3+} in apatite. Reprinted with permission from *J. Lumin.*, 2021, 233. Copyright © 2021 Elsevier B.V.

4 CONCLUSIONS

The successful use of three time-resolved laser-spectroscopic methods is presented in the analysis of rare earth element (REE) and lithium-bearing mineral and rock samples. The strengths of laser-spectroscopic analysis in the geosciences are very fast measurement times, minor sample preparation, and the equipment is less expensive, compared with many other methods. The focus of this thesis was to find measurement parameters suitable for REE and lithium analysis.

Laser-induced breakdown spectroscopy (LIBS) mapping was used to reveal both spatial elemental distributions and mineralogical information of REE and lithium-bearing minerals. The research presented here focused on chemometric mineral separations without large and time-consuming data handling. The main emphasis was placed on sorting the precious ore minerals from gangue.

The complementary information from two laser-spectroscopic methods were utilised side by side when elemental distributions achieved with LIBS were presented together with time-gated Raman data. Time-gated Raman was used to show discovery of the REE-bearing minerals eudialyte and catapleiite based their molecular composition. Time-gated Raman is valuable for verifying the mineral contents of the luminescent rock samples.

Time-resolved laser-induced luminescence can reveal luminescence activators such as REEs, even in very low concentrations. Luminescence activator excitations were analysed from REE-bearing apatite and calcite samples. The most convenient excitations for several REE^{3+} luminescences were also revealed and presented with a non-gated spectrometer.

An example of the spectra measured with these techniques from a luminescent mineral (Fig. 38, upper left) is presented to emphasise the holistic information given by the three laser-spectroscopic methods. LIBS measurement shows the presence of yttrium lines from the proper spectral range presented in paper I (Fig. 38, upper right). This indicates a high possibility that this mineral also contains other REEs due to their similar geochemical behaviour. The self-absorption seen in the calcium lines suggests it is one of the main elements, and a strontium line most likely represents one of the mineral's trace elements. Time-gated Raman spectroscopy shows phosphate vibrations and reveals the

luminescent mineral to be apatite (Fig. 38, lower left). Choosing specific excitation and time parameters for laser-induced luminescence measurement is a key to detecting specific luminescence activators, as presented in paper IV. For example, excitation 248 nm shows Eu^{3+} and Dy^{3+} peaks from apatite (Fig. 38, lower right).

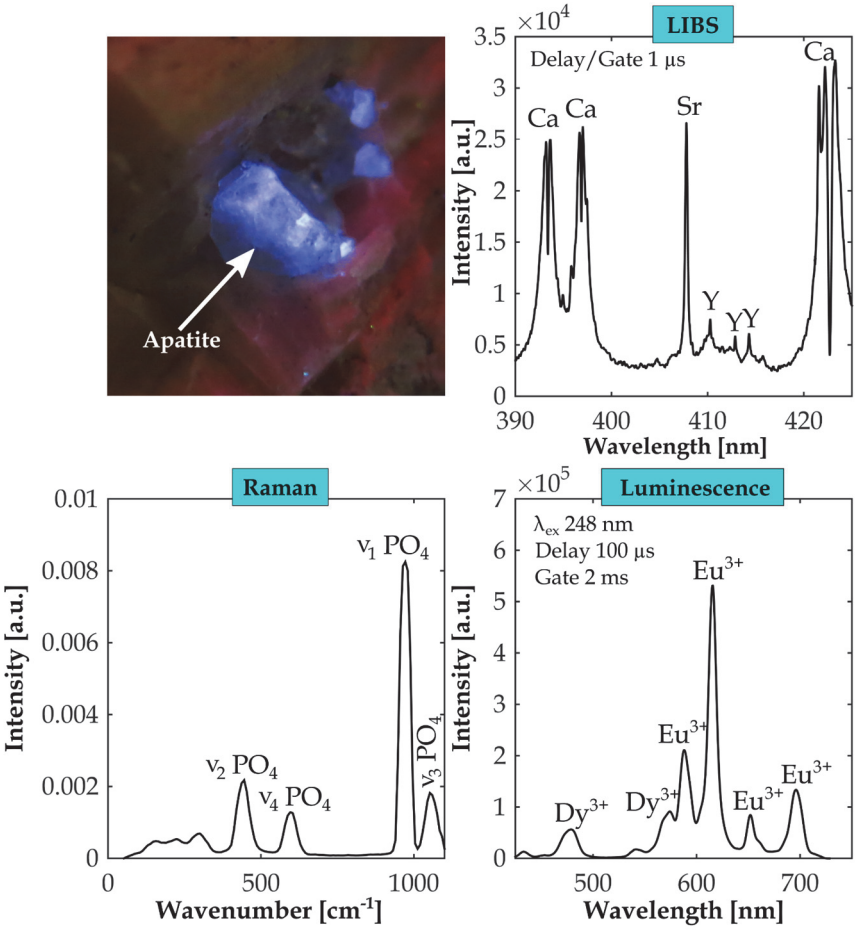

FIGURE 38. Different laser-spectroscopic measurements show complementary information of the luminescent apatite sample (upper left corner). LIBS analysis (right upper corner) shows Ca, Sr, and Y, while time-gated Raman (left lower corner) present vibrations of phosphate, from left to right: ν_2 PO_4 bend, ν_4 PO_4 bend, ν_1 PO_4 symmetric stretch, and ν_3 PO_4 antisymmetric stretch, based on Refs.[158,159] Time-resolved laser-induced luminescence reveals the luminescence activators dysprosium and europium.

In conclusion, elemental and mineralogical information can be obtained directly and quickly from the sample surface with laser-spectroscopic methods. Thus, laser-spectroscopic methods are useful and cost-effective analysis techniques for the analysis needs of the exploration, mining, and beneficiation industries. The fact that the potential exists for these techniques to be modified for use on portable devices, and even combined on the same device, increases their importance as analysis tools in these fields.

REFERENCES

1. European Commission, *Study on the review of the list of Critical Raw Materials - Final Report*, Publications Office of the European Union, Luxembourg, 2020.
2. Kemp, J. F., What is an ore?, *CIM Bull. - Can. Inst. Min. Metall.*, **1909**, *2*, 95–110.
3. Evans, A., *Ore Geology and Industrial Minerals: An Introduction*, 3rd edition, Blackwell Science, 2009.
4. Noetstaller, R., Industrial Minerals: A Technical Review, Washington, 1988.
5. Klein, C. and Philpotts, A., *Earth materials: introduction mineralogy and petrology* , Cambridge University Press, New York, 2013.
6. Rudnick, R. L. and Gao, S., Composition of the Continental Crust. In: Holland, H. D. and Turekian, K. K. (eds.), *Treatise On Geochemistry*, 3rd edition, Elsevier Ltd., 2003, pp. 1–64.
7. Greenwood, N. N. and Earnshaw, A., Silicon. In: *Chemistry of the Elements*, 2nd edition, Butterworth-Heinemann, 2001, pp. 328–366.
8. Macheyeki, A. S.; Li, X.; Kafumu, P. D. and Yuan, F., *Applied Geochemistry: Advances in Mineral Exploration Techniques*, Elsevier, 2020.
9. Brownlow, A. H., *Geochemistry*, 2nd edition, Prentice-Hall, Inc., New Jersey, 1996.
10. Haxel, G. B.; Hedrick, J. B. and Orris, G. J., Rare Earth Elements - Critical Resources for High Technology, 2002.
11. Nickel, E. H., The definition of a mineral, *Can. Mineral.*, **1995**, *33*, 689–690.
12. Back, M.; Biagioni, C.; Birch, W. D.; Blondieau, M.; Bojar, H.-P.; Carter, J.; Ciriotti, M. E.; de Fourestier, J.; Dolivo-Dobrovolsky, D.; Downs, R. T.; Fascio, L.; Ferraris, C.; Ferraris, G.; Garcia, J.; Gault, R.; Godelitsas, A.; Golden, J.; Grew, E. S.; Hålenius, U.; Hawthorne, F. C.; Horváth, L.; Husdal, T.; Imark, C. R.; Lluis, J.; Justo del Campo, J. L.; Kampf, A. R.; Keutsch, F.; Kiechle, E.; Kjellman, J.; Kolitsch, U.; Kostov, R. I.; Krivovichev, V. G.; Kruszewski, Ł.; Lapaire, J.; Larsen, L. M.; Manecki, A.; Márquez-Zavalía, M. F.; Martin, R. F.; Martins, T.; Mees, F.; Menchetti, S.; Mills, S. J.; Missen, O.; Nickolay, D.; Oberti, R.; Ostroumov, M.; Pedersen, R. E.; Pelckmans, H.; Peters, G. A.; Plášil, J.; Revheim, O.; Ritte, A. P.; Robbemond, A.; Roberts, A. C.; Rost, M. M.; Rousseau, M.; Schorn, S.; Schumer, B. N.; Schuminski, J.; Spürgin, S.; Stanco, P.; Stanley, C. J.; Starkey, R.; Szekvőlgyiová, D.; Uher, P.; Unwalla, M.; Vandenberghe, L.; Vighetto, I.; Vignola, P.; Wang, J.; Weissman, J.; Witzke, T. and Zaharia, L., The New IMA List of Minerals: A Work in Progress, Updated March 2021, **2021**, 224.
13. Nickel, E. H. and Grice, J. D., The IMA Commission On New Minerals And Mineral Names: procedures and guidelines on mineral nomenclature, 1998, *Mineral. Petrol.*, **1998**, *64*, 237–263.
14. Hawthorne, F. C.; Ungaretti, L. and Oberti, R., Site populations in minerals; terminology and presentation of results of crystal-structure refinement, *Can. Mineral.*, **1995**, *33*, 907–911.

15. Goldschmidt, V. M., The Principles of Distribution of Chemical Elements in Minerals and Rocks, *Journ. Chem. Soc.*, **1937**, *74*, 655–673.
16. Burns, R. G., *Mineralogical Applications of Crystal Field Theory*, 2nd edition, Cambridge University Press, 1993.
17. Burns, R. G., The partitioning of trace transition elements in crystal structures: a provocative review with applications to mantle geochemistry, *Geochim. Cosmochim. Acta*, **1973**, *37*, 2395–2403.
18. Mills, S. J.; Hatert, F.; Nickel, E. H. and Ferraris, G., The standardisation of mineral group hierarchies: application to recent nomenclature proposals, *Eur. J. Mineral.*, **2009**, *21*, 1073–1080.
19. Hurlbut, C. S. J. and Sharp, W. E., *Dana's Minerals and How to Study Them (After Edward Salisbury Dana)*, 4th edition, John Wiley & Sons, Inc., 1998.
20. Dana, J. D.; Dana, E. S.; Gaines, R. V.; Skinner, H. C. W.; Foord, E. E.; Mason, B. and Rosenzweig, A., *Dana's new mineralogy: the system of mineralogy of James Dwight Dana and Edward Salisbury Dana*, 8th edition, Wiley, 1997.
21. Dana, J. D., *A system of Mineralogy: including an extended treatise on crystallography with an appendix, containing the application of mathematics to crystallographic investigation, and a mineralogical bibliography*, Durrie & Peck and Herrick & Noyes, 1837.
22. Strunz, H., *Mineralogische Tabellen*, 8th edition, Akademische Verlagsgesellschaft, Leipzig, 1982.
23. Strunz, H. and Nickel, E. H., *Strunz mineralogical tables*, 9th edition, Schweizerbart, Stuttgart, 2001.
24. Deer, W. A.; Howie, R. A. and Zussman, J., An Introduction to the Rock-Forming Minerals. 3rd edition, Mineralogical Society of Great Britain and Ireland, 2013.
25. Nasdala, L.; Broska, I.; Harlov, D. E. and Macdonald, R., Recent progress in the study of accessory minerals, *Mineral. Petrol.*, **2017**, 111, 431–433.
26. Roedder, E., *Fluid inclusions*, Mineralogical Society of America, 1984.
27. Brady, N. C. and Weil, R. R., *The Nature and Properties of Soils*, 9th edition, Collier Macmillan Publishers, London, 1984.
28. Koivisto, M., *Jääkaudet*, WSOY, 2004.
29. Connelly, N. G.; Damhus, T.; Hartshorn, R. M. and Hutton, A. T., *Nomenclature of inorganic chemistry - IUPAC recommendations 2005*, Royal Society of Chemistry, 2005.
30. Greenwood, N. N. and Earnshaw, A., The Lanthanide Elements (Z = 58–71). In: *Chemistry of the Elements*, 2nd edition, Butterworth-Heinemann, 2001, pp. 1227–1249.
31. Gupta, C. K. and Krishnamurthy, N., *Extractive Metallurgy of Rare Earths*, CRC Press, Boca Raton, 2005.
32. Greenwood, N. N. and Earnshaw, A., Scandium, Yttrium, Lanthanum and Actinium. In: *Chemistry of the Elements*, 2nd edition, Butterworth-Heinemann, 2001, pp. 944–953.
33. Whittaker, E. J. W. and Muntus, R., Ionic radii for use in geochemistry, *Geochim. Cosmochim. Acta*, **1970**, *34*, 945–956.
34. Hatch, G. P., Dynamics in the global market for rare earths, *Elements*, **2012**,

8, 341–346.
35. Clark, A., Mineralogy of rare earth elements. In: Henderson, P. (ed.), *Rare Earth Element Geochemistry*, Elsevier, 1984, pp. 33–62.
36. Myllymäki, S., *Geochemical pathways of metals from bedrock and soil into water and berries in the Sarvlaxviken area, SE Finland*, 2014.
37. Kanazawa, Y. and Kamitani, M., Rare earth minerals and resources in the world, *J. Alloys Compd.*, Elsevier, 2006, pp. 1339–1343.
38. Goodenough, K. M.; Schilling, J.; Jonsson, E.; Kalvig, P.; Charles, N.; Tuduri, J.; Deady, E. A.; Sadeghi, M.; Schiellerup, H.; Müller, A.; Bertrand, G.; Arvanitidis, N.; Eliopoulos, D. G.; Shaw, R. A.; Thrane, K. and Keulen, N., Europe's rare earth element resource potential: An overview of REE metallogenetic provinces and their geodynamic setting, *Ore Geol. Rev.*, **2016**, *72*, 838–856.
39. Levinson;, A. A., A system of nomenclature for rare-earth minerals, *Am. Mineral.*, **1966**, *51*, 152–158.
40. Chakhmouradian, A. R. and Wall, F., Rare earth elements: Minerals, mines, magnets (and more), *Elements*, **2012**, *8*, 333–340.
41. Long, K. R.; Van Gosen, B. S.; Foley, N. K. and Cordier, D., The Principal Rare Earth Elements Deposits of the United States—A Summary of Domestic Deposits and a Global Perspective, 2010.
42. U.S. Geological Survey, Rare earths. In: *Mineral Commodity Summaries 2021*, 2021, pp. 132–133.
43. U.S. Geological Survey, Scandium. In: *Mineral Commodity Summaries 2021*, 2021, pp. 144–145.
44. U.S. Geological Survey, Yttrium. In: *Mineral Commodity Summaries 2021*, 2021, pp. 186–187.
45. Kynicky, J.; Smith, M. P. and Xu, C., Diversity of rare earth deposits: The key example of China, *Elements*, **2012**, *8*, 361–367.
46. Mariano, A. N. and Mariano, A., Rare earth mining and exploration in North America, *Elements*, **2012**, *8*, 369–376.
47. Sjöqvist, A. S. L.; Cornell, D. H.; Andersen, T.; Erambert, M.; Ek, M. and Leijd, M., Three Compositional Varieties of Rare-Earth Element Ore: Eudialyte-Group Minerals from the Norra Kärr Alkaline Complex, Southern Sweden, *Minerals*, **2013**, *3*, 94–120.
48. Ahonen, S.; Arvanitidis, N.; Auer, A.; Baillet, E.; Bellato, N.; Binnemans, K.; Blengini, G. A.; Bonato, D.; Brouwer, E.; Brower, S.; Buchert, M.; Bütikofer, R.; Cavaco Viegas, H.; Cescutti, J.-P.; Chmielarz, A.; Christmann, P.; Claessen, C.; Cozigou, G.; De Oliveira, D.; Deady, E.; Denis, R.; Diaz Pulido, F.; Edvardsson, M.; Fontana, D.; Forsgren, C.; Gabriel, J. C.; Gauss, R.; Gernuks, M.; Gibbon, A.; Gislev, M.; Goddin, J. R. J.; Gomez, M.; Gonçalves, M.; Goodenough, K.; Graupner, T.; Grohol, M.; Gutfleisch, O.; Gutzmer, J.; Hejny, H.; Holmstrom, H.; Hredzak, S.; Jernström, E.; Jha, A.; Kalvig, P.; Kefferputz, R.; Kennedy, D.; Kooroshy, J.; La Marca, F.; Larcher, O.; Leijd, M.; Lenting, H.; Lindner, F.; Loois, E.; Lopez Vicente, P.; Lusty, P.; Makanyire, T.; Millet, P.; Morales, A.; Nemeth, Z.; Ocera, A.; Offerman, E.;

Papavasileiou, K.; Paspaliaris, I.; Peck, D. P.; Pellegrini, M.; Pellet-Rostaing, S.; Peuker, U.; Quix, M.; Räisänen, M. L.; Redondo, E.; Revest, X.; Rollat, A.; Salminen, J.; Sanchez-Segad, S.; Santavaara, I.; Schmidt, G.; Sheridan, R.; Sjöqvist, A.; Solar, S.; Sundgren, M.; Tattam, C.; Taxiarchou, M.; Taylor, M.; Tiess, G.; Tukker, A.; van Der Eijk, C.; van Maercke, A.; van Veen, J.; Vecchione, S.; Vrancken, K.; Vu, H.; Walton, A.; Westin, E.; Wittenberg, A.; Wotruba, H.; Ye, G. and Zaleski, S., *Strengthening the European Rare Earths Supply-chain - Challenges and Policy Options: A report by the European rare earths competency network (ERECON)*, European Comission, 2015.

49. Al-Ani, T.; Molnár, F.; Lintinen, P. and Leinonen, S., Geology and Mineralogy of Rare Earth Elements Deposits and Occurrences in Finland, *Minerals*, **2018**, *8*, 356.
50. Hornig-Kjarsgaard, I., Rare Earth Elements in Sovitic Carbonatites and their Mineral Phases, *J. Petrol.*, **1998**, *39*, 2105–2121.
51. Puustinen, K., *Geology of the Siilinjärvi Carbonatite Complex, Eastern Finland*, Geologinen tutkimuslaitos, Otaniemi, 1971.
52. Al-Ani, T., Mineralogy and Petrography of Siilinjärvi Carbonatite and Glimmerite Rocks, Eastern Finland, 2013.
53. Gibson, M. and Parkinson, I., Once Ignored on the Periodic Table, Don't Ignore Them Now: A Rare Earth Element Industry Overview, 8, Toronto, 2011.
54. Greenwood, N. N. and Earnshaw, A., Lithium, Sodium, Potassium, Rubidium, Caesium and Francium. In: *Chemistry of the Elements*, 2nd edition, Butterworth-Heinemann, 2001, pp. 68–106.
55. Colton, J. W., Recovery of Lithium from Complex Silicates. In: *Advances in Chemistry: Handling and uses of the Alkali Metals*, American Chemical Society:, Washington DC, 1957, vol. 1, pp. 3–8.
56. Gourcerol, B.; Gloaguen, E.; Melleton, J.; Tuduri, J. and Galiegue, X., Re-assessing the European lithium resource potential – A review of hard-rock resources and metallogeny, *Ore Geol. Rev.*, **2019**, 109, 494–519.
57. Tadesse, B.; Makuei, F.; Albijanic, B. and Dyer, L., The beneficiation of lithium minerals from hard rock ores: A review, *Miner. Eng.*, **2019**, 131, 170–184.
58. Kesler, S. E.; Gruber, P. W.; Medina, P. A.; Keoleian, G. A.; Everson, M. P. and Wallington, T. J., Global lithium resources: Relative importance of pegmatite, brine and other deposits, *Ore Geol. Rev.*, **2012**, 48, 55–69.
59. Peiró, L. T.; Méndez, V. G. and Ayres, R. U., Lithium: Sources, Production, Uses, and Recovery Outlook, *J. Miner. Met. Mater. Soc.*, **2013**, *65*, 986–996.
60. Grosjean, C.; Herrera Miranda, P.; Perrin, M. and Poggi, P., Assessment of world lithium resources and consequences of their geographic distribution on the expected development of the electric vehicle industry, *Renew. Sustain. Energy Rev.*, **2012**, 16, 1735–1744.
61. Mohr, S. H.; Mudd, G. M. and Giurco, D., Lithium Resources and Production: Critical Assessment and Global Projections, *Minerals*, **2012**, *2*, 65–84.
62. U.S. Geological Survey, Lithium. In: *Mineral Commodity Summaries 2021*,

2021, pp. 98–99.
63. Tadesse, B.; Makuei, F.; Albijanic, B. and Dyer, L., The beneficiation of lithium minerals from hard rock ores: A review, *Miner. Eng.*, **2019**, *131*, 170–184.
64. Rasilainen, K.; Eilu, P.; Ahtola, T.; Halkoaho, T.; Kärkkäinen, N.; Kuusela, J.; Lintinen, P. and Törmänen, T., Quantitative assessment of undiscovered resources in lithium-caesium-tantalum pegmatite-hosted deposits in Finland, *Bulletin*, **2018**, *406*.
65. Sarapää, O.; Lauri, L. S.; Ahtola, T.; Al-Ani, T.; Grönholm, S.; Kärkkäinen, N.; Lintinen, P.; Torppa, A. & and Turunen, P., *Discovery potential of hi-tech metals and critical minerals in Finland*, Geological Survey of Finland, 2015.
66. Jaskula, B. W., Minerals Yearbook: Lithium, 2017.
67. Zawisza, B.; Pytlakowska, K.; Feist, B.; Polowniak, M.; Kita, A. and Sitko, R., Determination of rare earth elements by spectroscopic techniques: A review, *J. Anal. At. Spectrom.*, **2011**, 26, 2373–2390.
68. Fitton, G., X-ray fluorescence spectrometry. In: Gill, R. (ed.), *Modern Analytical Geochemistry: An Introduction to Quantitative Chemical Analysis Techniques for Earth, Environmental and Materials Scientists*, Taylor and Francis Inc., 2014, pp. 87–115.
69. Walsh, J. N., Inductively coupled plasma-atomic emission spectrometry (ICP-AES). In: Gill, R. (ed.), *Modern Analytical Geochemistry: An Introduction to Quantitative Chemical Analysis Techniques for Earth, Environmental and Materials Scientists*, Taylor and Francis Inc., London & New York, 2014, pp. 41–66.
70. Jarvis, K. E., Inductively coupled plasma-mass spectrometry. In: Gill, R. (ed.), *Modern Analytical Geochemistry: An Introduction to Quantitative Chemical Analysis Techniques for Earth, Environmental and Materials Scientists*, Taylor and Francis Inc., London & New York, 2014, pp. 171–187.
71. Chirinos, J. R.; Oropeza, D. D.; Gonzalez, J. J.; Hou, H.; Morey, M.; Zorba, V. and Russo, R. E., Simultaneous 3-dimensional elemental imaging with LIBS and LA-ICP-MS, *J. Anal. At. Spectrom.*, Royal Society of Chemistry, 2014, pp. 1292–1298.
72. Kilburn, M. R. and Wacey, D., Nanoscale Secondary Ion Mass Spectrometry (NanoSIMS) as an Analytical Tool in the Geosciences. In: Grice, K. (ed.), *Principles and Practice of Analytical Techniques in Geosciences*, Royal Society of Chemistry , Cambridge, 2015, pp. 1–34.
73. Harmon, R.; Lawley, C.; Watts, J.; Harraden, C.; Somers, A. and Hark, R., Laser-Induced Breakdown Spectroscopy—An Emerging Analytical Tool for Mineral Exploration, *Minerals*, **2019**, *9*, 718.
74. Parry, S. J., Neutron activation analysis. In: Gill, R. (ed.), *Modern Analytical Geochemistry: An Introduction to Quantitative Chemical Analysis Techniques for Earth, Environmental and Materials Scientists*, Taylor and Francis Inc., London & New York, 2014, pp. 116–134.
75. Chew, D.; Drost, K.; Marsh, J. H. and Petrus, J. A., LA-ICP-MS imaging in the geosciences and its applications to geochronology, *Chem. Geol.*, **2021**, *559*, 119917.

76. Li, X. H. and Li, Q. L., Major advances in microbeam analytical techniques and their applications in Earth Science, *Sci. Bull.*, **2016**, *61*, 1785–1787.
77. Atkins, P. and De Paula, J., *Atkins' Physical chemistry*, 8th edition, W. H. Freeman and Company, New York, 2006.
78. Hollas, J. M., *Modern Spectroscopy*, 4th edition, John Wiley & Sons, Chichester, 2004.
79. Svelto, O., *Principles of lasers*, 5th edition, Springer US, 2010.
80. Svelto, O.; Longhi, S.; Della Valle, G.; Huber, G.; Kück, S.; Pollnau, M.; Hillmer, H.; Kusserow, T.; Engelbrecht, R.; Rohlfing (deceased), F.; Kaiser, J.; Malz, R.; Marowsky, G.; Mann, K.; Simon, P.; Rhodes, C. K.; Duarte, F. J.; Borsutzky, A.; L'huillier, J. A.; Sigrist, M. W.; Wächter, H.; Saldin, E.; Schneidmiller, E.; Yurkov, M.; Sauerbrey, R.; Hein, J.; Gianella, M.; Helmcke, J.; Midorikawa, K.; Riehle, F.; Steinberg, S. and Brand, H., Lasers and Coherent Light Sources. In: Träger, F. (ed.), *Springer Handbook of Lasers and Optics*, Springer Berlin Heidelberg, Berlin, Heidelberg, 2012, pp. 641–1046.
81. Telle, H. H.; González Ureña, A. and Donovan, R. J., *Laser Chemistry: Spectroscopy, Dynamics and Applications*, John Wiley & Sons, Ltd, Chichester, 2007.
82. Noll, R., *Laser-induced breakdown spectroscopy: Fundamentals and applications*, Springer Berlin Heidelberg, 2012.
83. Demtröder, W., *Laser Spectroscopy -Volume 1: Basic Principles*, 4th edition, Springer-Verlag, Berlin Heidelberg, 2008.
84. Chatwal, G. R. and Anand, S. K., *Spectroscopy : (Atomic and molecular)*, Rev. ed, Himalaya Pub. House, Mumbai, 2009.
85. Becker-Ross, H. and Florek, S. V., Echelle spectrometers and charge-coupled devices, *Spectrochim. Acta - Part B At. Spectrosc.*, **1997**, *52*, 1367–1375.
86. Abramczyk, H., *Introduction to laser spectroscopy*, 1st ed, Elsevier Science, Amsterdam, 2005.
87. Bruschini, C.; Homulle, H.; Antolovic, I. M.; Burri, S. and Charbon, E., Single-photon avalanche diode imagers in biophotonics: review and outlook, *Light Sci. Appl.*, **2019**, *8*, 2047–7538.
88. Nissinen, I.; Nissinen, J.; Keranen, P.; Stoppa, D. and Kostamovaara, J., A 16 x 256 SPAD Line Detector with a 50-ps, 3-bit, 256-Channel Time-to-Digital Converter for Raman Spectroscopy, *IEEE Sens. J.*, **2018**, *18*, 3789–3798.
89. Cremers, D. A. and Radziemski, L. J., *Handbook of laser-induced breakdown spectroscopy*, 2nd edition, John Wiley & Sons, Ltd, Chichester, West Sussex, U.K., 2013.
90. Fabre, C.; Devismes, D.; Moncayo, S.; Pelascini, F.; Trichard, F.; Lecomte, A.; Bousquet, B.; Cauzid, J. and Motto-Ros, V., Elemental imaging by laser-induced breakdown spectroscopy for the geological characterization of minerals, *J. Anal. At. Spectrom.*, **2018**, *33*, 1345–1353.
91. Fabre, C., Advances in Laser-Induced Breakdown Spectroscopy analysis for geology: A critical review, *Spectrochim. Acta - Part B At. Spectrosc.*, **2020**,

166, 105799.

92. McMillan, N. J.; Rees, S.; Kochelek, K. and McManus, C., Geological Applications of Laser-Induced Breakdown Spectroscopy, *Geostand. Geoanalytical Res.*, **2014**, *38*, 329–343.
93. Harmon, R. S.; Russo, R. E. and Hark, R. R., Applications of laser-induced breakdown spectroscopy for geochemical and environmental analysis: A comprehensive review, *Spectrochim. Acta - Part B At. Spectrosc.*, **2013**, 87, 11–26.
94. Harmon, R. S.; Shughrue, K. M.; Remus, J. J.; Wise, M. A.; East, L. J. and Hark, R. R., Can the provenance of the conflict minerals columbite and tantalite be ascertained by laser-induced breakdown spectroscopy?, *Anal. Bioanal. Chem.*, **2011**, *400*, 3377–3382.
95. Harmon, R. S. and Senesi, G. S., Laser-Induced Breakdown Spectroscopy – A geochemical tool for the 21st century, *Appl. Geochemistry*, **2021**, 128, 104929.
96. Wiens, R. C.; Maurice, S.; Barraclough, B.; Saccoccio, M.; Barkley, W. C.; Bell, J. F.; Bender, S.; Bernardin, J.; Blaney, D.; Blank, J.; Bouyé, M.; Bridges, N.; Bultman, N.; Caïs, P.; Clanton, R. C.; Clark, B.; Clegg, S.; Cousin, A.; Cremers, D.; Cros, A.; Deflores, L.; Delapp, D.; Dingler, R.; D'Uston, C.; Darby Dyar, M.; Elliott, T.; Enemark, D.; Fabre, C.; Flores, M.; Forni, O.; Gasnault, O.; Hale, T.; Hays, C.; Herkenhoff, K.; Kan, E.; Kirkland, L.; Kouach, D.; Landis, D.; Langevin, Y.; Lanza, N.; Larocca, F.; Lasue, J.; Latino, J.; Limonadi, D.; Lindensmith, C.; Little, C.; Mangold, N.; Manhes, G.; Mauchien, P.; McKay, C.; Miller, E.; Mooney, J.; Morris, R. V.; Morrison, L.; Nelson, T.; Newsom, H.; Ollila, A.; Ott, M.; Pares, L.; Perez, R.; Poitrasson, F.; Provost, C.; Reiter, J. W.; Roberts, T.; Romero, F.; Sautter, V.; Salazar, S.; Simmonds, J. J.; Stiglich, R.; Storms, S.; Striebig, N.; Thocaven, J. J.; Trujillo, T.; Ulibarri, M.; Vaniman, D.; Warner, N.; Waterbury, R.; Whitaker, R.; Witt, J. and Wong-Swanson, B., The ChemCam instrument suite on the Mars Science Laboratory (MSL) rover: Body unit and combined system tests, *Space Sci. Rev.*, **2012**, *170*, 167–227.
97. Wiens, R. C.; Maurice, S.; Robinson, S. H.; Nelson, A. E.; Cais, P.; Bernardi, P.; Newell, R. T.; Clegg, S.; Sharma, S. K.; Storms, S.; Deming, J.; Beckman, D.; Ollila, A. M.; Gasnault, O.; Anderson, R. B.; André, Y.; Michael Angel, S.; Arana, G.; Auden, E.; Beck, P.; Becker, J.; Benzerara, K.; Bernard, S.; Beyssac, O.; Borges, L.; Bousquet, B.; Boyd, K.; Caffrey, M.; Carlson, J.; Castro, K.; Celis, J.; Chide, B.; Clark, K.; Cloutis, E.; Cordoba, E. C.; Cousin, A.; Dale, M.; Deflores, L.; Delapp, D.; Deleuze, M.; Dirmyer, M.; Donny, C.; Dromart, G.; George Duran, M.; Egan, M.; Ervin, J.; Fabre, C.; Fau, A.; Fischer, W.; Forni, O.; Fouchet, T.; Fresquez, R.; Frydenvang, J.; Gasway, D.; Gontijo, I.; Grotzinger, J.; Jacob, X.; Jacquinod, S.; Johnson, J. R.; Klisiewicz, R. A.; Lake, J.; Lanza, N.; Laserna, J.; Lasue, J.; Le Mouélic, S.; Legett, C.; Leveille, R.; Lewin, E.; Lopez-Reyes, G.; Lorenz, R.; Lorigny, E.; Love, S. P.; Lucero, B.; Madariaga, J. M.; Madsen, M.; Madsen, S.; Mangold, N.; Manrique, J. A.; Martinez, J. P.; Martinez-Frias, J.; McCabe, K. P.;

McConnochie, T. H.; McGlown, J. M.; McLennan, S. M.; Melikechi, N.; Meslin, P. Y.; Michel, J. M.; Mimoun, D.; Misra, A.; Montagnac, G.; Montmessin, F.; Mousset, V.; Murdoch, N.; Newsom, H.; Ott, L. A.; Ousnamer, Z. R.; Pares, L.; Parot, Y.; Pawluczyk, R.; Glen Peterson, C.; Pilleri, P.; Pinet, P.; Pont, G.; Poulet, F.; Provost, C.; Quertier, B.; Quinn, H.; Rapin, W.; Reess, J. M.; Regan, A. H.; Reyes-Newell, A. L.; Romano, P. J.; Royer, C.; Rull, F.; Sandoval, B.; Sarrao, J. H.; Sautter, V.; Schoppers, M. J.; Schröder, S.; Seitz, D.; Shepherd, T.; Sobron, P.; Dubois, B.; Sridhar, V.; Toplis, M. J.; Torre-Fdez, I.; Trettel, I. A.; Underwood, M.; Valdez, A.; Valdez, J.; Venhaus, D. and Willis, P., The SuperCam Instrument Suite on the NASA Mars 2020 Rover: Body Unit and Combined System Tests, *Space Sci. Rev.*, **2021**, 217, 1–87.

98. Fabre, C.; Boiron, M. C.; Dubessy, J.; Cathelineau, M. and Banks, D. A., Palaeofluid chemistry of a single fluid event: A bulk and in-situ multi-technique analysis (LIBS, Raman spectroscopy) of an Alpine fluid (Mont-Blanc), *Chem. Geol.*, **2002**, *182*, 249–264.
99. Stipe, C. B.; Miller, A. L.; Brown, J.; Guevara, E. and Cauda, E., Evaluation of laser-induced breakdown spectroscopy (LIBS) for measurement of silica on filter samples of coal dust, *Appl. Spectrosc.*, **2012**, *66*, 1286–1293.
100. Tognoni, E.; Cristoforetti, G.; Legnaioli, S. and Palleschi, V., Calibration-Free Laser-Induced Breakdown Spectroscopy: State of the art, *Spectrochim. Acta - Part B At. Spectrosc.*, **2010**, 65, 1–14.
101. Praher, B.; Palleschi, V.; Viskup, R.; Heitz, J. and Pedarnig, J. D., Calibration free laser-induced breakdown spectroscopy of oxide materials, *Spectrochim. Acta - Part B At. Spectrosc.*, Elsevier, 2010, pp. 671–679.
102. Sweetapple, M. T. and Tassios, S., Laser-induced breakdown spectroscopy (LIBS) as a tool for in situ mapping and textural interpretation of lithium in pegmatite minerals, *Am. Mineral.*, **2015**, *100*, 2141–2151.
103. Fabre, C.; Boiron, M. C.; Dubessy, J.; Chabiron, A.; Charoy, B. and Martin Crespo, T., Advances in lithium analysis in solids by means of laser-induced breakdown spectroscopy: An exploratory study, *Geochim. Cosmochim. Acta*, **2002**, *66*, 1401–1407.
104. Weast, R. C., *CRC Handbook of Chemistry & Physics*, 56th edition, CRC Press Inc., Cleveland, Ohio, 1974.
105. Smith, E. and Dent, G., *Modern Raman Spectroscopy: A Practical Approach*, John Wiley & Sons Ltd, Hoboken, New Jersey, 2019, vol. 2.
106. Neuville, D.; de Ligny, D. and Henderson, G., Advances in Raman Spectroscopy Applied to Earth and Material Sciences. In: Henderson, G.; Neuville, D. and Downs, R. (eds.), *Spectroscopic Methods in Mineralogy and Material Sciences*, De Gruyter, Inc., 2014, pp. 509–541.
107. Nasdala, L.; Smith, D. C.; Kaindl, R. and Ziemann, M. A., Raman spectroscopy: Analytical perspectives in mineralogical research. In: Beran, A. and Libowitzky, E. (eds.), *Spectroscopic methods in mineralogy*, Mineralogical Society of Great Britain and Ireland, Germany, 2004, pp. 281–343.

108. Bischoff, W. D.; Sharma, S. K. and MacKenzie, F. T., Carbonate ion disorder in synthetic and biogenic magnesian calcites: a Raman spectral study, *Am. Mineral.*, **1985**, *70*, 581–589.
109. Dufresne, W. J. B.; Rufledt, C. J. and Marshall, C. P., Raman spectroscopy of the eight natural carbonate minerals of calcite structure, *J. Raman Spectrosc.*, **2018**, *49*, 1999–2007.
110. Rutt, H. N. and Nicola, J. H., Raman spectra of carbonates of calcite structure, *J. Phys. C Solid State Phys.*, **1974**, *7*, 4522–4528.
111. Krishnamurti, D., Raman spectrum of magnesite, *Proc. Indian Acad. Sci. - Sect. A*, **1956**, *43*, 210–212.
112. Lafuente, B.; Downs, R. T.; Yang, H. and Stone, N., The power of databases: the RRUFF project. In: Highlights in Mineralogical Crystallography, https://rruff.info/ (4.2.2021).
113. Nasdala, L. and Schmidt, C., Applications of Raman spectroscopy in mineralogy and geochemistry, *Elements*, **2020**, *16*, 99–104.
114. Frezzotti, M. L.; Tecce, F. and Casagli, A., Raman spectroscopy for fluid inclusion analysis, *J. Geochemical Explor.*, **2012**, *112*, 1–20.
115. Bodnar, R. J. and Frezzotti, M. L., Microscale chemistry: Raman analysis of fluid and melt inclusions, *Elements*, **2020**, *16*, 93–98.
116. Bersani, D. and Lottici, P. P., Applications of Raman spectroscopy to gemology, *Anal. Bioanal. Chem.*, Springer, 2010, pp. 2631–2646.
117. Sharma, S. K.; Misra, A. K.; Lucey, P. G. and Lentz, R. C. F., A combined remote Raman and LIBS instrument for characterizing minerals with 532 nm laser excitation, *Spectrochim. Acta - Part A Mol. Biomol. Spectrosc.*, **2009**, *73*, 468–476.
118. Panczer, G.; De Ligny, D.; Mendoza, C.; Gaft, M.; Seydoux-Guillaume, A. M. and Wang, X., Raman and fluorescence, *Eur. Mineral. Union Notes Mineral.*, **2012**, *12*, 61–82.
119. Tuschel, D., Selecting an Excitation Wavelength for Raman Spectroscopy, *Spectroscopy*, **2016**, *31*, 11–17.
120. Parson, W. W., Raman Scattering and Other Multiphoton Processes. In: *Modern Optical Spectroscopy*, Springer Berlin Heidelberg, 2009, pp. 417–445.
121. Gaft, M.; Reisfeld, R. and Panczer, G., *Modern luminescence spectroscopy of minerals and materials*, Springer, Heidelberg, 2005.
122. Gaft, M.; Reisfeld, R. and Panczer, G., *Modern Luminescence Spectroscopy of Minerals and Materials*, 2nd edition, Springer Mineralogy, 2015.
123. Rakovan, J. and Waychunas, G., Luminescence in minerals, *Mineral. Rec.*, **1996**, *27*, 7–20.
124. Nasdala, L.; Götze, J.; Hanchar, J. M.; Gaft, M. and Krbetschek, M. R., Luminescence techniques in Earth Sciences. In: *Spectroscopic methods in mineralogy*, Mineralogical Society of Great Britain and Ireland, Germany, 2004, pp. 43–91.
125. Lakowicz, J. R., *Principles of Fluorescence Spectroscopy*, 3rd edition, Springer, New York, NY, 2006.
126. MacRae, C. M. and Wilson, N. C., Luminescence database I - Minerals and

materials, *Microsc. Microanal.*, **2008**, *14*, 184–204.
127. Gorobets, B. and Rogojine, A., *Luminescent spectra of minerals*, RPC VIMS, Moscow, 2001.
128. Blasse, G. and Grabmaier, B. C., *Luminescent materials*, Springer-Verlag, Berlin/Heidelberg, 1994.
129. Gaft, M.; Panczer, G.; Reisfeld, R. and Uspensky, E., Laser-induced time-resolved luminescence as a tool for rare-earth element identification in minerals, *Phys. Chem. Miner.*, **2001**, *28*, 347–363.
130. Bünzli, J.-C. G. and Eliseeva, S. V., Basics of Lanthanide Photophysics. In: Hänninen P. and Härmä H. (eds.), *Lanthanide Luminescence. Springer Series on Fluorescence (Methods and Applications)*, Springer, Berlin, Heidelberg, 2010, vol. 7, pp. 1–45.
131. Adamson, O. J., *The Petrology of the Norra Kärr District - An Occurrence of Alkaline Rocks in Southern Sweden*, Geologiska Föreningens i Stockholm Förhandlingar, Stockholm, 1944, vol. 66.
132. Saxon, M.; Leijd, M.; Forrester, K. and Berg, J., Geology, mineralogy, and metallurgical processing of the Norra Kärr heavy REE deposit, *Symp. Strateg. Crit. Mater. Proceedings, Novemb. 13-14, 2015, Victoria, Br. Columbia*, **2015**, 97–107.
133. Kuusela, J.; Ahtola, T.; Koistinen, E.; Seppänen, H.; Hatakka, T. and Lohva, J., Report of investigations on the Rapasaaret lithium pegmatite deposit in Kaustinen-Kokkola, Western Finland, 2011.
134. Zhang, T.; Tang, H. and Li, H., Chemometrics in laser-induced breakdown spectroscopy, *J. Chemom.*, **2018**, *32*, e2983.
135. Gottfried, J. L.; Harmon, R. S.; De Lucia, F. C. and Miziolek, A. W., Multivariate analysis of laser-induced breakdown spectroscopy chemical signatures for geomaterial classification, *Spectrochim. Acta - Part B At. Spectrosc.*, **2009**, *64*, 1009–1019.
136. Clegg, S. M.; Sklute, E.; Dyar, M. D.; Barefield, J. E. and Wiens, R. C., Multivariate analysis of remote laser-induced breakdown spectroscopy spectra using partial least squares, principal component analysis, and related techniques, *Spectrochim. Acta - Part B At. Spectrosc.*, **2009**, *64*, 79–88.
137. Pořízka, P.; Klus, J.; Képeš, E.; Prochazka, D.; Hahn, D. W. and Kaiser, J., On the utilization of principal component analysis in laser-induced breakdown spectroscopy data analysis, a review, *Spectrochim. Acta - Part B At. Spectrosc.*, **2018**, 148, 65–82.
138. Bousquet, B.; Sirven, J. B. and Canioni, L., Towards quantitative laser-induced breakdown spectroscopy analysis of soil samples, *Spectrochim. Acta - Part B At. Spectrosc.*, **2007**, *62*, 1582–1589.
139. Klus, J.; Mikysek, P.; Prochazka, D.; Pořízka, P.; Prochazková, P.; Novotný, J.; Trojek, T.; Novotný, K.; Slobodník, M. and Kaiser, J., Multivariate approach to the chemical mapping of uranium in sandstone-hosted uranium ores analyzed using double pulse Laser-Induced Breakdown Spectroscopy, *Spectrochim. Acta - Part B At. Spectrosc.*, **2016**, *123*, 143–149.
140. McManus, C. E.; McMillan, N. J.; Harmon, R. S.; Whitmore, R. C.; De Lucia,

F. C. and Miziolek, A. W., Use of laser induced breakdown spectroscopy in the determination of gem provenance: Beryls, *Appl. Opt.*, **2008**, *47*, G72–G79.
141. Alvey, D. C.; Morton, K.; Harmon, R. S.; Gottfried, J. L.; Remus, J. J.; Collins, L. M. and Wise, M. A., Laser-induced breakdown spectroscopy-based geochemical fingerprinting for the rapid analysis and discrimination of minerals: The example of garnet, *Appl. Opt.*, **2010**, *49*, C168–C180.
142. Death, D. L.; Cunningham, A. P. and Pollard, L. J., Multi-element and mineralogical analysis of mineral ores using laser induced breakdown spectroscopy and chemometric analysis, *Spectrochim. Acta - Part B At. Spectrosc.*, **2009**, *64*, 1048–1058.
143. Ollila, A. M.; Lasue, J.; Newsom, H. E.; Multari, R. A.; Wiens, R. C. and Clegg, S. M., Comparison of two partial least squares-discriminant analysis algorithms for identifying geological samples with the ChemCam laser-induced breakdown spectroscopy instrument, *Appl. Opt.*, OSA - The Optical Society, 2012, pp. B130–B142.
144. Zhu, X.; Xu, T.; Lin, Q.; Liang, L.; Niu, G.; Lai, H.; Xu, M.; Wang, X.; Li, H. and Duan, Y., Advanced statistical analysis of laser-induced breakdown spectroscopy data to discriminate sedimentary rocks based on Czerny-Turner and Echelle spectrometers, *Spectrochim. Acta - Part B At. Spectrosc.*, **2014**, *93*, 8–13.
145. Hark, R. R.; Remus, J. J.; East, L. J.; Harmon, R. S.; Wise, M. A.; Tansi, B. M.; Shughrue, K. M.; Dunsin, K. S. and Liu, C., Geographical analysis of 'conflict minerals' utilizing laser-induced breakdown spectroscopy, *Spectrochim. Acta - Part B At. Spectrosc.*, **2012**, *74–75*, 131–136.
146. Müller, S.; Meima, J. A. and Rammlmair, D., Detecting REE-rich areas in heterogeneous drill cores from Storkwitz using LIBS and a combination of k-means clustering and spatial raster analysis, *J. Geochemical Explor.*, **2021**, *221*, 106697.
147. Anderson, R. B.; Bell, J. F.; Wiens, R. C.; Morris, R. V. and Clegg, S. M., Clustering and training set selection methods for improving the accuracy of quantitative laser induced breakdown spectroscopy, *Spectrochim. Acta - Part B At. Spectrosc.*, **2012**, *70*, 24–32.
148. Sheng, L.; Zhang, T.; Niu, G.; Wang, K.; Tang, H.; Duan, Y. and Li, H., Classification of iron ores by laser-induced breakdown spectroscopy (LIBS) combined with random forest (RF), *J. Anal. At. Spectrom.*, **2015**, *30*, 453–458.
149. Bhatt, C. R.; Jain, J. C.; Goueguel, C. L.; McIntyre, D. L. and Singh, J. P., Determination of Rare Earth Elements in Geological Samples Using Laser-Induced Breakdown Spectroscopy (LIBS), *Appl. Spectrosc.*, **2018**, *72*, 114–121.
150. Abedin, K. M.; Haider, A. F. M. Y.; Rony, M. A. and Khan, Z. H., Identification of multiple rare earths and associated elements in raw monazite sands by laser-induced breakdown spectroscopy, *Opt. Laser Technol.*, **2011**, *43*, 45–49.
151. Rossi, M.; Dell'Aglio, M.; De Giacomo, A.; Gaudiuso, R.; Senesi, G. S.; De Pascale, O.; Capitelli, F.; Nestola, F. and Ghiara, M. R., Multi-methodological investigation of kunzite, hiddenite, alexandrite, elbaite and

topaz, based on laser-induced breakdown spectroscopy and conventional analytical techniques for supporting mineralogical characterization, *Phys. Chem. Miner.*, **2014**, *41*, 127–140.
152. Verlaguet, A.; Brunet, F.; Goffé, B.; Menut, D.; Findling, N.; Poinssot, C. and Huet, B., Selective transfer of Li-Al-rich phyllosilicate to metamorphic veins (Western Alps): Laser Induced Breakdown Spectroscopy (LIBS) compositional profiles and microstructural characterization, *J. Geodyn.*, **2016**, *101*, 51–72.
153. Jolliffe, I. T., *Principal Component Analysis*, Springer Science & Business Media, New York, 1986.
154. Nascimento, J. M. P. and Dias, J. M. B., Vertex component analysis: A fast algorithm to unmix hyperspectral data, *IEEE Trans. Geosci. Remote Sens.*, **2005**, *43*, 898–910.
155. Wu, J., *Advances in K-means Clustering*, Springer Berlin Heidelberg, Berlin, Heidelberg, 2012.
156. Maulik, U.; Bandyopadhyay, S. and Mukhopadhyay, A., *Multiobjective Genetic Algorithms for Clustering: Applications in Data Mining and Bioinformatics*, Springer Science & Business Media, Berlin Heidelberg, 2011.
157. Maruyama, Y.; Blacksberg, J. and Charbon, E., A 1024× 8, 700-ps Time-gated SPAD Line Sensor for Planetary Surface Exploration with Laser Raman Spectroscopy and LIBS, *IEEE J. Solid-State Circuits*, **2014**, *49*, 179–189.
158. Williams, Q. and Knittle, E., Infrared and raman spectra of Ca5(PO4)3F2-fluorapatite at high pressures: Compression-induced changes in phosphate site and Davydov splittings, *J. Phys. Chem. Solids*, **1996**, *57*, 417–422.
159. Penel, G.; Leroy, G.; Rey, C.; Sombret, B.; Huvenne, J. P. and Bres, E., Infrared and Raman microspectrometry study of fluor-fluor-hydroxy and hydroxy-apatite powders, *J. Mater. Sci. Mater. Med.*, **1997**, *8*, 271–276.
160. Burke, E. A. J., The end of CNMMN and CCM—LONG LIVE THE CNMNC!, *Elements*, **2006**, *2*, 388.

ORIGINAL PAPERS

I

SINGULAR VALUE DECOMPOSITION APPROACH TO THE YTTRIUM OCCURRENCE IN MINERAL MAPS OF RARE EARTH ELEMENT ORES USING LASER-INDUCED BREAKDOWN SPECTROSCOPY

by

Sari Romppanen, Heikki Häkkänen & Saara Kaski, 2017

Spectrochimica Acta Part B: Atomic Spectroscopy, 2017, 134, 69–74

DOI: 10.1016/j.sab.2017.06.002

Spectrochimica Acta Part B 134 (2017) 69–74

Contents lists available at ScienceDirect

Spectrochimica Acta Part B

journal homepage: www.elsevier.com/locate/sab

Singular value decomposition approach to the yttrium occurrence in mineral maps of rare earth element ores using laser-induced breakdown spectroscopy☆

Sari Romppanen [a], Heikki Häkkänen [b], Saara Kaski [a,*]

[a] Department of Chemistry, University of Jyväskylä, P.O. BOX 35, FI-40014, Finland
[b] Dept. of Biological and Environmental Science, University of Jyväskylä, P.O. BOX 35, FI-40014, Finland

ARTICLE INFO

Article history:
Received 28 February 2017
Received in revised form 15 May 2017
Accepted 3 June 2017
Available online 4 June 2017

Keywords:
Yttrium
Laser-induced Breakdown Spectroscopy (LIBS)
Singular value decomposition
Mineral mapping
Rock analysis

ABSTRACT

Laser-induced breakdown spectroscopy (LIBS) has been used in analysis of rare earth element (REE) ores from the geological formation of Norra Kärr Alkaline Complex in southern Sweden. Yttrium has been detected in eudialyte ($Na_{15}Ca_6(Fe,Mn)_3Zr_3Si(Si_{25}O_{73})(O,OH,H_2O)_3(OH,Cl)_2$) and catapleiite ($Ca/Na_2ZrSi_3O_9\cdot 2H_2O$). Singular value decomposition (SVD) has been employed in classification of the minerals in the rock samples and maps representing the mineralogy in the sampled area have been constructed. Based on the SVD classification the percentage of the yttrium-bearing ore minerals can be calculated even in fine-grained rock samples.

1. Introduction

Yttrium belongs to the group of rare earth metals, REMs (also known as rare earth elements; REEs) with scandium and lanthanoids [1]. European commission has classified rare earth elements as critical material for EU due to high supply risk as well as economic importance [2]. Recently the EU Commission has divided REEs in to two groups, heavy rare earth elements (HREEs) and light rare earth elements (LREEs) and scandium. Yttrium belongs to HREEs and their demand has been predicted to increase in the future, which could lead to possible deficit in 2020. The importance on REEs for modern technology is caused by their specific optical, electrical and magnetic properties [3]. Yttrium is mainly used as raw material in ceramics, metallurgy, and phosphors. A well-known example is an yttrium-aluminum-garnet crystal used in Nd:YAG lasers. In many of these applications, yttrium is hard to substitute with another material without losing the functionality. In year 2016 yttrium oxide was consumed 3000 to 6000 tons globally, mostly to form very pure oxide compounds for luminescent phosphors. World production of yttrium was estimated to be 5000–7000 tons. Currently yttrium, along with other REEs, is mainly supplied in China [4]. Worldwide resources are supposed to be large, because yttrium occurs in most of the REE deposits [5,6]. In geological environments, yttrium can be found in many different minerals in various concentrations.

In this research, laser-induced breakdown spectroscopy (LIBS) has been utilized to mapping of yttrium-bearing rocks. For mining purposes, ore bodies are 3D-modelled based on different geological measurements and various analyzed samples. We have constructed mineral maps, which offer fast and informative description of the mineralogical and elemental distribution of the drill core samples. Many tasks in mining processes as well as in mill processes could also gain profit of this kind of specification of rocks. For example, the texture i.e. the grain size and the shape of the minerals and the location of the gangue minerals can complicate the beneficiation of the ore.

The applications of LIBS in analysis of various geological materials have been reviewed in detail by Harmon et al. [7] and the strongest evidence of the capability of LIBS is the still continuous operation of the ChemCam analyzer in planetary exploration in Mars [8]. The first reported LIBS research on yttrium by Ishizuka [9] thoroughly studied the plasma dimensions, emission intensities and the calibration curves of several REEs in different salt matrices. As a result, lowest limit of detection for yttrium was 2 ppm and it was observed in sodium chloride matrix. Harilal et al. [10] used LIBS on yttrium to analyze temporal and spatial changes in a laser-induced plasma generated on a superconductor $YBa_2Cu_3O_7$ and Buckley et al. [11] detected yttrium in the exhaust fumes. Yttrium solutions, among others, have been used to compare LIBS and inductively coupled plasma spectroscopy (ICP-OES) by Fichet et al. [12] and a detection limit of 0.8 mg/L was obtained. Extensive

☆ Selected paper from the 9th International Conference on Laser-Induced Breakdown Spectroscopy (LIBS), Chamonix-Mont-Blanc, France, September 12 – September 16 2016.

* Corresponding author.
E-mail address: saara.kaski@jyu.fi (S. Kaski).

http://dx.doi.org/10.1016/j.sab.2017.06.002
0584-8547/

list of emission lines based on the REE samples prepared from reference materials at mass percentages of 1 to 50 has been provided by Martin et al. [13]. Just recently, Labutin et al. [14] have been able to determine limit of detection for yttrium, 0.6 ppm, using certified geological reference materials and plasma modeling.

Instead of quantitative analysis of yttrium, the aim of this research was identification of the yttrium-bearing minerals using singular value decomposition (SVD). It offers a possibility to find structure between the observations and the data variables, which can be used to extract the most important information to represent the data.

2. Experimental

2.1. Samples

The three diamond drill core samples from Norra Kärr deposit were selected for the LIBS analysis. The geological formation of Norra Kärr Alkaline Complex in southern Sweden consists on agpaitic nepheline syenites, also called as grennaite, which is a rock type rich in zirconium and rare-earth elements. The samples consist of typical PGT grennaite (grennaite with pegmatite), in which fine-grained greenish aegirine-rich ground mass contains leucosomic coarser pegmatitic sections, where mineral composition is nepheline altered to zeolite (natrolite–analcime), microcline, albite, eudialyte and catapleiite [15,16]. This PGT-type of mineralization covers about 75% of Norra Kärr's mineral resource. The main minerals of these PGT-rocks and examples of their chemical formulas are presented in Table 1. In minerals, the ratio of the cations may vary and partly they may have been substituted by other similar-sized elements even inside a single crystal. Thus, the chemical formulas given are in general form. The potential ore minerals of Norra Kärr are eudialyte and catapleiite, whereas the aegirine, all the feldspars and the feldspathoid nepheline are unworthy gangue minerals.

In general, REE grades in eudialyte may be lower than those of other REE-minerals monazite and xenotime, but in eudialyte, the HREE content is high and the environmentally hazardous uranium and thorium contents are lower [5]. Especially in Norra Kärr deposit the proportion of the valuable HREEs, including yttrium, is high. It has been investigated, that the eudialyte minerals contain as high as 95% of REEs of Norra Kärr. Also, economically interesting zirconosilicate mineral, catapleiite, occurs in the deposit. The total REE and zirconium contents as oxides in specific coarse-grained PGT have been analyzed at concentrations of 0.62% and 2.01%, respectively [15]. On average the yttrium content in Norra Kärr eudialyte is 1.3% [17]. This indicates, that some cations of eudialyte have been substituted by yttrium and due to the chemical similarity, by other HREEs.

2.2. Setup

Plasma was generated by focusing a KrF excimer laser (Optex, Lambda Physik) into the surface of a sample at spot size of 200 μm in diameter. Average pulse energy of ~2.5 mJ corresponds to irradiance of approximately 0.9 GW/cm^2. The plasma emission was collected via fused silica fiber. Fiber head was fixed to 30° angle from the laser beam and the distance from the plasma plume was 1 cm. Plasma light was dispersed in a 150 mm Czerny-Turner type imaging spectrograph (Acton, SP-150), resolution was 0.2 nm.

An intensified charge coupled device (ICCD) with a 1024 × 256 pixel imaging area and an 18-mm intensifier (InstaSpec V, Oriel) was used in recording the spectra. The delay time of 1 μs and the gate width of 2 μs were found optimal for these measurements and were controlled by a delay generator (model DG 535, Stanford Research System, Inc.). From all three samples a 1.5 cm × 1.5 cm area was measured resulting in with 60 × 60 spectra. At each location 5 laser shots were accumulated to produce a LIBS spectrum.

2.3. Data processing

The spectral data was decomposed with SVD using MATLAB R2015a software (The MathWorks, Inc.) from the original raw data (except for the background correction in the detector). The spectra were arranged to a matrix containing 60 × 180 measurements and each consisted of 701 pixels, which corresponded to the image intensified area of the 1024 pixel detector representing the spectral region of 389 nm – 417 nm.

3. Results and discussions

The mathematical formulation in detail of the singular value decomposition can be found elsewhere [18–20], but the schematic diagram in Fig. 1 demonstrates the variables in this research given by SVD function [21]. U and V are orthogonal normalized matrices and the columns of U and V are called left and right singular vectors, respectively. S is a diagonal matrix containing the singular values, which are positive and sorted in the decreasing order.

SVD is related to the principal component analysis (PCA). If the spectral data in A is centered column wise as it typically is in PCA, the results are equal: right singular vectors given as columns of the matrix V correspond to the principal components, also known as loadings, and the matrix U*S contains the scores of PCA [20]. The feasibility of PCA on LIBS spectra in constructing of high-resolution maps has been recently demonstrated by Klus et al. [22], which based on the idea that the first principal component represents the variation caused solely by the uranium and its score values show the location of the ore.

In our approach the matrices obtained via SVD are used directly for the classification of the spectral data. Firstly, the spectral data matrix has not been pre-processed. The discussion of the influence of the LIBS data treatment, including data centering, to the multivariate data analysis can be found in detail elsewhere [23], but in this case the raw data is optimal to find the differences in several minerals. When the data is not centered, the first component spectrum typically represents approximate average spectrum and the others show changes respective

Table 1
Main minerals of PGT-type grennaite in Norra Kärr deposit.

Mineral	Typical chemical formula	*wt%* [15]
Aegirine	$NaFeSi_2O_6$	21.4
Nepheline	$(Na,K)AlSiO_4$	11.2
Natrolite - Analcime	$Na_2Al_2Si_3O_{10}\cdot 2H_2O$ - $NaAlSi_2O_6\cdot H_2O$	16.3
Microcline	$KAlSi_3O_8$	16.0
Albite	$NaAlSi_3O_8$	17.7
Anorthoclase	$(Na,K)AlSi_3O_8$	1.3
Eudialyte	$Na_{15}\,Ca_6(Fe,Mn)_3\,Zr_3Si(Si_{25}O_{73})(O,OH,H_2O)_3(OH,Cl)_2$	8.2
Catapleiite	$Ca/Na_2ZrSi_3O_9\cdot 2H_2O$	4.0

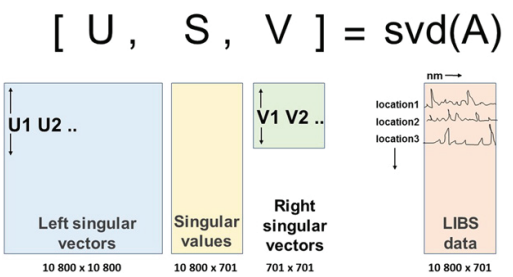

Fig. 1. Schematic diagram of the outcome of the singular value decomposition on the analyzed LIBS data.

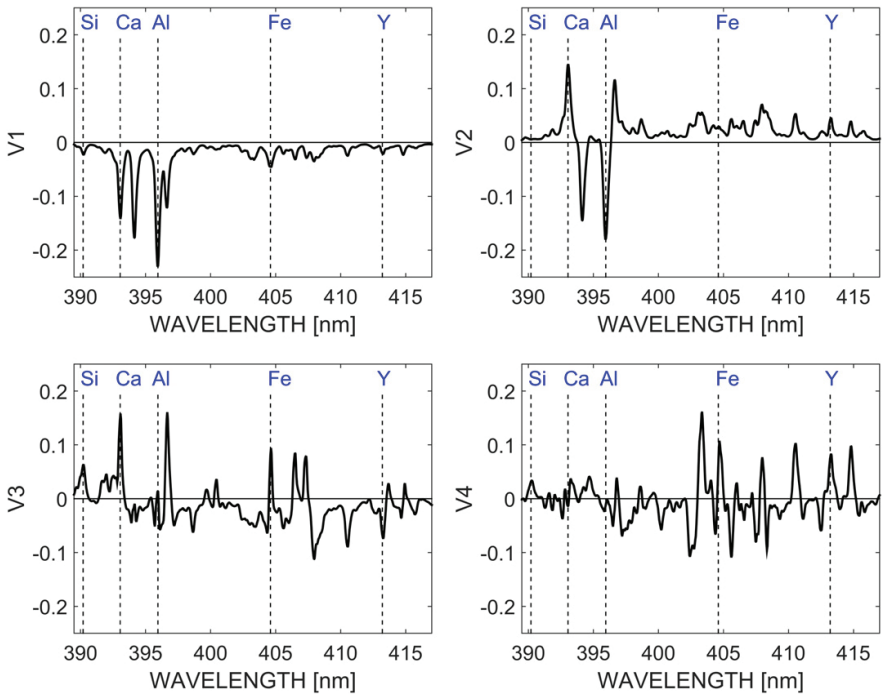

Fig. 2. Right singular vectors V1 – V4 calculated by SVD from the LIBS spectra measured from Norra Kärr drill core samples. Lines of the silicon, calcium, aluminum, iron and yttrium are presented in x-axis to show the contribution of selected elements to the components.

to it [24]. The SVD components V1 – V4, which explain 99.5% of the variance of the LIBS data (calculated from S^2), are presented in Fig. 2. If the value of V is close to zero at certain wavelength it has only a little contribution to the component. A high positive or negative load, on the other hand, suggests a strong contribution of the wavelength to the component in question [25]. Some selected wavelengths of representative elements describing the sample minerals have been marked to the spectrum in Fig. 2 to guide the eye. As the analysis is based on the whole spectrum in the range of 389 nm – 417 nm, the laborious identification of spectral lines with dense, overlapping spectra of zirconium, iron and yttrium is not needed. With strong negative peaks, V1 correlates to the existence of aluminum and calcium. V2 has a strong positive peak of calcium and also smaller peaks for yttrium and iron, whereas the aluminum peak is negative. V3 correlates to silicon and iron on positive peaks and to yttrium on negative peaks. V4 shows positive peaks of iron and yttrium, whereas others are negligible.

The matrix U works as a scaled version of the PCA scores [18] and the maps in Fig. 3 show values of the U in each measurement point with respect to the first four SVD components. The values of U1 regarding to the first component V1 were all negative, but other three show both positive and negative values. Sign of the U value (Fig. 3) controls the appearance of the certain peaks in component spectra (Fig. 2) and the magnitude has an impact to the intensity.

The mineral composition of sample was classified according to sign of the singular vectors U2, U3 and U4. It was assumed, that the similar shaped spectra would tend to cluster in a particular region according to their geochemical composition. As the values of U1 were all negative and the corresponding component V1 had a form of negative average spectrum, it was excluded from this analysis. The values of U2, U3 and U4 were divided to 8 different regions described by the octant notation. For example, when the values were all positive, the octant region was marked as "+++" and as "−−−" when all three were negative.

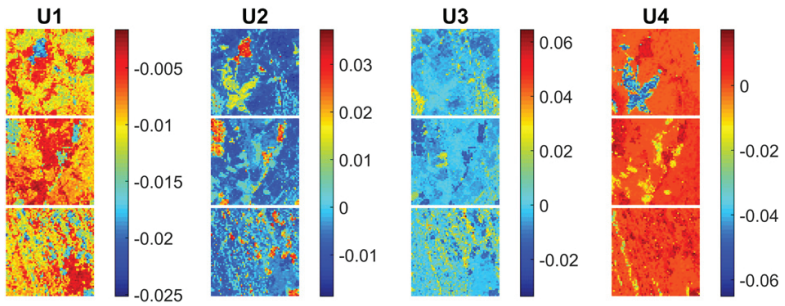

Fig. 3. Left singular vectors U1 – U4 for each measured location are presented as colored maps for three Norra Kärr samples. Note the different numerical scale on each plot.

All data points were classified to one of these octants and were presented in colors to provide maps of the samples, named A, B and C, in Fig. 4(1). As a reference, the photo, where the main minerals have been macroscopically identified in Fig. 4(2) is shown. It can be observed, that the map based on SVD classification follows the locations of the coarser grained areas. In photo taken under UV laser light (Fig. 4(3)) catapleiite can be recognized due to the strong green luminescence, which is typical to the Norra Kärr catapleiite and is caused by uranyl ion $(UO_2)^{2+}$. Other luminescence colors may also correlate to certain minerals, as luminescence often is an indication of presence of an activator element in the mineral structure [26]. In addition, the yttrium distribution determined as intensity from yttrium line at 412.8 nm [27] is presented in Fig. 4(4).

Based on the classification results, the original data was used to generate average spectra of all the measured locations belonging to specific color. The eight spectra are presented in Fig. 5, and final division to corresponding mineral types has been based on the strongest spectral features in them. Again, only some emission lines are marked to the spectrum to support the analysis.

The areas in the map under dark red, light red, blue and violet have been recognized as feldspar and feldspathoid minerals. Spectral lines of potassium can be seen as side wings in the both red spectra (insert in Fig. 5). The average contents (*wt%*) of potassium in Norra Kärr microcline and nepheline are 8.99% and 2.32%, respectively [28], so the light red areas in Fig. 4(4) most likely are microcline and dark red are feldspathoid nepheline. The black colored group belong to the aegirine, since iron and silicon contents are high in the average spectrum. The two green average spectra differ only slightly on their relative intensities, mostly of calcium. The respective locations in the map have been recognized in the areas, where the catapleiite mineral emits strong green luminescence in Fig. 4(3). The yellow areas correlate to the locations of reddish eudialyte mineral in the photos in Fig. 4(2). The intensities of yttrium, iron and manganese lines are strong in yellow spectrum and the lines are wide due to the occurrence of the zirconium, although not marked to the spectra. The comparison of green spectra of catapleiite to the other zirconium-rich mineral eudialyte and to the iron-rich aegirine is shown in another insert in Fig. 5. The green catapleiite spectra do not contain lines of manganese or iron, but otherwise follows the spectral lines of the yellow eudialyte, which is congruent to the mineral compositions in Table 1.

The correlation between the mineral locations and the areas classified by the SVD was very good as shown in Fig. 4. As a result, the content of the ore minerals eudialyte and catapleiite could be determined for the analyzed samples (Table 2). In the fine-grained areas of sample C, the macroscopic identification of minerals is very challenging, even impossible. The estimated percentage level of eudialyte (12% of the measured points) most likely would not have been obtained without the SVD classification based on the LIBS analysis. For these kinds of samples the complementary laser spectroscopic method Raman, which in general is very powerful in mineral identification, suffers from the strong fluorescent background.

SVD classification could be carried out to any LIBS spectra measured, but the spectral range, which optimally describes the changes in the minerals of interest, must be selected with care. When aiming to the potential use in on-line sorting, the use of high resolution spectrum at wide spectral range quickly increases the data handling time and thus

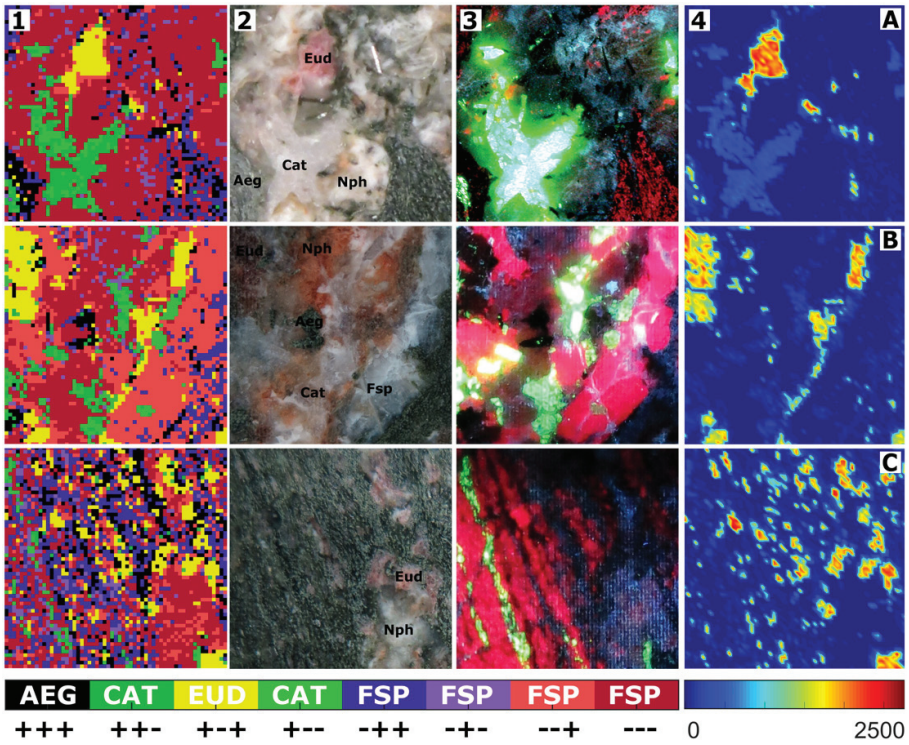

Fig. 4. (1) Mineral classification, based on the singular value decomposition using left singular vectors U2, U3 and U4, was carried out simultaneously for three Norra Kärr samples (A, B, C). Each color represents one octant, e.g. yellow areas correspond to the data points, where the values of U2 and U4 were positive and U3 negative (+−+). The results are compared to the (2) photo of the measured area. Mineral abbreviation Eud stands for eudialyte, Aeg for aegerine, Cat for catapleiite, Nph for nepheline and Fsp for feldspar minerals. In (3) corresponding luminescence photo under UV laser light (248 nm) is presented and in (4) distribution of yttrium emission intensity at 412.8 nm, where darkest blue corresponds negligible values.

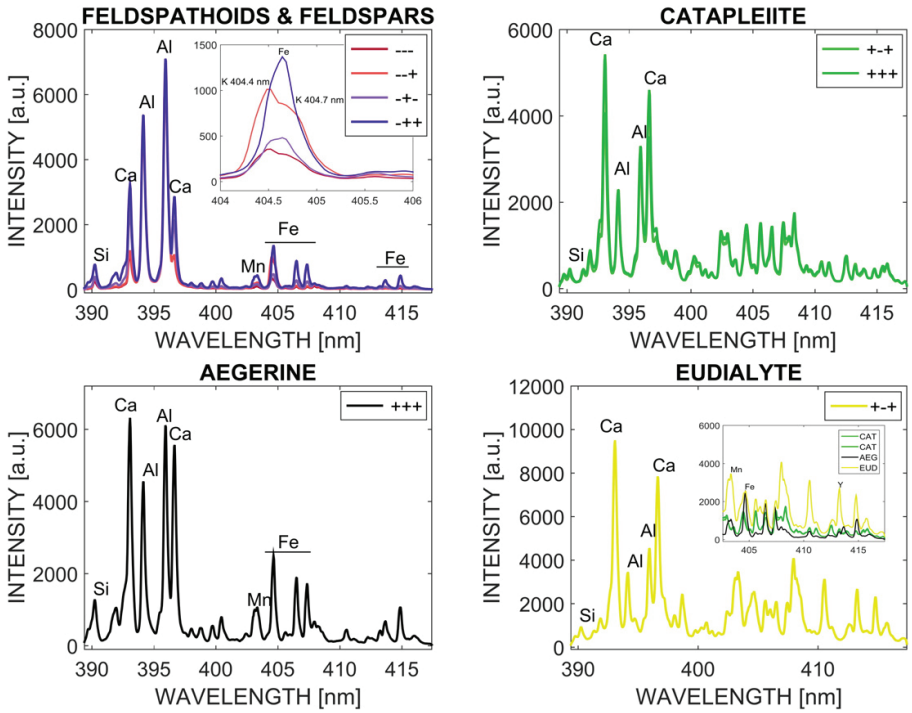

Fig. 5. Each color spectrum represent the average, which has been calculated from the original spectral data belonging to specific color shown in Fig. 4. Similar spectra are illustrated in the same subplot to demonstrate the respective resemblance. Small insert spectra show the differences in the spectral features of feldspar/feldspathoid minerals (up left) and eudialyte, catapleiites and aegerine (down right).

it is necessary to find a compromise. In this research, the spectra measured from 389 nm – 417 nm was optimally describing the Norra Kärr PGT samples. If more lines would have been included to the study, their contribution might have been dominating the first components and the separation would have needed more values of singular vectors U. On the other hand, without certain lines, the identification is more approximate. This was observed, when sorting was also tried separately for sample A in the spectral regions of 401 nm – 428 nm and 283 nm – 317 nm. In general, the first case lacks lines of silicon and aluminum, but shows yttrium, zirconium, iron and calcium. An oversimplified conclusion of this test was that map generated at this range describes best the eudialyte and catapleiite minerals and the gangue minerals are not separated well enough. The latter spectral range shows strong lines of silicon, aluminum, and calcium and, respectively, classifies better the gangue minerals but does not see difference between catapleiite and eudialyte. By combining these spectral ranges similar classification to the one given in Fig. 4 can be obtained, which can be seen as a proof of the optimal performance obtained by spectra measured at 389 nm – 417 nm.

This classification describes only the major differences in the spectra, because the number of vectors is limited. If there are only few points in the data set for specific mineral of interest, it may not be included to the selected components. To demonstrate this, the classification was carried out also separately on each sample A, B and C at the optimal spectral range between 389 nm and 417 nm. As a result, the catapleiite mineral was not found from the sample C. When the average spectra obtained from sample C were taken under study, it was realized, that method rather found differences in the intensities of the main emission lines in the larger groups of data points instead of detecting the change in the relatively weaker yttrium lines of catapleiite. The percentage catapleiite in the sample C was only 4, corresponding to 144 measurement points. On the contrary, although the eudialyte content in sample A was same 4%, it was clearly seen at the sampled locations. This can be explained by the greater difference in the spectrum, as eudialyte has strong lines of yttrium, zirconium, and manganese in the range 404 nm (Fig. 5).

Table 2
Mineral percentages in three sampled areas based on the SVD classification of the LIBS spectra.

%	A	B	C
Eudialyte	4	12	12
Catapleiite	12	10	4
Gangue minerals	83	78	84

The appearance of calcium and aluminum in Fig. 5. despite the general chemical formula given in Table 1 can be either seen as an indicator of an occurrence of many minerals at the measured location or the occurred replacement of cations in the minerals. At the borders of mineral grains, the laser most likely hits simultaneously to two or even more different minerals and thus the obtained spectrum is a mixture of these. Also the chemical variations in minerals are common and the analysis based on SVD is not meant to be that exact to differentiate all of those. Thus, the average spectra may be somewhat misleading for the recognition of the minerals. Especially for the elements with weak intensities, it could be useful to check how much spectrum in measured location differs from an average one. For example, yttrium lines could be observed, in descending order of intensity, in the average spectra of eudialyte (yellow), catapleiite (greens) and aegirine (black) in Fig. 5. The map constructed of the intensity distribution of yttrium line in Fig. 4(4) reveals, that yttrium rarely occurs at the regions of aegirine in these samples.

4. Conclusions

An approach based on SVD on the LIBS spectra can be used extract the mineralogical information of rock samples. The classification of all spectral points based on the singular vectors can be used to construct a map representing the mineralogy and geological texture at the sampled area. The minerals can be identified based on the average spectra from the original data. There may be a possibility to detect also the chemical alterations of minerals, but care must be taken in the interpretation of the results and the use of the original data in addition to the average spectra is recommended. A prior knowledge of the minerals to be identified is a benefit in the selection of a representative spectral range, but the method can be used as a first approach to discriminate and visualize any spectral data.

Acknowledgements

This research is supported by the Academy of Finland (Grant 281955 to S.K. and Grant 282240 to H.H.). The Norra Kärr samples were kindly provided by Tasman Metals AB (currently Leading Edge Materials).

References

[1] N.G. Connelly, Nomenclature of inorganic chemistry: IUPAC recommendations 2005, The Red Book, Royal Society of Chemistry, Cambridge, 2005.
[2] E. Commission, Critical raw materials for the EU, Report of the Ad-hoc Working Group on Defining Critical Raw Materials, 53, 2010.
[3] European Commission, Report on critical raw materials for the EU, Report of the Ad hoc Working Group on Defining Critical Raw Materials, 41, 2014http://ec.europa.eu/enterprise/policies/raw-materials/files/docs/crm-report-on-critical-raw-materials_en.pdf.
[4] U.S. Geological Survey, Mineral Commodity Summaries, 2017http://dx.doi.org/10.3133/70180197.
[5] K.M. Goodenough, J. Schilling, E. Jonsson, P. Kalvig, N. Charles, J. Tuduri, E.A. Deady, M. Sadeghi, H. Schiellerup, A. Müller, G. Bertrand, N. Arvanitidis, D.G. Eliopoulos, R.A. Shaw, K. Thrane, N. Keulen, Europe's rare earth element resource potential: an overview of REE metallogenetic provinces and their geodynamic setting, Ore Geol. Rev. 72 (2016) 838–856, http://dx.doi.org/10.1016/j.oregeorev.2015.09.019.
[6] K.R. Long, B.S. Van Gosen, N.K. Foley, D. Cordier, The principal rare earth elements deposits of the United States — a summary of domestic deposits and a global perspective, US Geol. Surv. Sci. Investig. 89 (2010) 8, http://dx.doi.org/10.1007/978-90-481-8679-2_7.
[7] R.S. Harmon, R.E. Russo, R.R. Hark, Applications of laser-induced breakdown spectroscopy for geochemical and environmental analysis: a comprehensive review, Spectrochim. Acta - Part B At. Spectrosc. 87 (2013) 11–26, http://dx.doi.org/10.1016/j.sab.2013.05.017.
[8] R.C. Wiens, S. Maurice, B. Barraclough, M. Saccoccio, W.C. Barkley, J.F. Bell, S. Bender, J. Bernardin, D. Blaney, J. Blank, M. Bouye, N. Bridges, N. Bultman, P. Cais, R.C. Clanton, B. Clark, S. Clegg, A. Cousin, D. Cremers, A. Cros, L. Deflores, D. Delapp, R. Dingler, C. D'Uston, M. Darby Dyar, T. Elliott, D. Enemark, C. Fabre, M. Flores, O. Forni, O. Gasnault, T. Hale, C. Hays, K. Herkenhoff, E. Kan, L. Kirkland, D. Kouach, D. Landis, Y. Langevin, N. Lanza, F. Larocca, J. Lasue, J. Latino, D. Limonadi, C. Lindensmith, C. Little, N. Mangold, G. Manhes, P. Mauchien, C. McKay, E. Miller, J. Mooney, R.V. Morris, L. Morrison, T. Nelson, H. Newsom, A. Ollila, M. Ott, L. Pares, R. Perez, F. Poitrasson, C. Provost, J.W. Reiter, T. Roberts, F. Romero, V. Sautter, S. Salazar, J.J. Simmonds, R. Stiglich, S. Storms, N. Striebig, J.J. Thocaven, T. Trujillo, M. Ulibarri, D. Vaniman, N. Warner, R. Waterbury, R. Whitaker, J. Witt, B. Wong-Swanson, The ChemCam instrument suite on the Mars Science Laboratory (MSL) rover: body unit and combined system tests, Space Sci. Rev. 170 (2012) 167–227, http://dx.doi.org/10.1007/s11214-012-9902-4.
[9] T. Ishizuka, Laser Emission Spectrography of Rare Earth Elements, 504, 1967 8–11.
[10] S.S. Harilal, P. Radhakrishnan, V.P.N. Nampoori, C.P.G. Vallabhan, Temporal and spatial evolution of laser ablated plasma from $YBa_2Cu_3O_7$, Appl. Phys. Lett. 64 (1994) 3377–3379, http://dx.doi.org/10.1063/1.111280.
[11] S.G. Buckley, H.A. Johnsen, K.R. Hencken, A.D.W. Hahn, Implementation of laser-induced breakdown spectroscopy as a continuous emissions monitor for toxic metals, Waste Manag. 20 (2000) 455–462, http://dx.doi.org/10.1016/S0956-053X(00)00011-8.
[12] P. Fichet, M. Tabarant, B. Salle, C. Gautier, Comparisons between LIBS and ICP/OES, Anal. Bioanal. Chem. 385 (2006) 338–344, http://dx.doi.org/10.1007/s00216-006-0384-7.
[13] M. Martin, R.C. Martin, S. Allman, D. Brice, A. Wymore, N. Andre, Quantification of rare earth elements using laser-induced breakdown spectroscopy, Spectrochim. Acta - Part B At. Spectrosc. 114 (2015) 65–73, http://dx.doi.org/10.1016/j.sab.2015.10.005.
[14] T.A. Labutin, S.M. Zaytsev, A.M. Popov, N.B. Zorov, A novel approach to sensitivity evaluation of laser-induced breakdown spectroscopy for rare earth elements determination, J. Anal. At. Spectrom. 31 (2016) 2223–2226, http://dx.doi.org/10.1039/C6JA00200E.
[15] M. Saxon, M. Leijd, K. Forrester, J. Berg, Geology, mineralogy, and metallurgical processing of the Norra Kärr heavy REE deposit, Sweden, Symp. Strateg. Crit. Mater. Proceedings, Novemb. 13–14, 2015 2015, pp. 97–107.
[16] A.S.L. Sjöqvist, D.H. Cornell, T. Andersen, M. Erambert, M. Ek, M. Leijd, Three compositional varieties of rare-earth element ore: Eudialyte-group minerals from the Norra Kärr Alkaline Complex, Southern Sweden, Fortschr. Mineral. 3 (2013) 94–120, http://dx.doi.org/10.3390/min3010094.
[17] B. Castor, J.B. Hedrick, Rare earth elements, in: S.T. Kogel, Jessica Elzea, Nikhil C. Trivedi, James M. Barker, Krukowski (Eds.),Ind. Miner. Rocks, Society for Mining, Metallurgy and Exploration 2006, pp. 769–792, http://dx.doi.org/10.1007/978-3-642-35458-8.
[18] I.T. Jolliffe, Principal component analysis, second edition, Encycl. Stat. Behav. Sci. 30 (2002) 487, http://dx.doi.org/10.2307/1270093.
[19] H. Abdi, L.J. Williams, Principal component analysis, Wiley Interdiscip. Rev. Comput. Stat. 2 (2010) 433–459, http://dx.doi.org/10.1002/wics.101.
[20] M. Wall, A. Rechtsteiner, L.M. Rocha, Singular value decomposition and principal component analysis, in: D.P. Berrar, W. Dubitzky, M. Granow (Eds.),A Pract. Approach to Microarray Data Anal., Kluwer 2003, pp. 1–18, http://dx.doi.org/10.1007/0-306-47815-3_5.
[21] Matlab Documentation, MathWorks, Inc(n.d.) https://se.mathworks.com/help/matlab/ref/svd.html (accessed May 5, 2017).
[22] J. Klus, P. Mikysek, D. Prochazka, P. Pořízka, P. Prochazková, J. Novotný, T. Trojek, K. Novotný, M. Slobodník, J. Kaiser, Multivariate approach to the chemical mapping of uranium in sandstone-hosted uranium ores analyzed using double pulse Laser-Induced Breakdown Spectroscopy, Spectrochim. Acta - Part B At. Spectrosc. 123 (2016) 143–149, http://dx.doi.org/10.1016/j.sab.2016.08.014.
[23] P. Pořízka, J. Klus, A. Hrdlička, J. Vrábel, P. Škarková, D. Prochazka, J. Novotný, K. Novotný, J. Kaiser, Impact of Laser-Induced Breakdown Spectroscopy data normalization on multivariate classification accuracy, J. Anal. At. Spectrom. (2016) 277–288, http://dx.doi.org/10.1039/C6JA00322B.
[24] I.R. Lewis, H. Edwards, Handbook of Raman Spectroscopy: From the Research Laboratory to the Process Line, CRC Press, 2001.
[25] M.H. Trauth, MATLAB Recipes for Earth Sciences, 2nd edition Springer-Verlag, Berlin Heidelberg, 2007http://dx.doi.org/10.1007/978-3-540-72749-1.
[26] M. Gaft, R. Reisfeld, G. Panczer, Modern Luminescence Spectroscopy of Minerals and Materials, 1st ed. Springer-Verlag, Berlin Heidelberg, 2005.
[27] A. Kramida, Yu Ralchenko, J. Reader, NIST Atomic Spectra Database (ver. 5.3) [Online], Natl. Inst. Stand. Technol. Gaithersburg, MD, 2015.
[28] O.J. Adamson, The Petrology of the Norra Kärr District. An occurrence of alkaline Rocks in Southern Sweden, Geol. Föreningen I Stock. Förhandlingar, 66, 1944 112–255.

II

OPTIMIZATION OF SPODUMENE IDENTIFICATION BY STATISTICAL APPROACH FOR LASER-INDUCED BREAKDOWN SPECTROSCOPY DATA OF LITHIUM-PEGMATITES

by

Sari Romppanen, Ilkka Pölönen, Heikki Häkkänen, & Saara Kaski, 2021

Manuscript, 2021

Request a copy from the author.

III

TIME-GATED RAMAN AND LASER-INDUCED BREAKDOWN SPECTROSCOPY IN MAPPING OF EUDIALYTE AND CATAPLEIITE

by

Sari Romppanen, Heikki Häkkänen, Jere Kekkonen, Jan Nissinen, Ilkka Nissinen, Juha Kostamovaara & Saara Kaski, 2019

Journal of Raman Spectroscopy

DOI: 10.1002/jrs.5622

Sharing link

IV

LASER-INDUCED TIME-RESOLVED LUMINESCENCE IN ANALYSIS OF RARE EARTH ELEMENTS IN APATITE AND CALCITE

by

Sari Romppanen, Heikki Häkkänen & Saara Kaski, 2021

Journal of Luminescence

DOI: 10.1016/j.jlumin.2021.117929

Journal of Luminescence 233 (2021) 117929

Contents lists available at ScienceDirect

Journal of Luminescence

journal homepage: http://www.elsevier.com/locate/jlumin

Laser-induced time-resolved luminescence in analysis of rare earth elements in apatite and calcite

Sari Romppanen [a,*], Heikki Häkkänen [b], Saara Kaski [a]

[a] Department of Chemistry, University of Jyväskylä, P.O. Box 35, FI-40014, Finland
[b] Department of Biological and Environmental Science, University of Jyväskylä, P.O. Box 35, FI-40014, Finland

ARTICLE INFO

Keywords:
Time-resolved spectroscopy
Apatite
Minerals
Calcite
Laser-induced luminescence
Rare earth elements

ABSTRACT

Laser-induced time-resolved luminescence was used to study rare earth element (REE) containing natural apatite and calcite minerals. The luminescence from 400 nm to 700 nm in the minerals was analyzed with excitation ranges 210–340 nm and 405–535 nm. As an outcome, several useful excitation wavelengths to detect one or more REE from apatite and calcite are reported. The feasibility of selected excitations in *e.g.* avoiding the disturbance of intense Mn^{2+} luminescence band, results was demonstrated with a non-gated detector.

1. Introduction

Rare earth elements (REEs) are representing a group of elements consisting of lanthanoids (La–Lu), yttrium (Y), and scandium (Sc). REEs are needed for modern technology [1] and a rapid analysis technique would be a benefit at many stages of their supply chain. REEs can act as luminescence centres in host minerals and therefore luminescence spectroscopy is efficient in detecting them. Natural minerals typically host several REEs simultaneously [2]. Although luminescence emission of REEs is generally observed as relatively sharp lines and only some ions *e.g.* Ce^{3+} and Eu^{2+} have broad bands [3], in natural minerals, the luminescence spectrum can be rather complex with several overlapping bands. For example, the crystal field of the host mineral lattice can split the energy levels of REE^{3+} ions [3] and as a consequence, more luminescence emission lines may appear. In addition, the intensity of luminescence emission is dependent on both the mineral's crystallinity and on the surroundings of the luminescence centre, which may change the energy transfer, quenching, reabsorption and sensitizing processes [4–6].

Although one of the most common techniques to luminescent mineral research is cathodoluminescence [7–11], laser-induced time-resolved luminescence spectroscopy has several benefits, *e.g.* high laser power excites also weak luminescence centres, time-resolving enables separation of different luminescence centres from each other and the method could be easily combined with other laser-spectroscopic method like Raman spectroscopy or laser-induced breakdown spectroscopy (LIBS), as reviewed in the literature [4,6,12–14]. However, the occurrence of luminescence is strongly dependent on the selection of the laser wavelength used for the excitation. Therefore, the aim of this research was to survey, which excitation wavelengths would be optimal for detecting luminescence of certain or multiple REEs. A tunable ns-pulse laser was used at excitation regions 210–340 nm and 405–535 nm to study luminescent minerals, apatite and calcite, from the same geological site. The emission was detected in the visible range, with a view to the possible *on-line* and *on-site* applications in the future. Based on the results, suggestions for optimal excitations for the detection of REEs were produced and the concept was tested using the laser with a basic non-gated spectrometer.

2. Materials & methods

Two natural mineral samples, apatite and calcite, were chosen from the Siilinjärvi ultramafic alkaline-carbonatite complex in Eastern Central Finland. At the Siilinjärvi complex REE-hosting minerals are occurring in the "glimmerite" (phlogopite rock) and carbonatite rock types [15,16]. REEs are known to be situated in Ca-bearing phases in carbonatites like carbonates and apatites and in previous research overall REE content is analyzed to be smaller in calcite (509 ppm in Mg-rich calcite in apatite sövite *i.e* carbonatite proper) than in apatite (2986 ppm in glimmerite and 3820 ppm in apatite sövite) [17]. The results enable the general assumption of the occurrence of the same REEs in the host lattice of the chosen samples. At the moment, apatite is

* Corresponding author.
E-mail address: sari.m.romppanen@jyu.fi (S. Romppanen).

https://doi.org/10.1016/j.jlumin.2021.117929
Received 10 June 2020; Received in revised form 15 January 2021; Accepted 18 January 2021
Available online 29 January 2021

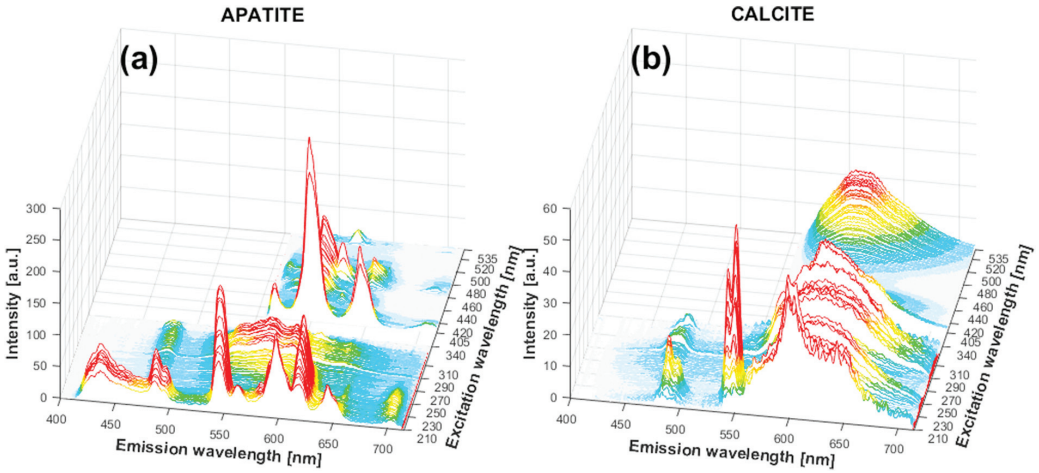

Fig. 1. Luminescence emission-excitation maps (EEMs) from apatite (a) and calcite (b), using excitations at UV (210–340 nm) and Vis (405–535 nm) with a step of 1 nm. The delay time was 50 μs and the gate 500 μs.

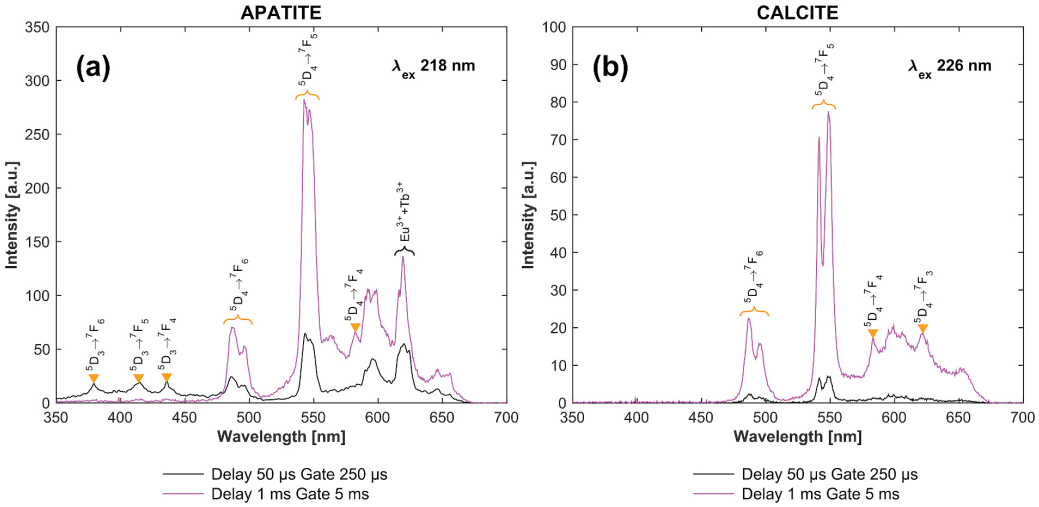

Fig. 2. The strongest luminescence peaks from Tb^{3+} (marked with orange triangles) can be observed at the laser excitation of 218 nm for apatite (a) and of 226 nm for calcite (b), measured at two different delay and gate times. Unmarked luminescence peaks are caused by Sm^{3+} and Eu^{3+}.

Table 1
Transitions and luminescence peaks of Tb^{3+} observed in apatite and calcite.

TRANSITION	APATITE [nm]	CALCITE [nm]
$^5D_3 \rightarrow {}^7F_6$	379	–
$^5D_3 \rightarrow {}^7F_5$	415	–
$^5D_3 \rightarrow {}^7F_4$	436	–
$^5D_4 \rightarrow {}^7F_6$	486/496	487/496
$^5D_4 \rightarrow {}^7F_5$	542	541/549
$^5D_4 \rightarrow {}^7F_4$	582	583
$^5D_4 \rightarrow {}^7F_3$	–	622

only exploited as a phosphate source [15]. Greenish apatite with a length about 2 cm representing medium-grained carbonate glimmerite and a 2 cm piece of reddish calcite were selected because they contained rather large areas of the same mineral macroscopically. Under a 254 nm ultraviolet (UV) lamp, both showed intense luminescence, especially calcite had a very strong red colour. The samples were sawed and polished.

Apatite often acts as a host to luminescent ions [18–21] and for example, manganese and REEs, can replace calcium in the mineral lattice. As the majority of apatite in Siilinjärvi complex is fluorapatite $Ca_5(PO_4)_3F$ [16], it is assumed that our sample is this phosphate mineral, having a hexagonal structure ($P6_3/m$) [22,23]. There are two Ca sites in the apatite's crystal structure: Ca (I) and Ca (II), which differ in both size and site-symmetry [9,18,22–24]. It is presented, how LREEs (light REEs: La–Sm) prefer the Ca (II) site in apatite's structure [25–28]. However, the REE content in apatite typically corresponds to the whole-rock composition, due to the poor REE selectivity [26,27,29]. Calcite's ($CaCO_3$) structure consists of planar carbonate $(CO_3)^{2-}$ groups within the centre of an equilateral oxygen triangle occupied by a carbon ion [18]. Rare earth elements can substitute Ca in calcite lattice and become luminescence centres, e.g. Refs. [4,6,12,30–34]. Also different divalent

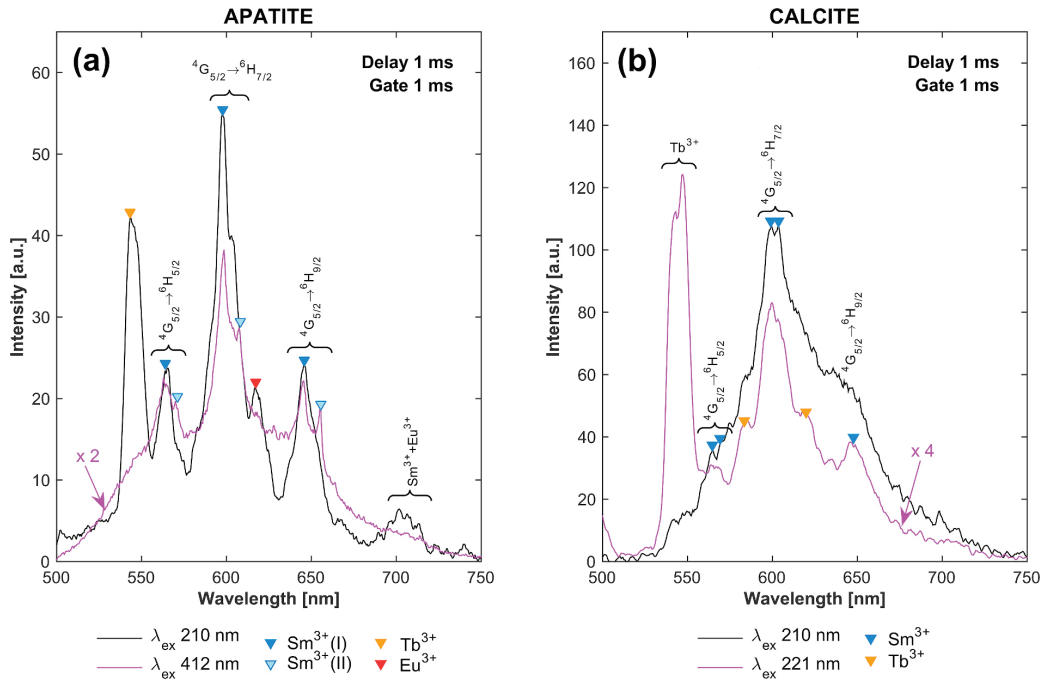

Fig. 3. In apatite (a) Sm^{3+} luminescence is observed only from substitution at Ca (I) site (dark blue triangles) or also from Ca (II) site (light blue triangles), depending on the excitation wavelength, here 210 nm (black) and 412 nm (violet), respectively. In calcite (b) the strongest Sm^{3+} signal is seen with excitation at 210 nm (black), but for other peaks of Sm^{3+}, the excitation at 221 nm (violet) is better. Note the scaling of the violet spectra in calcite. Peaks related to Tb^{3+} (orange triangles) and Eu^{3+} (red triangle) are also marked. All spectra were measured with a delay of 1 ms and a gate of 1 ms.

Table 2
Transitions and luminescence peaks of Sm^{3+} observed in apatite at two Ca sites and in calcite.

TRANSITION	APATITE: Ca (I) site [nm]	APATITE: Ca (II) site [nm]	CALCITE [nm]
$^4G_{5/2}\rightarrow{}^6H_{5/2}$	563	570	563/568
$^4G_{5/2}\rightarrow{}^6H_{7/2}$	598	607	599/604
$^4G_{5/2}\rightarrow{}^6H_{9/2}$	645	655	650
$^4G_{5/2}\rightarrow{}^6H_{11/2}$	705	–	–

cations can replace the Ca^{2+} cation, *e.g.* Mg^{2+}, Fe^{2+}, Mn^{2+} and Sr^{2+} [18].

Luminescence was measured with a home-built laser-induced time-resolved spectroscopy setup having a tunable laser wavelength system based on Ekspla OPO (optical parametric oscillator). The laser had a pulse duration of 3.3 ns and a repetition rate of 100 Hz. The signal was collected via a plano-convex lens with 45° geometry to the laser beam. The reflective collimator directed the light to fused silica fiber connected to the spectrograph. To block the laser light from the detector, a long-pass filter was used between the lens and reflective collimator. The selected filters had cut-on wavelengths at 266 nm, 400 nm, 450 nm, and 550 nm to match the excitation wavelengths between 210–340 nm and 405–535 nm. Each emission spectrum was accumulated from 400 laser pulses to average the influence of possible pulse-to-pulse laser energy fluctuations. All measurements were carried out at room temperature.

The light was directed to the Czerny-Turner type imaging spectrograph (Acton, SP-150) equipped with a grating having 300 grooves per mm (blazed to 500 nm, resolution >1 nm) and spectra were recorded with ICCD (Instaspec V, Oriel). The spectral range was about 350 nm and the central wavelength was changed by turning the grating. The calibration was carried out with HgAr lamp. A delay generator (model DG 535, Stanford Research System, Inc.) was used to control the time parameters of ICCD. To exclude the broad, strong, and very short-living luminescence emission bands of Ce^{3+} and Eu^{2+}, which are known to dominate steady-state luminescence spectra [6,35,36], a delay of 50 μs was used in the measurement of excitation-emission maps (EEMs) of calcite and apatite. The luminescence lifetimes (τ) of Ce^{3+} and Eu^{2+} bands are presented to be < 1 μs in literature, *e.g.* Ref. [6] and the chosen delay was proven also experimentally to be suitable for exclude these. Spectra were measured with a step of 1 nm (laser wavelength). Gate width was 500 μs to avoid the dominance of the long-living luminescence peaks. The benefit of the time-gated detection is presented on supplementary material (Fig. A1) with excitation wavelength of 266 nm. To further analyse the observed REE^{3+} emissions, certain wavelengths were re-measured with different delay times (10 μs, 50 μs, and 1 ms) with varying gate widths (25 μs, 250 μs, 1 ms, and 5 ms).

To test the predicted optimal excitation wavelength areas, the luminescence signal was directed to a non-gated Czerny-Turner type CCD spectrometer (Thorlabs, model CCS200, grating 600 lines/mm; blazed to 800 nm and FWHM spectral accuracy < 2 nm). The spectral range was 200–1000 nm, and the filters were applied to block the excitation laser light.

Data processing was carried out with MathWorks MATLAB R2015a program. As the laser energy varies in OPO as a function of wavelength, it was compensated for each spectrum by dividing the spectral intensities by the average energy value measured with Ophir (model PE10-SH-V2) laser power meter. All presented spectra have slight smoothing for enhanced visualization.

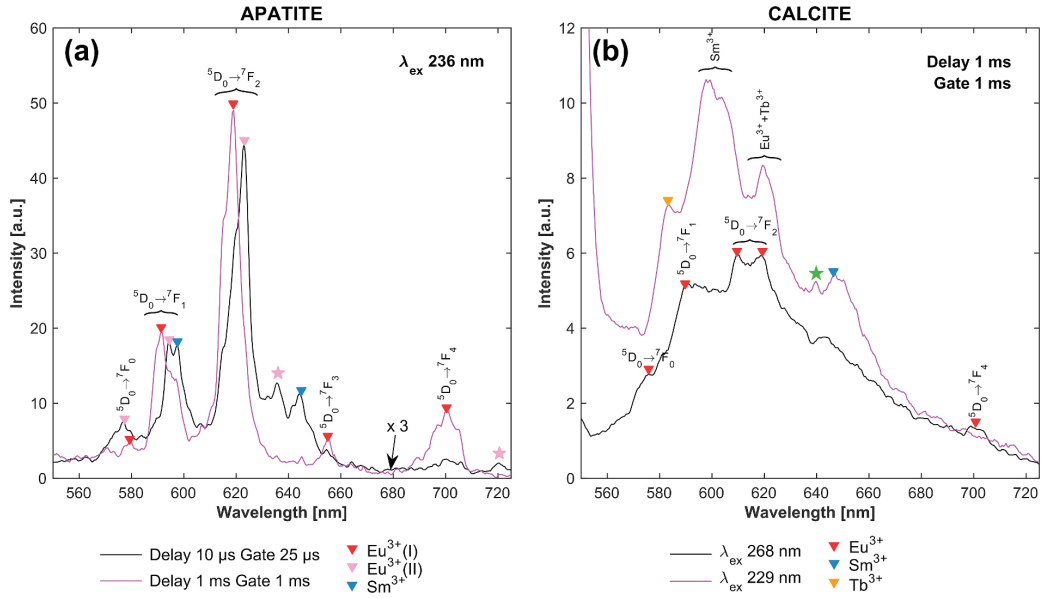

Fig. 4. In apatite (a) Eu^{3+} luminescence peaks from Ca (I) and Ca (II) sites can be observed with the same excitation wavelength of 236 nm by changing the delay time. Emission of Eu^{3+} in Ca (II) site can be seen with the shorter delay (10 µs, black) and emission of Eu^{3+} in Ca (I) site with the longer delay (1 ms, violet). In calcite (b) either the strong background caused by the Mn^{2+} band at excitation of 268 nm (black) or emission peaks from other REEs disturb the detection of Eu^{3+} luminescence (violet). Both spectra of calcite were measured with a delay of 1 ms and a gate of 1 ms. The peaks of Sm^{3+} (blue triangle) and Tb^{3+} (orange triangles) are marked in spectra and the peak with a green star in calcite is possibly related to Pr^{3+}.

Table 3
Eu^{3+} luminescence peaks recognized in apatite's Ca sites and in calcite, with respective transitions.

TRANSITION	APATITE: Ca (I) site [nm]	APATITE: Ca (II) site [nm]	CALCITE [nm]
$^5D_0 \rightarrow {}^7F_0$	579	573, 577	577
$^5D_0 \rightarrow {}^7F_1$	591	595	591
$^5D_0 \rightarrow {}^7F_2$	618	623	610/620
$^5D_0 \rightarrow {}^7F_3$	655	–	–
$^5D_0 \rightarrow {}^7F_4$	700	–	702

3. Results & discussion

3.1. Laser-induced time-resolved luminescence of apatite and calcite

Time-resolved luminescence spectra from apatite and calcite were measured at a range of 400–700 nm using excitations 210–340 nm and 405–535 nm. The delay time was 50 µs and the gate width 500 µs. Excitation-emission maps (EEMs) are shown in Fig. 1.

The chosen delay and gate times seem to be suitable for observing several narrow REE^{3+} luminescence peaks simultaneously. Shape of spectrum varies as the excitation wavelength changes. Intensities of the luminescence peaks and bands in calcite were lower than in apatite, which is most likely caused by the lower REE content in calcite in the Siilinjärvi [17].

In apatite (Fig. 1a) more REE^{3+} peaks can be observed than in calcite (Fig. 1b), where a broad luminescence band around 620 nm is dominating spectra at wide excitation regions. This band is caused by Mn^{2+} and is thoroughly studied, *e.g.* Refs. [8,30,37–43]. Also, the broad Mn^{2+} band is peaking at 573 nm in apatite (Fig. 1a) – note that the change in the emission wavelength is caused by different mineral structures [8]. In literature Mn^{2+} band in apatite in this spectral region has been observed earlier [21,44] and Mn^{2+} can accommodate both Ca (I) and Ca (II) sites in apatite's structure [4,19,45]. The absolute intensity of Mn^{2+} band in the measured excitation wavelength regions has no considerable difference between the apatite and calcite, even though the relative intensities of Mn^{2+} and REE^{3+} luminescence between the minerals differ (Fig. 1). Calcite from Siilinjärvi contains typically 0.10–0.32 wt % of MnO, whereas apatite has only 80–300 ppm of Mn [16]. In order to study how REEs contribute to the EEMs in Fig. 1, in the following selected excitation wavelengths are discussed in detail.

At excitation wavelength 218 nm, a strong double peak at 542 nm is observed in apatite (Fig. 2a) which is assigned as Tb^{3+} luminescence transition $^5D_4 \rightarrow {}^7F_5$ [4,7,12,46–60]. In calcite, this peak is detected at 541/549 nm and the strongest intensity is obtained at excitation wavelength 226 nm (Fig. 2b). The different mineral structures can explain the difference in both locations and relative intensities of this Tb^{3+} peak. Also, Tb^{3+} transitions $^5D_4 \rightarrow {}^7F_6$ and $^5D_4 \rightarrow {}^7F_4$ are seen in both minerals: at 486/496 nm and 582 nm in apatite (Fig. 2a) and 487/496 nm and 583 nm in calcite (Fig. 2b). In apatite also Tb^{3+} peaks at 379 nm, 415 nm and 436 nm can be detected, but only with measurement of delay 50 µs (Fig. 2a, black) and the respective transitions in the literature are $^5D_3 \rightarrow {}^7F_6$, $^5D_3 \rightarrow {}^7F_5$ and $^5D_3 \rightarrow {}^7F_4$ [4,7,36,48,52,57,59,60]. The different mineral lattice may cause the absence of these peaks in calcite, as the host material has been observed to influence the intensity of certain Tb^{3+}peaks [4,12]. Tb^{3+} has a transition of $^5D_4 \rightarrow {}^7F_3$, typically observed around ~620 nm, depending on the host material [46–49,55, 57–59]. In calcite, it is observed at 622 nm with the measurement delay of 1 ms (Fig. 2b, violet), but in apatite, there is a strong contribution from nearby Eu^{3+} peaks and the exact location of Tb^{3+} transition cannot be pointed. All clearly observed luminescence peaks of Tb in calcite and apatite and the respective transitions are collected into Table 1.

Several strong Sm^{3+} luminescence peaks can be seen in both minerals. In apatite Sm^{3+} can occupy Ca (I) and Ca (II) sites in the mineral structure [4,6,9,12,19,36,61,62]. For example, Sm^{3+} luminescence at excitation wavelength of 210 nm originates from the substitution to Ca (I) site (Fig. 3a, black). When excitation is changed to 412 nm (Fig. 3a,

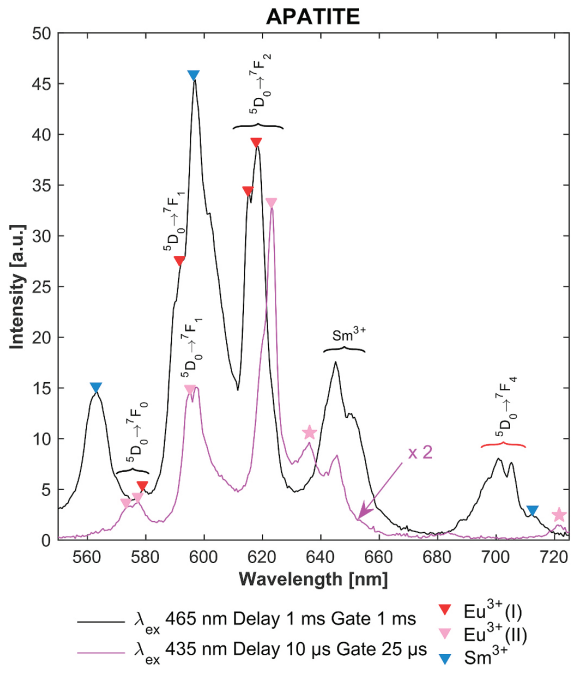

Fig. 5. Visible excitations can be used for detection of Eu^{3+} luminescence in apatite because the Mn^{2+} band is not detected in this excitation region. As an example, Eu^{3+} in Ca (I) site (red triangles) is better observed with excitation 465 nm (black) whereas Eu^{3+} in Ca (II) site (pink triangles) is seen with 435 nm excitation wavelength (violet). The measurement delay for observing luminescence from the sites is different, the longer 1 ms for Eu^{3+} in Ca (I) site, and the shorter 10 µs for Eu^{3+} in Ca (II) site. Note the scaling of the violet spectrum.

violet), also luminescence from Ca (II) site is detected. The band ~700 nm in apatite is a combination of Eu^{3+} and Sm^{3+} transition $^4G_{5/2} \rightarrow {}^6H_{11/2}$ (Fig. 3a, black).

In calcite the strongest Sm^{3+} luminescence was observed with excitation at 210 nm, but also a broad Mn^{2+} band occurs, nearly hindering the detection of other Sm^{3+} peaks than the double peak at 599/604 nm (Fig. 3b, black). At excitation 221 nm, also peaks at 563/568 nm and 650 nm can be detected clearly (Fig. 3b, violet). The occurrence of Sm^{3+} luminescence as two double peaks have also been reported for synthetic calcites [30,43,63,64]. Due to the strong luminescence of the overlapping Mn^{2+} band, the used visible excitations are not relevant for successful detection of Sm^{3+} in the measured calcite. All observed Sm^{3+} luminescence peaks are collected in Table 2 with the respective transitions recognized via literature [53,58,65–73].

Analogous to samarium, also luminescence of Eu^{3+} has been observed from different Ca sites in apatite, *e.g.* Refs. [9,19,36,74–86]. This is also the case in our study and as an example, spectra measured with excitation 236 nm are presented (Fig. 4a). The appearance of the luminescence from two Ca sites can be controlled by changing the delay time of the measurement. At the shorter delay of 10 µs, luminescence peaks of Eu^{3+} in Ca (II) site can be observed at 577 nm, 595 nm, and 623 nm (Fig. 4a, black). With the longer measurement having the delay of 1 ms, the luminescence from Eu^{3+} in Ca (I) site can be observed in 579 nm, 591 nm, 618 nm, 655 nm and 700 nm (Fig. 4a, violet). The peak ~620 nm is rather wide regardless of the occupied Ca site, which suggests further fine structure within this peak. It can be noted that we observe peaks at 636 nm and 720 nm in apatite (pink stars in Fig. 4a), always when also the peaks of Eu^{3+} from Ca (II) site are seen. Our assumption is, that both are luminescence of Eu^{3+} in Ca (II) site, somewhat supported by previous research, where the peak observed at ~636 nm was explained as a vibronic transition of Eu^{3+} in Ca (II) site [76,86].

In calcite, the detection of Eu^{3+} peaks is challenging due to the broad and strong Mn^{2+} band, as they are excited simultaneously. With excitation wavelength 268 nm, luminescence of Eu^{3+} is observed at 577 nm, 591 nm, 610 nm, 620 nm, 655 nm, and 702 nm although there is also Mn^{2+} band underneath (Fig. 4b, black). It can be remarked, that the transition $^5D_0 \rightarrow {}^7F_2$ here is observed as a double peak at 610/620 nm, also reported for doped calcite samples [43,63,87,88]. When luminescence from calcite is measured with excitation 229 nm, the contribution of Mn^{2+} is also relatively low and only the Eu^{3+} peak at 620 nm is seen along the adjacent Tb^{3+} peak (Fig. 4b, violet), whereas other Eu^{3+} peaks are not resolved. Table 3 summarizes the observed Eu^{3+} luminescence peaks in both minerals and the corresponding transitions were recognized based on *e.g.* Refs. [49,67,89–92].

We assume, that peak at 641 nm in calcite (Fig. 4b, green star) might be related to Pr^{3+}, which is observed around this spectral region [61,62,71,93–95]. Also, the suitability of deep UV excitation for Pr^{3+} in minerals has been proved very recently [96]. However, in the scope of this study, the occurrence of Pr^{3+} in our sample cannot be proven, because the other intensive Pr^{3+} peaks in this spectral region are located around 600 nm and most likely be overwhelmed by strong Sm^{3+} luminescence and by Mn^{2+} in calcite.

In the above, the occurrence of Eu^{3+} luminescence was only presented with UV excitation. In apatite, where the Mn^{2+} luminescence was not as strong as in calcite, the Eu^{3+} peaks can also be efficiently observed using also visible excitation. For example, excitation at ~465 nm is suitable for detecting Eu^{3+} in Ca (I) site whereas ~435 nm is good for Eu^{3+} in Ca (II) site (Fig. 5). The measurement times are analogous to our previous observations; the luminescence of Eu^{3+} from Ca (I) site is strong at the longer delay (1 ms) whereas from Ca (II) it is better observed at the shorter delay time (10 µs). In Fig. 5 those Eu^{3+} transitions, which have a strong contribution of nearby Sm^{3+} luminescence, are not marked. At excitation 435 nm there are two peaks related to transition $^5D_0 \rightarrow {}^7F_0$ at 573 nm and 577 nm (Fig. 5, violet). Therefore, it is assumed that in our sample Eu^{3+} is occupying at least three different Ca sites because europium's states $^5D_0$ and $^7F_0$ are non-degenerated [82]. It can be also remarked that the same peaks at 636 nm and 720 nm (Fig. 5, pink stars), which were seen in Fig. 4a along with the Eu^{3+} occurrence in Ca (II) site in apatite's structure are observed here as well.

The two strongest Dy^{3+} bands can be seen at ~480 nm and ~575 nm in both apatite and calcite *e.g.* with excitation 427 nm (Fig. 6). The corresponding transitions are $^4F_{9/2} \rightarrow {}^6H_{15/2}$ and $^4F_{9/2} \rightarrow {}^6H_{13/2}$ also reported previously for various dysprosium containing samples [69,73,90,97–100]. The recognized Dy^{3+} peaks are presented in Table 4. The peak at ~480 nm is wide and seems to consist of several peaks located very close together in both minerals. Such fine structure for the Dy^{3+} peak has been reported on apatite [61], in doped calcites [43,63] and other materials [7,100]. It seems that in apatite (Fig. 6a) the relative intensities of three peaks at 475 nm, 480 nm, and 484 nm vary when the measurement delay is changed from 10 µs to 1 ms, but such behaviour is not observed in calcite (Fig. 6b). We anticipate that this could be caused by the Dy^{3+} occupying different Ca sites in apatite, which would lead to the difference in relative intensities at changed delays, as demonstrated earlier for Eu^{3+}.

The Dy^{3+} band at ~575 nm is clearly observed with excitation 452 nm for apatite and 454 nm for calcite (Fig. 6, cyan). Also here is the fine structure of closely located peaks and similar patterns have been presented for Dy^{3+} at ~575 nm by others, *e.g.* Refs. [7,61,77]. With the excitation wavelength of 427 nm, the Dy^{3+} ~575 nm luminescence is strongly contributed by other luminescence species. In apatite adjacent Eu^{3+} (II) peak is dominating at the shorter measurement delay 10 µs (Fig. 6a, black). If the delay is changed to 1 ms, Dy^{3+} at 578 nm in apatite nm can be better resolved, but there is a background from the Mn^{2+}, Sm^{3+} (I), and Sm^{3+} (II) (Fig. 6a, violet). In calcite, the Dy^{3+} peak at 579 nm can be observed at the shorter delay only, as at the longer

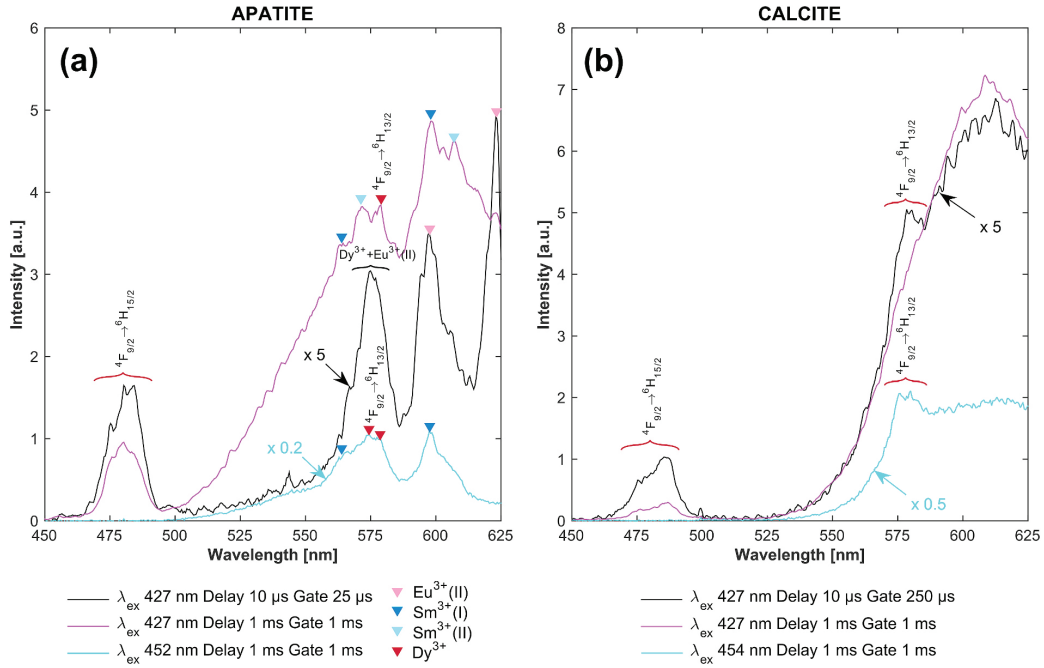

Fig. 6. Dy^{3+} luminescence peaks ~480 nm and ~575 nm in apatite (a) and calcite (b). The peak at 575 nm Dy^{3+} is observed clearly with excitation 452 nm (cyan), as laser wavelength 427 nm induces luminescence to the same spectral region also from other REEs and Mn^{2+}, which is demonstrated with measurement delays of 10 µs and as 1 ms (black & violet). Note the scaling of the black and the cyan spectra.

Table 4
Transitions and luminescence peaks of Dy^{3+} observed in apatite and calcite.

TRANSITION	APATITE [nm]	CALCITE [nm]
$^4F_{9/2} \rightarrow {}^6H_{15/2}$	475/480/484	485
$^4F_{9/2} \rightarrow {}^6H_{13/2}$	574/578	576/579

delays it is overwhelmed by intense Mn^{2+} band.

The right selection of the measurement time parameters with excitation 427 nm has importance in discovering the Dy^{3+} band at ~575 nm. In apatite, at the measurement of delay 10 µs, Dy^{3+} has a strong contribution of Eu^{3+} (II) peak (Fig. 6a, black). Measurement performed with the longer delay (1 ms), the Dy^{3+} at 578 nm in apatite nm can be better resolved (Fig. 6a, violet), but a strong contribution of Mn^{2+}, as well as Sm^{3+} (I) and Sm^{3+} (II), can be seen. In calcite (Fig. 6b), the detection of Dy^{3+} peak at 579 nm can be observed at the shorter delay

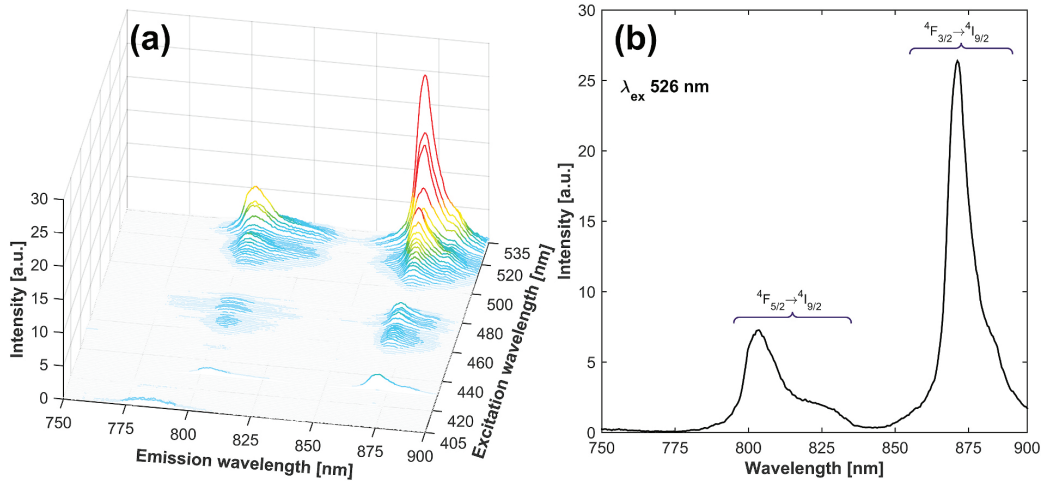

Fig. 7. Luminescence emission-excitation map from apatite (a) using excitations at 405–535 nm with a step of 1 nm. The Nd^{3+} luminescence peaks and the corresponding transitions are presented with excitation 526 nm (b). The delay time was 50 µs and gate width 500 µs in the measurements.

Table 5
Transitions and luminescence peaks of Nd^{3+} observed in apatite.

TRANSITION	APATITE [nm]
$^4F_{5/2} \rightarrow {}^4I_{9/2}$	804
$^4F_{3/2} \rightarrow {}^4I_{9/2}$	871

only, as at the longer delays the luminescence is overwhelmed by intensive Mn^{2+} band.

In the above, the luminescence emission in the visible spectral region was presented. In addition to it, also Nd^{3+} luminescence in the spectral region of 750–900 nm was measured. As observed in EEM of apatite, measured with excitation from 405 nm to 535 nm (Fig. 7a), the strongest intensities of Nd^{3+} bands are seen at excitation 526 nm. The Nd^{3+} luminescence bands are located at ~790–835 nm and ~850–940 nm, having the highest peaks at 804 nm and 871 nm, respectively (Fig. 7b, Table 5). Corresponding transitions are stated in the literature as $^4F_{5/2} \rightarrow {}^4I_{9/2}$ [7,101,102] and $^4F_{3/2} \rightarrow {}^4I_{9/2}$ [7,69,98,101–107]. Under the same measurement conditions (delay 50 μs and gate width 500 μs) no Nd^{3+} peaks were detected in calcite, which is most likely explained by the lower REE content in calcite than apatite at the Siilinjärvi complex.

3.2. Selection of optimized excitation wavelengths for apatite and calcite

The appearance of the luminescence spectrum depends significantly on the excitation wavelength. This is efficiently visualized as animations for excitation in the UV (video B1) and the visible (video C1) range. Normalization offers better comparison of the changed spectral shapes, thus the intensity values of apatite and calcite are normalized to the maximum of respective spectrum. The delay time in the measurements was 50 μs and the gate width 500 μs. For further applications in the luminescence analysis of natural minerals, it is useful to know which excitation wavelengths can be used to separate specific REEs or, on the other hand, to observe multiple REE^{3+} peaks simultaneously. Therefore, the laser-induced time-resolved luminescence spectra measured from apatite and calcite (Fig. 1) are illustrated as 2D contour presentations of EEMs (Figs. 8–10). The excitation regions (UV, Vis) are shown separately and for clarity, only the locations of the most prominent REE^{3+} peaks are marked as dashed lines. Deviating from Fig. 1, Contour EEM of apatite in the visible excitation region (Fig. 8), shows also spectral area of 750–900 nm presented in Fig. 7.

Contour-EEM of apatite in the visible excitation region shows luminescence from several REEs and no significant contribution of the Mn^{2+} band is observed (Fig. 8). The highest intensities for the Dy^{3+} peak at 578 nm are obtained with excitations at 427 nm and 452 nm. All the excitation wavelength regions, where Dy^{3+} is detected clearly, here 424–429 nm and 444–458 nm, are presented as grey boxes on the left side of the map, and stars show the most suitable excitations in our study. The same notation is used throughout all EEMs. Eu^{3+} can be excited from apatite using several spectral regions. With the delay of 50 μs luminescence from both mineral sites is seen and to separate Eu^{3+} peaks, those related to Ca (II) site are marked with pink. The good excitation wavelength for Eu^{3+} in apatite's Ca (I) site is 465 nm and for Eu^{3+} in Ca (II) sites either 435 nm, 473 nm, or 527 nm Sm^{3+} peaks have high intensities in apatite at wide excitation range. At Ca (I) site Sm^{3+} is well observed at excitations 405 nm and 473 nm. If also Sm^{3+} at Ca (II) site should be measured, the highest intensities were obtained with 414 nm excitation, marked with a pink star. The other REEs do not disturb the detection of Nd^{3+} peaks and in this research, the excitation 526 nm was the best.

In the apatite's EEM in UV excitation region (Fig. 9), background from some shorter living luminescence is here seen around the Tb^{3+} peaks (see also Fig. 1a), but they are clearly resolved and the highest intensities are obtained at 218 nm. The broad and intense Mn^{2+} band ~575–650 nm disturbs the detection of the other REEs, especially at excitations from 275 to 320 nm. The strongest intensities for Dy^{3+} peaks were observed at excitations of 287 nm and 326 nm. For Eu^{3+} the most suitable excitation wavelength at UV was 236 nm and the Sm^{3+} peak offered a strong signal when 210 nm was used for the excitation.

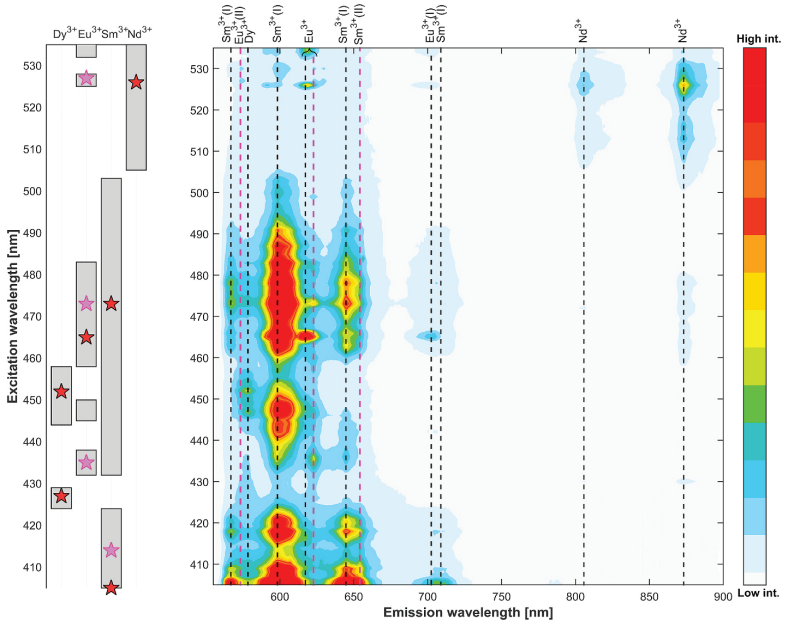

Fig. 8. Contour presentation of the excitation wavelengths in the visible for apatite as a function of luminescence emission wavelength (EEM-Vis). Locations of the selected REE^{3+} peaks are marked with black dashed lines and the appearance in Ca (II) site for Eu^{3+} and Sm^{3+} are marked with pink colour. The prominent excitation wavelengths are marked as grey boxes on the left side and the suggestions for optimal excitations are presented with stars.

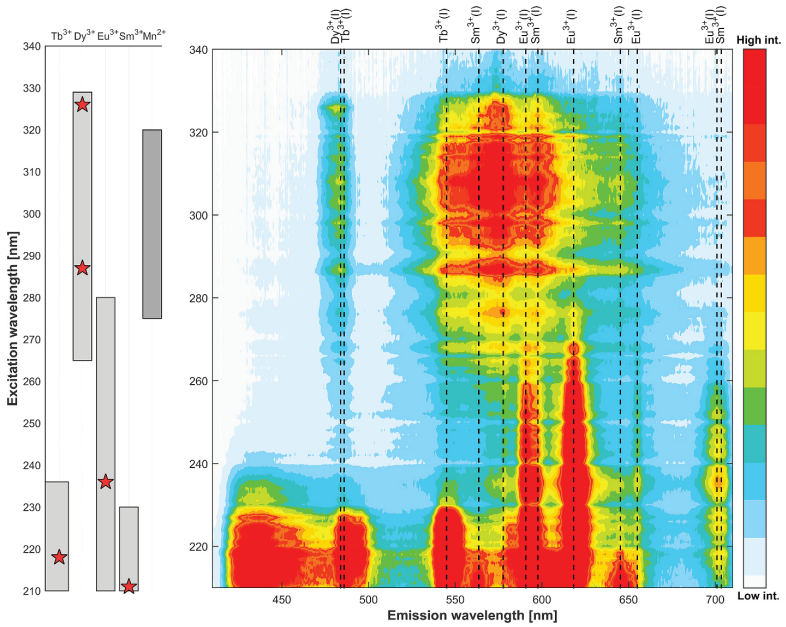

Fig. 9. Contour presentation of the excitation wavelengths in the UV for apatite as a function of luminescence emission wavelength (EEM-UV). Locations of the selected REE^{3+} peaks are marked with black dashed lines and suitable excitation wavelengths are marked as grey boxes on the left side of the contour and the suggestions for optimal excitations are presented with stars.

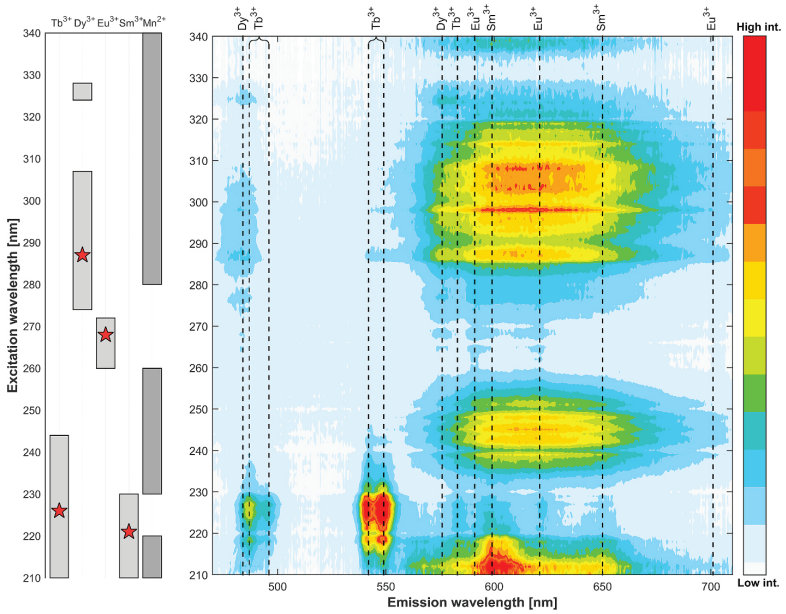

Fig. 10. Contour presentation of the excitation wavelengths in the UV for calcite as a function of luminescence emission wavelength (EEM-UV). The broad band of Mn^{2+} luminescence is observed ~575–650 nm at several excitation ranges. Locations of the selected REE^{3+} peaks are marked with black dashed lines. The prominent excitation wavelengths are marked as grey boxes on the left side and the suggestions for optimal excitations are presented with stars.

In calcite, the visible excitations strongly induce luminescence of Mn^{2+} and it readily dominates the spectra, as demonstrated in Fig. 1b. As an exception, the excitation 454 nm is applicable to Dy^{3+} and excitation 405 nm for the Sm^{3+}, but both have a notable background. For this reason, the contour-EEM for calcite is only presented in the UV excitation range (Fig. 10). For Tb^{3+} luminescence, the best excitation is at 226 nm. Because of Mn^{2+}, for the other REE^{3+} peaks the optimal excitation ranges (grey boxes) in calcite are not as wide as was shown for

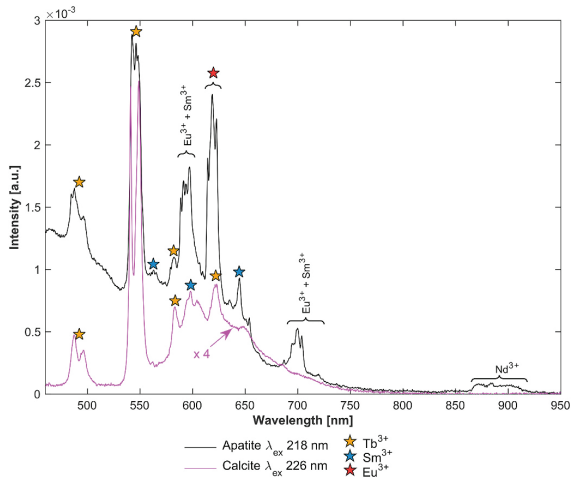

Fig. 11. Non-gated laser-induced luminescence measurements with the best excitations for Tb^{3+} for apatite (λ_{ex} 218 nm, black) and calcite (λ_{ex} 226 nm, violet). The Tb^{3+} peaks are marked with orange stars, Sm^{3+} as blue stars and Eu^{3+} as a red star. Note scaling of the violet spectrum.

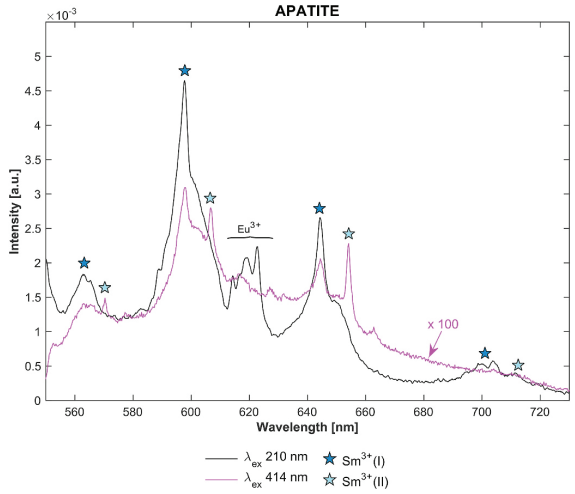

Fig. 12. Non-gated laser-induced luminescence measurements demonstrate how the optimal selection of excitation wavelength can show either only from Sm^{3+} in Ca (I) site (λ_{ex} 210 nm, black with blue stars) or also from Ca (II) site (λ_{ex} 414 nm, violet with blue and light blue stars). With excitation 210 nm also Eu^{3+}peaks are observed. Note the scaling of the violet spectrum.

apatite. The excitation of 287 nm is applicable to Dy^{3+} peaks and for Eu^{3+} and Sm^{3+} the excitations 268 nm and 221 nm, respectively, were found good.

The results offer possibility to locate those excitation wavelengths, where the emission signal of one or several REE^{3+} peaks are intensive and the disturbance of Mn^{2+} luminescence is minimal. The applicability was tested by measuring luminescence with a non-gated spectrometer with a few selected excitation wavelengths from the same samples. Without time-gating the long-living Mn^{2+} luminescence could readily dominate the spectrum even at low concentrations of Mn. However, the relative intensities of the REE peaks will not be comparable due to the varying lifetimes of the luminescence activators.

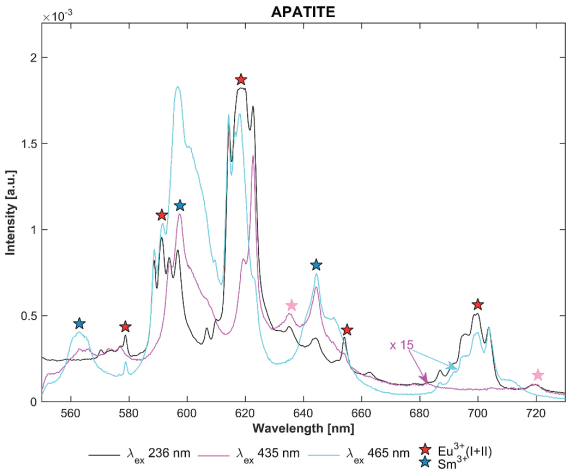

Fig. 13. Non-gated laser-induced luminescence measurements show peaks of Eu^{3+} (red stars) in apatite's Ca (II) site (λ_{ex} 435 nm, violet), Ca (I) site (λ_{ex} 465 nm, cyan) and on both of these sites (λ_{ex} 236 nm, black). Note the scaling of violet and cyan spectra. Sm^{3+} peaks are marked as blue stars.

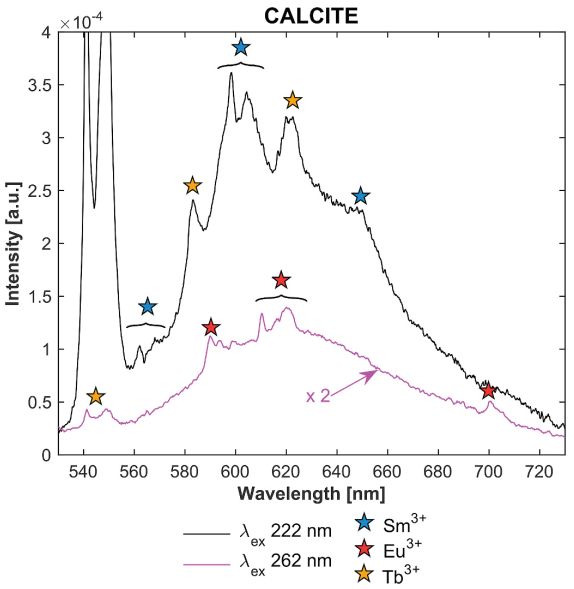

Fig. 14. Laser-induced non-gated luminescence measurements of calcite show the peaks of Tb^{3+} and Sm^{3+} (λ_{ex} 236 nm, black) and of Eu^{3+} (λ_{ex} 262 nm, violet). Note the scaling of the violet spectrum.

Firstly, the optimal excitations of Tb^{3+} for calcite and apatite were measured (Fig. 11). At these deep UV excitation wavelengths, both spectra show the luminescence peaks of Tb^{3+} and Sm^{3+} clearly (orange and blue stars), despite the background caused by the luminescence of Eu^{2+}, Ce^{3+}, and Mn^{2+}. In apatite (Fig. 11, black) also several Eu^{3+} related peaks (red star) and the Nd^{3+} band are seen.

Secondly, the occurrence of Sm^{3+} in both Ca (I) and Ca (II) sites in apatite's structure was measured. Luminescence of Sm^{3+} in the Ca (I) site can be detected in many excitation areas and here UV excitation 210 nm was selected (Fig. 12, black). Several peaks of Sm^{3+} in Ca (I) site

(blue stars) can be observed in addition to the luminescence peaks of Eu^{3+} occupying both sites. If also Sm^{3+} in Ca (II) is needed, the excitation at 414 nm (Fig. 12, violet) shows intensive luminescence peaks (light blue stars).

Eu^{3+} was also observed in the time-resolved measurements to occupy Ca (I) and Ca (II) sites in apatite, but optimal delay times were varying. In the non-gated measurement, the influence of the excitation wavelength seems to be decisive (Fig. 13). At excitation 236 nm (Fig. 13, black) the luminescence of Eu^{3+} is seen from Ca (I) and Ca (II) sites (red star). For comparison, excitation wavelength 435 nm shows Eu^{3+} peaks from Ca (II) site (Fig. 13, violet) and excitation 465 nm from Ca (I) site (Fig. 13, cyan). It can be remarked that the peaks at 636 nm and 720 nm (pink stars) are observed also here when the luminescence of Eu^{3+} from Ca (II) site is induced. This supports our assumption, that these peaks are related to Eu^{3+} and especially to Ca (II) site. Sm^{3+}peaks are seen in all spectra of Fig. 13.

For non-gated measurements of calcite, only UV excitations were used, as the luminescence of Mn^{2+} was strong already in the time-resolved study. Even with the selected UV excitations 222 nm and 262 nm, the background caused by Mn^{2+} in calcite is notable (Fig. 14). With excitation of 222 nm strong peaks of Sm^{3+} and Tb^{3+} are seen (Fig. 14, black). For non-gated measurement of Eu^{3+} in calcite, the excitation 262 nm seems to be the best (Fig. 14, violet).

4. Conclusion

The aim of the research was to study how REEs could be efficiently detected in natural apatite and calcite by optimizing the laser excitation wavelength. Luminescence from both minerals was systematically measured using excitations of 210–340 nm and 405–535 nm with tunable OPO and a time-resolved ICCD. The complex luminescence spectra of several REEs were studied and multiple suitable excitation wavelengths for detecting the REE^{3+} luminescence peaks from both apatite and calcite were presented. A broad band of Mn^{2+} was seen as a strong background, especially in calcite. For apatite, the luminescence of Eu^{3+} and Sm^{3+} occupying different Ca sites was observed with specific excitation regions, which would offer further information about the crystal structure. As a main result, the laser excitation region in deep UV around ~220–230 nm was discovered very promising. Within this range, the intensive luminescence of Tb^{3+} and Sm^{3+} was observed from both minerals and in the case of apatite peaks of $Nd^{3+}$and Eu^{3+} as occupying Ca (I) and Ca (II) sites were detected. In addition, the luminescence of Mn^{2+} is not strong with these excitations. Applicability of the optimized excitation wavelengths found here was demonstrated with a non-gated detector, as it would be more feasible for *in-situ* analysis of minerals.

Author statement

Sari Romppanen: Investigation, Resources, Software, Funding acquisition, Conceptualization, Visualization, Data Curation, Writing - Original Draft, Writing - Review & Editing. **Heikki Häkkänen**: Investigation, Resources, Software, Supervision, Funding acquisition, Conceptualization, Visualization, Writing - Review & Editing. **Saara Kaski**: Supervision, Funding acquisition, Conceptualization, Visualization, Project administration, Writing - Original Draft, Writing - Review & Editing.

Declaration of competing interest

The authors declare that they have no known competing financial interests or personal relationships that could have appeared to influence the work reported in this paper.

5 Acknowledgments

This study was partly supported by the Academy of Finland (Grant 281955 to S.K. and Grant 282240 to H.H.). S.R. wishes to acknowledge K.H. Renlund's Foundation for the grant which offered the possibility to finalize this work.

The apatite sample for the research was chosen from the samples kindly offered by Yara Suomi Oy and Pasi Heino and Aleksi Salo are appreciated for the co-operation. The Mn-bearing calcite sample from Siilinjärvi was from the collection offered by Geological Survey of Finland: Jari Nenonen and Satu Hietala are thanked for it.

Appendix A. Supplementary data

Supplementary data to this article can be found online at https://doi.org/10.1016/j.jlumin.2021.117929.

References

[1] R. Eggert, C. Wadia, C. Anderson, D. Bauer, F. Fields, L. Meinert, P. Taylor, Rare earths: market disruption, innovation, and global supply chains, Annu. Rev. Environ. Resour. 41 (2016) 199–222, https://doi.org/10.1146/annurev-environ-110615-085700.
[2] P. Henderson, General geochemical properties and abundances of the rare earth elements, in: P. Henderson (Ed.), Rare Earth Elem. Geochemistry, Elsevier Science Publishers B.V., 1984, pp. 1–32.
[3] G. Blasse, B.C. Grabmaier, Luminescent Materials, Springer-Verlag, Berlin/Heidelberg, 1994, https://doi.org/10.1007/978-3-642-79017-1.
[4] M. Gaft, R. Reisfeld, G. Panczer, Modern Luminescence Spectroscopy of Minerals and Materials, Springer, Heidelberg, 2005, https://doi.org/10.1007/b137490.
[5] L. Nasdala, J. Götze, J.M. Hanchar, M. Gaft, M.R. Krbetschek, Luminescence techniques in earth sciences, in: Spectrosc. Methods Mineral., Mineralogical Society of Great Britain and Ireland, Germany, 2004, pp. 43–91, https://doi.org/10.1180/EMU-notes.6.2.
[6] M. Gaft, R. Reisfeld, G. Panczer, P. Blank, G. Boulon, Laser-induced time-resolved luminescence of minerals, Spectrochim. Acta Part A Mol. Biomol. Spectrosc. 54 (1998) 2163–2175, https://doi.org/10.1016/S1386-1425(98)00134-6.
[7] P. Blanc, A. Baumer, F. Cesbron, D. Ohnenstetter, G. Panczer, G. Rémond, Systematic cathodoluminescence spectral analysis of synthetic doped minerals: anhydrite, apatite, calcite, fluorite, scheelite and zircon, in: Cathodoluminescence Geosci., Springer Berlin Heidelberg, 2000, pp. 127–160, https://doi.org/10.1007/978-3-662-04086-7_5.
[8] J. Götze, Application of cathodoluminescence microscopy and spectroscopy in geosciences, Microsc. Microanal. 18 (2012) 1270–1284, https://doi.org/10.1017/S1431927612001122.
[9] H. Friis, Luminescence Spectroscopy of Natural and Synthetic REE-Bearing Minerals, University of St. Andrews, 2009.
[10] S. Boggs, D. Krinsley, Application of Cathodoluminescence Imaging to the Study of Sedimentary Rocks, Cambridge University Press, 2006, https://doi.org/10.1017/cbo9780511535475.
[11] M. Pagel, V. Barbin, P. Blanc, D. Ohnenstetter (Eds.), Cathodoluminescence in Geosciences, Springer, Berlin, Heidelberg, 2000, https://doi.org/10.1007/978-3-662-04086-7.
[12] M. Gaft, R. Reisfeld, G. Panczer, Modern Luminescence Spectroscopy of Minerals and Materials, second ed., Springer Mineralogy, 2015 https://doi.org/10.1007/978-3-319-24765-6.
[13] M. Gaft, G. Panczer, R. Reisfeld, E. Uspensky, Laser-induced time-resolved luminescence as a tool for rare-earth element identification in minerals, Phys. Chem. Miner. 28 (2001) 347–363, https://doi.org/10.1007/s002690100163.
[14] M. Gaft, G. Panczer, Laser-induced time-resolved luminescence spectroscopy of minerals: a powerful tool for studying the nature of emission centres, Mineral. Petrol. 107 (2013) 363–372, https://doi.org/10.1007/s00710-013-0293-3.
[15] T. Al-Ani, F. Molnár, P. Lintinen, S. Leinonen, T. Al-Ani, F. Molnár, P. Lintinen, S. Leinonen, Geology and mineralogy of rare earth elements deposits and occurrences in Finland, Minerals 8 (2018) 356, https://doi.org/10.3390/min8080356.
[16] K. Puustinen, Geology of the Siilinjärvi Carbonatite Complex, Eastern Finland, Geologinen tutkimuslaitos, Otaniemi, 1971.
[17] I. Hornig-Kjarsgaard, Rare earth elements in sovitic carbonatites and their mineral phases, J. Petrol. 39 (1998) 2105–2121, https://doi.org/10.1093/petroj/39.11-12.2105.
[18] W.A. Deer, R.A. Howi, J. Zussman, An Introduction to the Rock-Forming Minerals, third ed., Mineralogical Society of Great Britain and Ireland, 2013 https://doi.org/10.1180/DHZ.
[19] G.A. Waychunas, Apatite luminescence, Rev. Mineral. Geochem. 48 (2002) 701–742, https://doi.org/10.2138/rmg.2002.48.19.
[20] J.-M. Baele, R. Dreesen, M. Dusar, Assessing apatite cathodoluminescence as a tool for sourcing oolitic ironstones 126 (2015) 57–67.
[21] J. Barbarand, M. Pagel, Cathodoluminescence study of apatite crystals, Am. Mineral. 86 (2001) 473–484, https://doi.org/10.2138/am-2001-0411.

[22] J.M. Hughes, J. Rakovan, The crystal structure of apatite, Ca5(PO4)3(F,OH,Cl), Rev. Mineral. Geochem. 48 (2002) 1–12, https://doi.org/10.2138/rmg.2002.48.1.

[23] J.M. Hughes, M. Cameron, K.D. Crowley, Structural variations in natural F, OH, and Cl apatites, Am. Mineral. 74 (1989) 870–876.

[24] G. Blasse, Influence of local charge compensation on site occupation and luminescence of apatites, J. Solid State Chem. 14 (1975) 181–184, https://doi.org/10.1016/0022-4596(75)90009-2.

[25] J.M. Hughes, M. Cameron, A. Mariano, Rare-earth-element ordering and structural variations in natural rare-earth'bearing apatites, Am. Mineral. 76 (1991) 1165–1173.

[26] M.E. Fleet, Y. Pan, Site preference of rare earth elements in fluorapatite, Am. Mineral. 80 (1995) 329–335, https://doi.org/10.2138/am-1995-3-414.

[27] M.E. Fleet, Y. Pan, Crystal chemistry of Rare Earth Elements in fluorapatite and some calc-silicates, Eur. J. Mineral 7 (1995) 591–606, https://doi.org/10.1127/ejm/7/3/0591.

[28] M.E. Fleet, Yuanming Pan, Site preference of rare earth elements in fluorapatite: binary (LREE+HREE)-substituted crystals, Am. Mineral. 82 (1997) 870–877, https://doi.org/10.2138/am-1997-9-1004.

[29] G. Chazot, M.A. Menzies, B. Harte, Determination of partition coefficients between apatite, clinopyroxene, amphibole, and melt in natural spinel lherzolites from Yemen: implications for wet melting of the lithospheric mantle, Geochem. Cosmochim. Acta 60 (1996) 423–437, https://doi.org/10.1016/0016-7037(95)00412-2.

[30] R.A. Mason, A.N. Mariano, Cathodoluminescence activation in manganese-bearing and rare earth-bearing synthetic calcites, Chem. Geol. 88 (1990) 191–206, https://doi.org/10.1016/0009-2541(90)90113-L.

[31] G. Blasse, M. Aguilar, Luminescence of natural calcite (CaCO3), J. Lumin. 29 (1984) 239–241, https://doi.org/10.1016/S0022-2313(84)90091-7.

[32] D. Habermann, R.D. Neuser, D.K. Richter, REE-activated cathodoluminescence of calcite and dolomite: high-resolution spectrometric analysis of CL emission (HRS-CL), Sediment, Geol. 101 (1996) 1–7, https://doi.org/10.1016/0037-0738(95)00086-0.

[33] M.B. Toffolo, G. Ricci, L. Caneve, I. Kaplan-Ashiri, Luminescence reveals variations in local structural order of calcium carbonate polymorphs formed by different mechanisms, Sci. Rep. 9 (2019) 1, https://doi.org/10.1038/s41598-019-52587-7.

[34] M. Gaft, L. Nagli, G. Panczer, G. Waychunas, N. Porat, The nature of unusual luminescence in natural calcite CaCO3, Am. Mineral. 93 (2008) 158–167, https://doi.org/10.2138/am.2008.2576.

[35] S. Bodył, Luminescence properties of Ce3+ and Eu2+ in fluorites and apatites, Mineralogia 40 (2009) 85–94, https://doi.org/10.2478/v10002-009-0007-y.

[36] R. Reisfeld, M. Gaft, G. Boulon, C. Panczer, C.K. Jørgensen, Laser-induced luminescence of rare-earth elements in natural fluor-apatites, J. Lumin. 69 (1996) 343–353, https://doi.org/10.1016/S0022-2313(96)00114-7.

[37] S.E. Sommer, Cathodoluminescence of carbonates, 2, Geological applications, Chem. Geol. 9 (1972) 275–284, https://doi.org/10.1016/0009-2541(72)90065-4.

[38] A. El Ali, V. Barbin, G. Calas, B. Cervelle, K. Ramseyer, J. Bouroulec, Mn2+-activated luminescence in dolomite, calcite and magnesite: quantitative determination of manganese and site distribution by EPR and CL spectroscopy, Chem. Geol. 104 (1993) 189–202, https://doi.org/10.1016/0009-2541(93)90150-H.

[39] A. Sidike, X.M. Wang, A. Sawuti, H.J. Zhu, I. Kusachi, N. Yamashita, Energy transfer among Pb, Ce and Mn in fluorescent calcite from Kuerle, Xinjiang, China, Phys. Chem. Miner. 33 (2006) 559–566, https://doi.org/10.1007/s00269-006-0103-0.

[40] D. Habermann, R.D. Neuser, D.K. Richter, Low limit of Mn2+-activated cathodoluminescence of calcite: state of the art, Sediment. Geol. 116 (1998) 13–24, https://doi.org/10.1016/S0037-0738(97)00118-8.

[41] V.A. Pedone, K.R. Cercone, R.C. Burruss, Activators of photoluminescence in calcite: evidence from high-resolution, laser-excited luminescence spectroscopy, Chem. Geol. 88 (1990) 183–190, https://doi.org/10.1016/0009-2541(90)90112-K.

[42] G. Walker, O.E. Abumere, B. Kamaluddin, Luminescence spectroscopy of Mn2+ centres in rock-forming carbonates, Mineral. Mag. 53 (1989) 201–211, https://doi.org/10.1180/minmag.1989.053.370.07.

[43] H.G. Machel, R.A. Mason, A.N. Mariano, A. Mucci, Causes and emission of luminescence in calcite and dolomite, in: H.Y.C. Charles E. Barker, Robert C. Burruss, Otto C. Kopp, Hans G. Machel, Donald J. Marshall, Paul Wright (Eds.), Lumin. Microsc. Spectrosc. Qual. Quant. Appl., SEPM Society for Sedimentary Geology, 1991, https://doi.org/10.2110/scn.91.25.0009.

[44] U. Kempe, J. Götze, Cathodoluminescence (CL) behaviour and crystal chemistry of apatite from rare-metal deposits, Mineral. Mag. 66 (2002) 151–172, https://doi.org/10.1180/0026461026610019.

[45] M. Gaft, R. Reisfeld, G. Panczer, G. Boulon, S. Shoval, B. Champagnon, Accommodation of rare-earths and manganese by apatite, Opt. Mater. 8 (1997) 149–156, https://doi.org/10.1016/S0925-3467(97)00042-6.

[46] K. Linganna, S. Ju, C. Basavapoornima, V. Venkatramu, C.K. Jayasankar, Journal of Asian Ceramic Societies Luminescence and decay characteristics of Tb 3+-doped fluorophosphate glasses Luminescence and decay characteristics of Tb 3+-doped fluorophosphate glasses, J. Asian Ceram. Soc. 6 (2018) 82–87, https://doi.org/10.1080/21870764.2018.1442674.

[47] T.H. Tran, K.A. Tran, T.K. Hoang, T.H. Pham, Q.M. Le, Fabrication and properties of terbium phosphate nanorods, Adv. Nat. Sci. Nanosci. Nanotechnol. 3 (2012), https://doi.org/10.1088/2043-6262/3/1/015010, 015010.

[48] T. Hayakawa, N. Kamata, K. Yamada, Visible emission characteristics in Tb3+-doped fluorescent glasses under selective excitation, J. Lumin. 68 (1996) 179–186, https://doi.org/10.1016/0022-2313(96)00022-1.

[49] M. Nazarov, E.J. Popovici, I. Arellano, D.Y. Noh, Luminescence properties of europium and terbium activated yttrium niobium/tantalate phosphors under VUV-UV excitation, Mold. J. Phys. Sci. 7 (2008) 433–437.

[50] H. Zhu, B. Qian, X. Zhou, Y. Song, K. Zheng, Y. Sheng, H. Zou, Tunable luminescence and energy transfer of Tb3+/Eu3+ co-doped cubic CaCO3 nanoparticles, J. Lumin. 203 (2018) 441–446, https://doi.org/10.1016/j.jlumin.2018.06.041.

[51] M.A. Mickens, Z. Assefa, Tunable luminescence and white light emission of novel multiphase sodium calcium silicate nanophosphors doped with Ce3+, Tb3+, and Mn2+ ions, J. Lumin. 145 (2014) 498–506, https://doi.org/10.1016/j.jlumin.2013.07.053.

[52] J.F.M. dos Santos, N.G.C. Astrath, M.L. Baesso, L.A.O. Nunes, T. Catunda, The effect of silica content on the luminescence properties of Tb3+-doped calcium aluminosilicate glasses, J. Lumin. 202 (2018) 363–369, https://doi.org/10.1016/j.jlumin.2018.05.008.

[53] C.J. Duan, W.F. Li, X.Y. Wu, H.H. Chen, X.X. Yang, J.T. Zhao, Y.B. Fu, Z.M. Qi, G. Bin Zhang, Z.S. Shi, Photoluminescence of Ce3+, Tb3+, Sm3+ or Gd3+ activated Ba3BP3O12 under the VUV and UV excitation, Mater. Sci. Eng. B Solid-State Mater. Adv. Technol. 121 (2005) 272–277, https://doi.org/10.1016/j.mseb.2005.04.013.

[54] F. Meng, X. Zhang, Y. Xu, J. Yang, Z. Cheng, Photoluminescence of Eu2+, Ce3+ and Tb3+ in a new potassium barium phosphate K2Ba3(P2O7)2 host lattice, J. Alloys Compd. (2017), https://doi.org/10.1016/j.jallcom.2017.09.224.

[55] H. Desirena, J. Molina-González, O. Meza, P. Castillo, J. Bujdud-Pérez, Multicolor and warm white emissions with a high color rendering index in a Tb3+/Eu3+-codoped phosphor ceramic plate, Materials 12 (2019) 2240, https://doi.org/10.3390/ma12142240.

[56] W. Chen, R. Sammynaiken, Y. Huang, Photostimulated luminescence of Tb3+ and Eu 3+ in zeolite-Y, Lumin, Solids J. Chem. Phys. 88 (2000) 836, https://doi.org/10.1063/1.373834.

[57] A. Akrim, D. Zambon, J.C. Cousseins, Optical properties of Tb3+ in the diphosphate CsYP2O7, J. Alloys Compd. 207–208 (1994) 99–101, https://doi.org/10.1016/0925-8388(94)90186-4.

[58] C.A. Kodaira, H.F. Brito, E.E.S. Teotonio, M.C.F.C. Felinto, O.L. Malta, G.E. S. Brito, Photoluminescence behavior of the Sm3+ and Tb3+ ions doped into the Gd2(WO4)3 matrix prepared by the Pechini and ceramic methods, J. Braz. Chem. Soc. 15 (2004) 890–896, https://doi.org/10.1590/S0103-50532004000600016.

[59] W.A. Pisarski, L. Zur, M. Sołtys, J. Pisarska, Terbium-terbium interactions in lead phosphate glasses, J. Appl. Phys. 113 (2013), https://doi.org/10.1063/1.4799592.

[60] G. Ju, Y. Hu, L. Chen, Y. Jin, Z. Yang, T. Wang, Photoluminescence properties of Ce3+and Tb3+-activated Ba2Mg(PO4)2, Opt. Mater. Express 5 (2015) 1, https://doi.org/10.1364/ome.5.000001.

[61] R.H. Mitchell, J. Xiong, A.N. Mariano, M.E. Fleet, Rare-earth-element-activated cathodoluminescence in apatite, Can. Mineral. 35 (1997) 979–998.

[62] M. Czaja, S. Bodył, R. Lisiecki, Z. Mazurak, Luminescence properties of Pr3+ and Sm3+ ions in natural apatites, Phys. Chem. Miner. 37 (2010) 425–433, https://doi.org/10.1007/s00269-009-0344-9.

[63] N.P.O. Homman, C. Yang, K.G. Malmqvist, A highly sensitive method for rare-earth element analysis using ionoluminescence combined with PIXE, Nucl. Instrum. Methods Phys. Res. A. 353 (1994) 610–614, https://doi.org/10.1016/0168-9002(94)91734-5.

[64] D. Habermann, J. Meijer, R.D. Neuser, D.K. Richter, C. Rolfs, A. Stephan, Micro-PIXE and quantitative cathodoluminescence spectroscopy: combined high resolution trace element analyses in minerals, Nucl. Instrum. Methods Phys. Res. Sect. B Beam Interact. Mater. Atoms 150 (1999) 470–477, https://doi.org/10.1016/S0168-583X(98)00926-4.

[65] H.M. Farok, G.A. Saunders, W. Poon, H. Vass, Low temperature fluorescence, valence state and elastic anomalies of samarium phosphate glasses, J. Non-Cryst. Solids 142 (1992) 175–180, https://doi.org/10.1016/S0022-3093(05)80022-5.

[66] K. Annapurna, R.N. Dwivedi, P. Kundu, S. Buddhudu, Fluorescence properties of Sm3+: ZnCl2-BaCl2-LiCl glass, Mater. Res. Bull. 38 (2003) 429–436, https://doi.org/10.1016/S0025-5408(02)01068-1.

[67] Y. Wen, Y. Wang, B. Liu, F. Zhang, Luminescence properties of Ca4Y6(SiO4)6O: RE3+ (RE = Eu, Tb, Dy, Sm and Tm) under vacuum ultraviolet excitation, Opt. Mater. 34 (2012) 889–892, https://doi.org/10.1016/J.OPTMAT.2011.12.005.

[68] Z. Yang, D. Xu, J. Sun, Synthesis and Luminescence Properties of Ba3Lu(PO4)3: Sm3+ phosphor for white light- emitting diodes, Optic Express 25 (2017), https://doi.org/10.1364/OE.25.00A391. A391–A401.

[69] F.S. Liu, Q.L. Liu, J.K. Liang, J. Luo, L.T. Yang, G.B. Song, Y. Zhang, L.X. Wang, J. N. Yao, G.H. Rao, Optical spectra of Ln3+(Nd3+, Sm3+, Dy3+, Ho3+, Er3+)-doped Y3GaO6, J. Lumin. 111 (2005) 61–68, https://doi.org/10.1016/J.JLUMIN.2004.06.005.

[70] C.K. Jayasankar, P. Babu, Optical properties of Sm3+ ions in lithium borate and lithium fluoroborate glasses, J. Alloys Compd. 307 (2000) 82–95, https://doi.org/10.1016/S0925-8388(00)00888-4.

[71] S. Bodył, M. Czaja, Z. Mazurak, Optical properties of Pr3+, Sm3+ and Er3+ ions in apatite, fluorite and phosphate glasses, Phys. Procedia. 2 (2009) 515–525, https://doi.org/10.1016/j.phpro.2009.07.037.

[72] B.V. Rao, U. Rambabu, S. Buddhudu, Emission analysis of Sm3+:Ca4GdO(BO3)3 powder phosphor, Mater. Lett. 61 (2007) 2868–2871, https://doi.org/10.1016/j.matlet.2007.01.042.

[73] G.S.R. Raju, S. Buddhudu, Emission analysis of Sm3+ and Dy3+:MgLaLiSi2O7 powder phosphors, Spectrochim. Acta Part A Mol. Biomol. Spectrosc. 70 (2008) 601–605, https://doi.org/10.1016/J.SAA.2007.08.004.
[74] R. Jagannathan, M. Kottaisamy, Eu3+ luminescence: a spectral probe in M5(PO4) 3X apatites, (M = Ca or Sr; X = F–, Cl–, Br– or OH–), J. Phys. Condens. Matter 7 (1995) 8453–8466, https://doi.org/10.1088/0022-3727/27/10/034.
[75] M. Gaft, R. Reisfeld, G. Panczer, S. Shoval, C. Garapon, G. Boulon, W. Strek, Luminescence of Eu(III), Pr(III) and Sm(III) in carbonate-fluor-apatite, Acta Phys. Pol. Ser. A. 90 (1996) 267–274.
[76] R. Ternane, M. Trabelsi-Ayedi, N. Kbir-Ariguib, B. Piriou, Luminescent properties of Eu3+ in calcium hydroxyapatite, J. Lumin. 81 (1999) 165–170, https://doi.org/10.1016/S0022-2313(98)00172-0.
[77] M. Gaft, R. Reisfeld, G. Panczer, S. Shoval, B. Champagnon, G. Boulon, Eu3+ luminescence in high-symmetry sites of natural apatite, J. Lumin. 72–74 (1997) 572–574, https://doi.org/10.1016/S0022-2313(96)00229-3.
[78] B. Piriou, D. Fahmi, J. Dexpert-Ghys, A. Taitai, J.L. Lacout, Unusual fluorescent properties of Eu3+ in oxyapatites, J. Lumin. 39 (1987) 97–103, https://doi.org/10.1016/0022-2313(87)90036-6.
[79] B. Piriou, A. Elfakir, M. Quarton, Site-selective spectroscopy of Eu3+-doped sodium lead phosphate apatite, J. Lumin. 93 (2001) 17–26, https://doi.org/10.1016/S0022-2313(01)00172-7.
[80] A. Zounani, D. Zambon, J.C. Cousseins, Spectroscopic study of Eu3+ in the fluorapatite Sr10F2(PO4)6, J. Alloys Compd. 207–208 (1994) 94–98, https://doi.org/10.1016/0925-8388(94)90185-6.
[81] A. Zounani, D. Zambon, J.C. Cousseins, Optical properties of Eu3+ activated Sr10F2(PO4)6 elaborated by coprecipitation, J. Alloys Compd. 188 (1992) 82–86, https://doi.org/10.1016/0925-8388(92)90648-S.
[82] F. Nouri, G. Panczer, Y. Guyot, M. Trabelsi-Ayadi, R. Ternane, Synthesis and luminescent properties of Eu3+-doped phosphate-sulfate fluorapatites Ca10−xNax(PO4)6−x(SO4)xF2, J. Lumin. 192 (2017) 590–594, https://doi.org/10.1016/j.jlumin.2017.07.033.
[83] V. Jokanović, B. Čolović, N. Jović, The luminescent properties of yttrium oxyapatite doped with Eu 3+ ions, Sci. Sinter. 46 (2014) 129–134, https://doi.org/10.2298/SOS1401129J.
[84] A. Tesch, C. Wenisch, K.H. Herrmann, J.R. Reichenbach, P. Warncke, D. Fischer, F.A. Müller, Luminomagnetic Eu3+ - and Dy3+ -doped hydroxyapatite for multimodal imaging, Mater. Sci. Eng. C 81 (2017) 422–431, https://doi.org/10.1016/j.msec.2017.08.032.
[85] M. Gaft, R. Reisfeld, G. Panczer, O. Ioffe, I. Sigal, Laser-induced time-resolved luminescence as a means for discrimination of oxidation states of Eu in minerals, J. Alloys Compd. 323–324 (2001) 842–846, https://doi.org/10.1016/S0925-8388(01)01157-4.
[86] R. El Ouenzerfi, N. Kbir-Ariguib, M. Trabelsi-Ayedi, B. Piriou, Spectroscopic study of Eu3+ in strontium hydroxyapatite Sr10(PO4)6(OH)2, J. Lumin. 85 (1999) 71–77, https://doi.org/10.1016/S0022-2313(99)00149-0.
[87] M. Marques Fernandes, M. Schmidt, T. Stumpf, C. Walther, D. Bosbach, R. Klenze, T. Fanghänel, Site-selective time-resolved laser fluorescence spectroscopy of Eu3 + in calcite, J. Colloid Interface Sci. (2008), https://doi.org/10.1016/j.jcis.2008.01.017.
[88] B. Piriou, M. Fedoroff, J. Jeanjean, L. Bercis, Characterization of the sorption of europium(lll) on calcite by site-selective and time-resolved luminescence spectroscopy, J. Colloid Interface Sci. (1997), https://doi.org/10.1006/jcis.1997.5115.
[89] K. Binnemans, Interpretation of europium(III) spectra, Coord. Chem. Rev. 295 (2015) 1–45, https://doi.org/10.1016/J.CCR.2015.02.015.
[90] Y. Il Jeon, L. Krishna Bharat, J.S. Yu, Synthesis and luminescence properties of Eu3+/Dy3+ ions co-doped Ca2La8(GeO4)6O2 phosphors for white-light applications, J. Alloys Compd. 620 (2015) 263–268, https://doi.org/10.1016/j.jallcom.2014.09.135.
[91] T.B. de Queiroz, M.B.S. Botelho, T.S. Gonçalves, M.R. Dousti, A.S.S. de Camargo, New fluorophosphate glasses co-doped with Eu3+ and Tb3+ as candidates for generating tunable visible light, J. Crit. Care 38 (2015) 315–321, https://doi.org/10.1016/j.jallcom.2015.06.066.
[92] Y.N. Xue, F. Xiao, Q.Y. Zhang, Enhanced red light emission from LaBSiO5:Eu3+, R3+ (R = Bi or Sm) phosphors, Spectrochim. Acta Part A Mol. Biomol. Spectrosc. 78 (2011) 607–611, https://doi.org/10.1016/J.SAA.2010.11.030.
[93] M. Gaft, R. Reisfeld, G. Panczer, E. Uspensky, B. Varrel, G. Boulon, Luminescence of Pr3+ in minerals, Opt. Mater. 13 (1999) 71–79, https://doi.org/10.1016/S0925-3467(99)00014-2.
[94] M. Czaja, R. Lisiecki, Luminescence of agrellite specimen from the kipawa river locality, Minerals 9 (2019) 752, https://doi.org/10.3390/min9120752.
[95] M.B. Czaja, S. Bodył-Gajowska, Z. Mazurak, Steady-state luminescence measurement for qualitative identification of rare earth ions in minerals, J. Mineral. Petrol. Sci. 108 (2013) 47–54, https://doi.org/10.2465/jmps.111229.
[96] M. Gaft, Y. Raichlin, Luminescence of 5d–4f transitions of Pr3+ in natural fluorite CaF2, anhydrite CaSO4 and apatite Ca5(PO4)3F, Phys. Chem. Miner. 47 (2020) 1–8, https://doi.org/10.1007/s00269-019-01074-6.
[97] M. Soltys, L. Żur, J. Pisarska, W.A. Pisarski, Excitation and luminescence of Dy3+ ions in PbO-P2O5-Ga2O3 glass system, J. Rare Earths 32 (2014) 213–216, https://doi.org/10.1016/S1002-0721(14)60054-5.
[98] M. Seshadri, K. Venkata Rao, J. Lakshmana Rao, K.S.R. Koteswara Rao, Y. C. Ratnakaram, Spectroscopic investigations and luminescence spectra of Nd3+ and Dy3+ doped different phosphate glasses, J. Lumin. 130 (2010) 536–543, https://doi.org/10.1016/J.JLUMIN.2009.10.027.
[99] V.K. Rai, S.B. Rai, D.K. Rai, Optical studies of Dy3+ doped tellurite glass: observation of yellow-green upconversion, Optic Commun. 257 (2006) 112–119, https://doi.org/10.1016/j.optcom.2005.07.022.
[100] W.Y. Zhao, S.L. An, B. Fan, S.B. Li, Y.T. Dai, Photoluminescence and cathodoluminescence properties of a novel CaLaGa3O7:Dy3+ phosphor, Chin. Sci. Bull. 57 (2012) 827–831, https://doi.org/10.1007/s11434-011-4938-5.
[101] M. Suta, Ž. Antić, V. Đorđević, S. Kuzman, M.D. Dramićanin, A. Meijerink, Making Nd3+ a sensitive luminescent thermometer for physiological temperatures—an account of pitfalls in Boltzmann thermometry, Nanomaterials 10 (2020) 543, https://doi.org/10.3390/nano10030543.
[102] Y.C. Ratnakaram, N.V. Srihari, A.V. Kumar, D.T. Naidu, R.P.S. Chakradhar, Optical absorption and photoluminescence properties of Nd3+ doped mixed alkali phosphate glasses-spectroscopic investigations, Spectrochim. Acta Part A Mol. Biomol. Spectrosc. 72 (2009) 171–177, https://doi.org/10.1016/J.SAA.2008.09.008.
[103] D. de Ligny, G. Panczer, D. Caurant, D.R. Neuville, Contribution of neodymium optical spectroscopy to the crystal growth study of a silicate apatite in a glassy matrix, Opt. Mater. 30 (2008) 1694–1698, https://doi.org/10.1016/j.optmat.2007.07.008.
[104] J.B. Gruber, C.A. Morrison, M.D. Seltzer, A.O. Wright, M.P. Nadler, T.H. Allik, J. A. Hutchinson, B.H.T. Chai, Site-selective excitation and polarized absorption spectra of Nd3+ in Sr5(PO4)3F and Ca5(PO4)3F, J. Appl. Phys. 79 (1996) 1746–1758, https://doi.org/10.1063/1.360964.
[105] S. Damodaraiah, V. Reddy Prasad, Y.C. Ratnakaram, Investigations on spectroscopic properties of Nd3+ doped alkali bismuth phosphate glasses for 1.053 μm laser applications, Optic Laser. Technol. 113 (2019) 322–329, https://doi.org/10.1016/J.OPTLASTEC.2019.01.010.
[106] G. Lakshminarayana, R. Vidya Sagar, S. Buddhudu, NIR luminescence from Er3+/Yb3+, Tm3+/Yb3+, Er3+/Tm3+ and Nd3+ ions-doped zincborotellurite glasses for optical amplification, J. Lumin. 128 (2008) 690–695, https://doi.org/10.1016/J.JLUMIN.2007.11.081.
[107] C. Lenz, D. Talla, K. Ruschel, R. Škoda, J. Götze, L. Nasdala, Factors affecting the Nd3+ (REE3+) luminescence of minerals, Mineral. Petrol. 107 (2013) 415–428, https://doi.org/10.1007/s00710-013-0286-2.

DEPARTMENT OF CHEMISTRY, UNIVERSITY OF JYVÄSKYLÄ
RESEARCH REPORT SERIES

1. Vuolle, Mikko: Electron paramagnetic resonance and molecular orbital study of radical ions generated from (2.2)metacyclophane, pyrene and its hydrogenated compounds by alkali metal reduction and by thallium(III)trifluoroacetate oxidation. (99 pp.) 1976
2. Pasanen, Kaija: Electron paramagnetic resonance study of cation radical generated from various chlorinated biphenyls. (66 pp.) 1977
3. Carbon-13 Workshop, September 6-8, 1977. (91 pp.) 1977
4. Laihia, Katri: On the structure determination of norbornane polyols by NMR spectroscopy. (111 pp.) 1979
5. Nyrönen, Timo: On the EPR, ENDOR and visible absorption spectra of some nitrogen containing heterocyclic compounds in liquid ammonia. (76 pp.) 1978
6. Talvitie, Antti: Structure determination of some sesquiterpenoids by shift reagent NMR. (54 pp.) 1979
7. Häkli, Harri: Structure analysis and molecular dynamics of cyclic compounds by shift reagent NMR. (48 pp.) 1979
8. Pitkänen, Ilkka: Thermodynamics of complexation of 1,2,4-triazole with divalent manganese, cobalt, nickel, copper, zinc, cadmium and lead ions in aqueous sodium perchlorate solutions. (89 pp.) 1980
9. Asunta, Tuula: Preparation and characterization of new organometallic compounds synthesized by using metal vapours. (91 pp.) 1980
10. Sattar, Mohammad Abdus: Analyses of MCPA and its metabolites in soil. (57 pp.) 1980
11. Bibliography 1980. (31 pp.) 1981
12. Knuuttila, Pekka: X-Ray structural studies on some divalent 3d metal compounds of picolinic and isonicotinic acid N-oxides. (77 pp.) 1981
13. Bibliography 1981. (33 pp.) 1982
14. 6^{th} National NMR Symposium, September 9-10, 1982, Abstracts. (49 pp.) 1982
15. Bibliography 1982. (38 pp.) 1983
16. Knuuttila, Hilkka: X-Ray structural studies on some Cu(II), Co(II) and Ni(II) complexes with nicotinic and isonicotinic acid N-oxides. (54 pp.) 1983
17. Symposium on inorganic and analytical chemistry May 18, 1984, Program and Abstracts. (100 pp.) 1984
18. Knuutinen, Juha: On the synthesis, structure verification and gas chromatographic determination of chlorinated catechols and guaiacols occuring in spent bleach liquors of kraft pulp mill. (30 pp.) 1984
19. Bibliography 1983. (47 pp.) 1984
20. Pitkänen, Maija: Addition of BrCl, B_2 and Cl_2 to methyl esters of propenoic and 2-butenoic acid derivatives and ^{13}C NMR studies on methyl esters of saturated aliphatic mono- and dichlorocarboxylic acids. (56 pp.) 1985
21. Bibliography 1984. (39 pp.) 1985
22. Salo, Esa: EPR, ENDOR and TRIPLE spectroscopy of some nitrogen heteroaromatics in liquid ammonia. (111 pp.) 1985

23. Humppi, Tarmo: Synthesis, identification and analysis of dimeric impurities of chlorophenols. (39 pp.) 1985
24. Aho, Martti: The ion exchange and adsorption properties of sphagnum peat under acid conditions. (90 pp.) 1985
25. Bibliography 1985 (61 pp.) 1986
26. Bibliography 1986. (23 pp.) 1987
27. Bibliography 1987. (26 pp.) 1988
28. Paasivirta, Jaakko (Ed.): Structures of organic environmental chemicals. (67 pp.) 1988
29. Paasivirta, Jaakko (Ed.): Chemistry and ecology of organo-element compounds. (93 pp.) 1989
30. Sinkkonen, Seija: Determination of crude oil alkylated dibenzothiophenes in environment. (35 pp.) 1989
31. Kolehmainen, Erkki (Ed.): XII National NMR Symposium Program and Abstracts. (75 pp.) 1989
32. Kuokkanen, Tauno: Chlorocymenes and Chlorocymenenes: Persistent chlorocompounds in spent bleach liquors of kraft pulp mills. (40 pp.) 1989
33. Mäkelä, Reijo: ESR, ENDOR and TRIPLE resonance study on substituted 9,10-anthraquinone radicals in solution. (35 pp.) 1990
34. Veijanen, Anja: An integrated sensory and analytical method for identification of off-flavour compounds. (70 pp.) 1990
35. Kasa, Seppo: EPR, ENDOR and TRIPLE resonance and molecular orbital studies on a substitution reaction of anthracene induced by thallium(III) in two fluorinated carboxylic acids. (114 pp.) 1990
36. Herve, Sirpa: Mussel incubation method for monitoring organochlorine compounds in freshwater recipients of pulp and paper industry. (145 pp.) 1991
37. Pohjola, Pekka: The electron paramagnetic resonance method for characterization of Finnish peat types and iron (III) complexes in the process of peat decomposition. (77 pp.) 1991
38. Paasivirta, Jaakko (Ed.): Organochlorines from pulp mills and other sources. Research methodology studies 1988-91. (120 pp.) 1992
39. Veijanen, Anja (Ed.): VI National Symposium on Mass Spectrometry, May 13-15, 1992, Abstracts. (55 pp.) 1992
40. Rissanen, Kari (Ed.): The 7. National Symposium on Inorganic and Analytical Chemistry, May 22, 1992, Abstracts and Program. (153 pp.) 1992
41. Paasivirta, Jaakko (Ed.): CEOEC'92, Second Finnish-Russian Seminar: Chemistry and Ecology of Organo-Element Compounds. (93 pp.) 1992
42. Koistinen, Jaana: Persistent polychloroaromatic compounds in the environment: structure-specific analyses. (50 pp.) 1993
43. Virkki, Liisa: Structural characterization of chlorolignins by spectroscopic and liquid chromatographic methods and a comparison with humic substances. (62 pp.) 1993
44. Helenius, Vesa: Electronic and vibrational excitations in some

biologically relevant molecules. (30 pp.) 1993

45. Leppä-aho, Jaakko: Thermal behaviour, infrared spectra and x-ray structures of some new rare earth chromates(VI). (64 pp.) 1994
46. Kotila, Sirpa: Synthesis, structure and thermal behavior of solid copper(II) complexes of 2-amino-2- hydroxymethyl-1,3-propanediol. (111 pp.) 1994
47. Mikkonen, Anneli: Retention of molybdenum(VI), vanadium(V) and tungsten(VI) by kaolin and three Finnish mineral soils. (90 pp.) 1995
48. Suontamo, Reijo: Molecular orbital studies of small molecules containing sulfur and selenium. (42 pp.) 1995
49. Hämäläinen, Jouni: Effect of fuel composition on the conversion of fuel-N to nitrogen oxides in the combustion of small single particles. (50 pp.) 1995
50. Nevalainen, Tapio: Polychlorinated diphenyl ethers: synthesis, NMR spectroscopy, structural properties, and estimated toxicity. (76 pp.) 1995
51. Aittola, Jussi-Pekka: Organochloro compounds in the stack emission. (35 pp.) 1995
52. Harju, Timo: Ultrafast polar molecular photophysics of (dibenzylmethine)borondifluoride and 4-aminophthalimide in solution. (61 pp.) 1995
53. Maatela, Paula: Determination of organically bound chlorine in industrial and environmental samples. (83 pp.) 1995
54. Paasivirta, Jaakko (Ed.): CEOEC'95, Third Finnish-Russian Seminar: Chemistry and Ecology of Organo-Element Compounds. (109 pp.) 1995
55. Huuskonen, Juhani: Synthesis and structural studies of some supramolecular compounds. (54 pp.) 1995
56. Palm, Helena: Fate of chlorophenols and their derivatives in sawmill soil and pulp mill recipient environments. (52 pp.) 1995
57. Rantio, Tiina: Chlorohydrocarbons in pulp mill effluents and their fate in the environment. (89 pp.) 1997
58. Ratilainen, Jari: Covalent and non-covalent interactions in molecular recognition. (37 pp.) 1997
59. Kolehmainen, Erkki (Ed.): XIX National NMR Symposium, June 4-6, 1997, Abstracts. (89 pp.) 1997
60. Matilainen, Rose: Development of methods for fertilizer analysis by inductively coupled plasma atomic emission spectrometry. (41 pp.) 1997
61. Koistinen, Jari (Ed.): Spring Meeting on the Division of Synthetic Chemistry, May 15-16, 1997, Program and Abstracts. (36 pp.) 1997
62. Lappalainen, Kari: Monomeric and cyclic bile acid derivatives: syntheses, NMR spectroscopy and molecular recognition properties. (50 pp.) 1997
63. Laitinen, Eira: Molecular dynamics of cyanine dyes and phthalimides in solution: picosecond laser studies. (62 pp.) 1997
64. Eloranta, Jussi: Experimental and theoretical studies on some

quinone and quinol radicals. (40 pp.) 1997

65. Oksanen, Jari: Spectroscopic characterization of some monomeric and aggregated chlorophylls. (43 pp.) 1998
66. Häkkänen, Heikki: Development of a method based on laser-induced plasma spectrometry for rapid spatial analysis of material distributions in paper coatings. (60 pp.) 1998
67. Virtapohja, Janne: Fate of chelating agents used in the pulp and paper industries. (58 pp.) 1998
68. Airola, Karri: X-ray structural studies of supramolecular and organic compounds. (39 pp.) 1998
69. Hyötyläinen, Juha: Transport of lignin–type compounds in the receiving waters of pulp mills. (40 pp.) 1999
70. Ristolainen, Matti: Analysis of the organic material dissolved during totally chlorine-free bleaching. (40 pp.) 1999
71. Eklin, Tero: Development of analytical procedures with industrial samples for atomic emission and atomic absorption spectrometry. (43 pp.) 1999
72. Välisaari, Jouni: Hygiene properties of resol-type phenolic resin laminates. (129 pp.) 1999
73. Hu, Jiwei: Persistent polyhalogenated diphenyl ethers: model compounds syntheses, characterization and molecular orbital studies. (59 pp.) 1999
74. Malkavaara, Petteri: Chemometric adaptations in wood processing chemistry. (56 pp.) 2000
75. Kujala Elena, Laihia Katri, Nieminen Kari (Eds.): NBC 2000, Symposium on Nuclear, Biological and Chemical Threats in the 21st Century. (299 pp.) 2000
76. Rantalainen, Anna-Lea: Semipermeable membrane devices in monitoring persistent organic pollutants in the environment. (58 pp.) 2000
77. Lahtinen, Manu: *In situ* X-ray powder diffraction studies of Pt/C, CuCl/C and Cu_2O/C catalysts at elevated temperatures in various reaction conditions. (92 pp.) 2000
78. Tamminen, Jari: Syntheses, empirical and theoretical characterization, and metal cation complexation of bile acid-based monomers and open/closed dimers. (54 pp.) 2000
79. Vatanen, Virpi: Experimental studies by EPR and theoretical studies by DFT calculations of α-amino-9,10-anthraquinone radical anions and cations in solution. (37 pp.) 2000
80. Kotilainen, Risto: Chemical changes in wood during heating at 150-260 °C. (57 pp.) 2000
81. Nissinen, Maija: X-ray structural studies on weak, non-covalent interactions in supramolecular compounds. (69 pp.) 2001
82. Wegelius, Elina: X-ray structural studies on self-assembled hydrogen-bonded networks and metallosupramolecular complexes. (84 pp.) 2001
83. Paasivirta, Jaakko (Ed.): CEOEC'2001, Fifth Finnish-Russian Seminar: Chemistry and Ecology of Organo-Element Compounds. (163 pp.) 2001
84. Kiljunen, Toni: Theoretical studies on spectroscopy and

atomic dynamics in rare gas solids. (56 pp.) 2001

85. Du, Jin: Derivatives of dextran: synthesis and applications in oncology. (48 pp.) 2001
86. Koivisto, Jari: Structural analysis of selected polychlorinated persistent organic pollutants (POPs) and related compounds. (88 pp.) 2001
87. Feng, Zhinan: Alkaline pulping of non-wood feedstocks and characterization of black liquors. (54 pp.) 2001
88. Halonen, Markku: Lahon havupuun käyttö sulfaattiprosessin raaka-aineena sekä havupuun lahontorjunta. (90 pp.) 2002
89. Falábu, Dezsö: Synthesis, conformational analysis and complexation studies of resorcarene derivatives. (212 pp.) 2001
90. Lehtovuori, Pekka: EMR spectroscopic studies on radicals of ubiquinones Q-*n*, vitamin K_3 and vitamine E in liquid solution. (40 pp.) 2002
91. Perkkalainen, Paula: Polymorphism of sugar alcohols and effect of grinding on thermal behavior on binary sugar alcohol mixtures. (53 pp.) 2002
92. Ihalainen, Janne: Spectroscopic studies on light-harvesting complexes of green plants and purple bacteria. (42 pp.) 2002
93. Kunttu, Henrik, Kiljunen, Toni (Eds.): 4th International Conference on Low Temperature Chemistry. (159 pp.) 2002
94. Väisänen, Ari: Development of methods for toxic element analysis in samples with environmental concern by ICP-AES and ETAAS. (54 pp.) 2002
95. Luostarinen, Minna: Synthesis and characterisation of novel resorcarene derivatives. (200 pp.) 2002
96. Louhelainen, Jarmo: Changes in the chemical composition and physical properties of wood and nonwood black liquors during heating. (68 pp.) 2003
97. Lahtinen, Tanja: Concave hydrocarbon cyclophane π-prismands. (65 pp.) 2003
98. Laihia, Katri (Ed.): NBC 2003, Symposium on Nuclear, Biological and Chemical Threats – A Crisis Management Challenge. (245 pp.) 2003
99. Oasmaa, Anja: Fuel oil quality properties of wood-based pyrolysis liquids. (32 pp.) 2003
100. Virtanen, Elina: Syntheses, structural characterisation, and cation/anion recognition properties of nano-sized bile acid-based host molecules and their precursors. (123 pp.) 2003
101. Nättinen, Kalle: Synthesis and X-ray structural studies of organic and metallo-organic supramolecular systems. (79 pp.) 2003
102. Lampiselkä, Jarkko: Demonstraatio lukion kemian opetuksessa. (285 pp.) 2003
103. Kallioinen, Jani: Photoinduced dynamics of $Ru(dcbpy)_2(NCS)_2$ – in solution and on nanocrystalline titanium dioxide thin films. (47 pp.) 2004
104. Valkonen, Arto (Ed.): VII Synthetic Chemistry Meeting and XXVI Finnish NMR Symposium. (103 pp.) 2004

105. Vaskonen, Kari: Spectroscopic studies on atoms and small molecules isolated in low temperature rare gas matrices. (65 pp.) 2004
106. Lehtovuori, Viivi: Ultrafast light induced dissociation of $Ru(dcbpy)(CO)_2I_2$ in solution. (49 pp.) 2004
107. Saarenketo, Pauli: Structural studies of metal complexing Schiff bases, Schiff base derived *N*-glycosides and cyclophane π-prismands. (95 pp.) 2004
108. Paasivirta, Jaakko (Ed.): CEOEC'2004, Sixth Finnish-Russian Seminar: Chemistry and Ecology of Organo-Element Compounds. (147 pp.) 2004
109. Suontamo, Tuula: Development of a test method for evaluating the cleaning efficiency of hard-surface cleaning agents. (96 pp.) 2004
110. Güneş, Minna: Studies of thiocyanates of silver for nonlinear optics. (48 pp.) 2004
111. Ropponen, Jarmo: Aliphatic polyester dendrimers and dendrons. (81 pp.) 2004
112. Vu, Mân Thi Hong: Alkaline pulping and the subsequent elemental chlorine-free bleaching of bamboo (*Bambusa procera*). (69 pp.) 2004
113. Mansikkamäki, Heidi: Self-assembly of resorcinarenes. (77 pp.) 2006
114. Tuononen, Heikki M.: EPR spectroscopic and quantum chemical studies of some inorganic main group radicals. (79 pp.) 2005
115. Kaski, Saara: Development of methods and applications of laser-induced plasma spectroscopy in vacuum ultraviolet. (44 pp.) 2005
116. Mäkinen, Riika-Mari: Synthesis, crystal structure and thermal decomposition of certain metal thiocyanates and organic thiocyanates. (119 pp.) 2006
117. Ahokas, Jussi: Spectroscopic studies of atoms and small molecules isolated in rare gas solids: photodissociation and thermal reactions. (53 pp.) 2006
118. Busi, Sara: Synthesis, characterization and thermal properties of new quaternary ammonium compounds: new materials for electrolytes, ionic liquids and complexation studies. (102 pp.) 2006
119. Mäntykoski, Keijo: PCBs in processes, products and environment of paper mills using wastepaper as their raw material. (73 pp.) 2006
120. Laamanen, Pirkko-Leena: Simultaneous determination of industrially and environmentally relevant aminopolycarboxylic and hydroxycarboxylic acids by capillary zone electrophoresis. (54 pp.) 2007
121. Salmela, Maria: Description of oxygen-alkali delignification of kraft pulp using analysis of dissolved material. (71 pp.) 2007
122. Lehtovaara, Lauri: Theoretical studies of atomic scale impurities in superfluid ^{4}He. (87 pp.) 2007
123. Rautiainen, J. Mikko: Quantum chemical calculations of structures, bonding, and spectroscopic properties of some sulphur and selenium iodine cations. (71 pp.) 2007
124. Nummelin, Sami: Synthesis, characterization, structural and

retrostructural analysis of self-assembling pore forming dendrimers. (286 pp.) 2008

125. Sopo, Harri: Uranyl(VI) ion complexes of some organic aminobisphenolate ligands: syntheses, structures and extraction studies. (57 pp.) 2008
126. Valkonen, Arto: Structural characteristics and properties of substituted cholanoates and *N*-substituted cholanamides. (80 pp.) 2008
127. Lähde, Anna: Production and surface modification of pharmaceutical nano- and microparticles with the aerosol flow reactor. (43 pp.) 2008
128. Beyeh, Ngong Kodiah: Resorcinarenes and their derivatives: synthesis, characterization and complexation in gas phase and in solution. (75 pp.) 2008
129. Välisaari, Jouni, Lundell, Jan (Eds.): Kemian opetuksen päivät 2008: uusia oppimisympäristöjä ja ongelmalähtöistä opetusta. (118 pp.) 2008
130. Myllyperkiö, Pasi: Ultrafast electron transfer from potential organic and metal containing solar cell sensitizers. (69 pp.) 2009
131. Käkölä, Jaana: Fast chromatographic methods for determining aliphatic carboxylic acids in black liquors. (82 pp.) 2009
132. Koivukorpi, Juha: Bile acid-arene conjugates: from photoswitchability to cancer cell detection. (67 pp.) 2009
133. Tuuttila, Tero: Functional dendritic polyester compounds: synthesis and characterization of small bifunctional dendrimers and dyes. (74 pp.) 2009
134. Salorinne, Kirsi: Tetramethoxy resorcinarene based cation and anion receptors: synthesis, characterization and binding properties. (79 pp.) 2009
135. Rautiainen, Riikka: The use of first-thinning Scots pine (*Pinus sylvestris*) as fiber raw material for the kraft pulp and paper industry. (73 pp.) 2010
136. Ilander, Laura: Uranyl salophens: synthesis and use as ditopic receptors. (199 pp.) 2010
137. Kiviniemi, Tiina: Vibrational dynamics of iodine molecule and its complexes in solid krypton - Towards coherent control of bimolecular reactions? (73 pp.) 2010
138. Ikonen, Satu: Synthesis, characterization and structural properties of various covalent and non-covalent bile acid derivatives of N/O-heterocycles and their precursors. (105 pp.) 2010
139. Siitonen, Anni: Spectroscopic studies of semiconducting single-walled carbon nanotubes. (56 pp.) 2010
140. Raatikainen, Kari: Synthesis and structural studies of piperazine cyclophanes – Supramolecular systems through Halogen and Hydrogen bonding and metal ion coordination. (69 pp.) 2010
141. Leivo, Kimmo: Gelation and gel properties of two- and three-component Pyrene based low molecular weight organogelators. (116 pp.) 2011
142. Martiskainen, Jari: Electronic energy transfer in light-harvesting complexes isolated from *Spinacia oleracea* and from three

photosynthetic green bacteria *Chloroflexus aurantiacus*, *Chlorobium tepidum*, and *Prosthecochloris aestuarii*. (55 pp.) 2011

143. Wichmann, Oula: Syntheses, characterization and structural properties of [O,N,O,X´] aminobisphenolate metal complexes. (101 pp.) 2011
144. Ilander, Aki: Development of ultrasound-assisted digestion methods for the determination of toxic element concentrations in ash samples by ICP-OES. (58 pp.) 2011
145. The Combined XII Spring Meeting of the Division of Synthetic Chemistry and XXXIII Finnish NMR Symposium. Book of Abstracts. (90 pp.) 2011
146. Valto, Piia: Development of fast analysis methods for extractives in papermaking process waters. (73 pp.) 2011
147. Andersin, Jenni: Catalytic activity of palladium-based nanostructures in the conversion of simple olefinic hydro- and chlorohydrocarbons from first principles. (78 pp.) 2011
148. Aumanen, Jukka: Photophysical properties of dansylated poly(propylene amine) dendrimers. (55 pp.) 2011
149. Kärnä, Minna: Ether-functionalized quaternary ammonium ionic liquids – synthesis, characterization and physicochemical properties. (76 pp.) 2011
150. Jurček, Ondřej: Steroid conjugates for applications in pharmacology and biology. (57 pp.) 2011
151. Nauha, Elisa: Crystalline forms of selected Agrochemical actives: design and synthesis of cocrystals. (77 pp.) 2012
152. Ahkola, Heidi: Passive sampling in monitoring of nonylphenol ethoxylates and nonylphenol in aquatic environments. (92 pp.) 2012
153. Helttunen, Kaisa: Exploring the self-assembly of resorcinarenes: from molecular level interactions to mesoscopic structures. (78 pp.) 2012
154. Linnanto, Juha: Light excitation transfer in photosynthesis revealed by quantum chemical calculations and exiton theory. (179 pp.) 2012
155. Roiko-Jokela, Veikko: Digital imaging and infrared measurements of soil adhesion and cleanability of semihard and hard surfaces. (122 pp.) 2012
156. Noponen, Virpi: Amides of bile acids and biologically important small molecules: properties and applications. (85 pp.) 2012
157. Hulkko, Eero: Spectroscopic signatures as a probe of structure and dynamics in condensed-phase systems – studies of iodine and gold ranging from isolated molecules to nanoclusters. (69 pp.) 2012
158. Lappi, Hanna: Production of Hydrocarbon-rich biofuels from extractives-derived materials. (95 pp.) 2012
159. Nykänen, Lauri: Computational studies of Carbon chemistry on transition metal surfaces. (76 pp.) 2012
160. Ahonen, Kari: Solid state studies of pharmaceutically important molecules and their derivatives. (65 pp.) 2012

161. Pakkanen, Hannu: Characterization of organic material dissolved during alkaline pulping of wood and non-wood feedstocks. (76 pp.) 2012
162. Moilanen, Jani: Theoretical and experimental studies of some main group compounds: from closed shell interactions to singlet diradicals and stable radicals. (80 pp.) 2012
163. Himanen, Jatta: Stereoselective synthesis of Oligosaccharides by *De Novo* Saccharide welding. (133 pp.) 2012
164. Bunzen, Hana: Steroidal derivatives of nitrogen containing compounds as potential gelators. (76 pp.) 2013
165. Seppälä, Petri: Structural diversity of copper(II) amino alcohol complexes. Syntheses, structural and magnetic properties of bidentate amino alcohol copper(II) complexes. (67 pp.) 2013
166. Lindgren, Johan: Computational investigations on rotational and vibrational spectroscopies of some diatomics in solid environment. (77 pp.) 2013
167. Giri, Chandan: Sub-component self-assembly of linear and non-linear diamines and diacylhydrazines, formulpyridine and transition metal cations. (145 pp.) 2013
168. Riisiö, Antti: Synthesis, Characterization and Properties of Cu(II)-, Mo(VI)- and U(VI) Complexes With Diaminotetraphenolate Ligands. (51 pp.) 2013
169. Kiljunen, Toni (Ed.): Chemistry and Physics at Low Temperatures. Book of Abstracts. (103 pp.) 2013
170. Hänninen, Mikko: Experimental and Computational Studies of Transition Metal Complexes with Polydentate Amino- and Aminophenolate Ligands: Synthesis, Structure, Reactivity and Magnetic Properties. (66 pp.) 2013
171. Antila, Liisa: Spectroscopic studies of electron transfer reactions at the photoactive electrode of dye-sensitized solar cells. (53 pp.) 2013
172. Kemppainen, Eeva: Mukaiyama-Michael reactions with α-substituted acroleins – a useful tool for the synthesis of the pectenotoxins and other natural product targets. (190 pp.) 2013
173. Virtanen, Suvi: Structural Studies of Dielectric Polymer Nanocomposites. (49 pp.) 2013
174. Yliniemelä-Sipari, Sanna: Understanding The Structural Requirements for Optimal Hydrogen Bond Catalyzed Enolization – A Biomimetic Approach.(160 pp.) 2013
175. Leskinen, Mikko V: Remote β-functionalization of β'-keto esters. (105 pp.) 2014
176. 12th European Conference on Research in Chemistry Education (ECRICE2014). Book of Abstracts. (166 pp.) 2014
177. Peuronen, Anssi: N-Monoalkylated DABCO-Based N-Donors as Versatile Building Blocks in Crystal Engineering and Supramolecular Chemistry. (54 pp.) 2014
178. Perämäki, Siiri: Method development for determination and recovery of rare earth elements from industrial fly ash. (88 pp.) 2014

179. Chernyshev, Alexander, N.: Nitrogen-containing ligands and their platinum(IV) and gold(III) complexes: investigation and basicity and nucleophilicity, luminescence, and aurophilic interactions. (64 pp.) 2014
180. Lehto, Joni: Advanced Biorefinery Concepts Integrated to Chemical Pulping. (142 pp.) 2015
181. Tero, Tiia-Riikka: Tetramethoxy resorcinarenes as platforms for fluorescent and halogen bonding systems. (61 pp.) 2015
182. Löfman, Miika: Bile acid amides as components of microcrystalline organogels. (62 pp.) 2015
183. Selin, Jukka: Adsorption of softwood-derived organic material onto various fillers during papermaking. (169 pp.) 2015
184. Piisola, Antti: Challenges in the stereoselective synthesis of allylic alcohols. (210 pp.) 2015
185. Bonakdarzadeh, Pia: Supramolecular coordination polyhedra based on achiral and chiral pyridyl ligands: design, preparation, and characterization. (65 pp.) 2015
186. Vasko, Petra: Synthesis, characterization, and reactivity of heavier group 13 and 14 metallylenes and metalloid clusters: small molecule activation and more. (66 pp.) 2015
187. Topić, Filip: Structural Studies of Nano-sized Supramolecular Assemblies. (79 pp.) 2015
188. Mustalahti, Satu: Photodynamics Studies of Ligand-Protected Gold Nanoclusters by using Ultrafast Transient Infrared Spectroscopy. (58 pp.) 2015
189. Koivisto, Jaakko: Electronic and vibrational spectroscopic studies of gold-nanoclusters. (63 pp.) 2015
190. Suhonen, Aku: Solid state conformational behavior and interactions of series of aromatis oligoamide foldamers. (68 pp.) 2016
191. Soikkeli, Ville: Hydrometallurgical recovery and leaching studies for selected valuable metals from fly ash samples by ultrasound-assisted extraction followed by ICP-OES determination. (107 pp.) 2016
192. XXXVIII Finnish NMR Symposium. Book of Abstracts. (51 pp.) 2016
193. Mäkelä, Toni: Ion Pair Recognition by Ditopic Crown Ether Based bis-Urea and Uranyl Salophen Receptors. (75 pp.) 2016
194. Lindholm-Lehto, Petra: Occurrence of pharmaceuticals in municipal wastewater treatment plants and receiving surface waters in Central and Southern Finland. (98 pp.) 2016
195. Härkönen, Ville: Computational and Theoretical studies on Lattice Thermal conductivity and Thermal properties of Silicon Clathrates. (89 pp.) 2016
196. Tuokko, Sakari: Understanding selective reduction reactions with heterogeneous Pd and Pt: climbing out of the black box. (85 pp.) 2016
197. Nuora, Piia: Monitapaustutkimus LUMA-Toimintaan liittyvissä oppimisympäristöissä tapahtuvista kemian oppimiskokemuksista. (171 pp.) 2016

198. Kumar, Hemanathan: Novel Concepts on The Recovery of By-Products from Alkaline Pulping. (61 pp.) 2016
199. Arnedo-Sánchez, Leticia: Lanthanide and Transition Metal Complexes as Building Blocks for Supramolecular Functional Materials. (227 pp.) 2016
200. Gell, Lars: Theoretical Investigations of Ligand Protected Silver Nanoclusters. (134 pp.) 2016
201. Vaskuri, Juhani: Oppiennätyksistä opetussuunnitelman perusteisiin - lukion kemian kansallisen opetussuunnitelman kehittyminen Suomessa vuosina 1918-2016. (314 pp.) 2017
202. Lundell Jan, Kiljunen Toni (Eds.): 22nd Horizons in Hydrogen Bond Research. Book of Abstracts. 2017
203. Turunen, Lotta: Design and construction of halogen-bonded capsules and cages. (61 pp.) 2017
204. Hurmalainen, Juha: Experimental and computational studies of unconventional main group compounds: stable radicals and reactive intermediates. (88 pp.) 2017
205. Koivistoinen Juha: Non-linear interactions of femtosecond laser pulses with graphene: photo-oxidation, imaging and photodynamics. (68 pp.) 2017
206. Chen, Chengcong: Combustion behavior of black liquors: droplet swelling and influence of liquor composition. (39 pp.) 2017
207. Mansikkamäki, Akseli: Theoretical and Computational Studies of Magnetic Anisotropy and Exchange Coupling in Molecular Systems. (190 p. + included articles) 2018.
208. Tatikonda, Rajendhraprasad: Multivalent N-donor ligands for the construction of coordination polymers and coordination polymer gels. (62 pp.) 2018
209. Budhathoki, Roshan: Beneficiation, desilication and selective precipitation techniques for phosphorus refining from biomass derived fly ash. (64 pp.) 2018
210. Siitonen, Juha: Synthetic Studies on 1-azabicyclo[5.3.0]decane Alkaloids. (140 pp.) 2018
211. Ullah, Saleem: Advanced Biorefinery Concepts Related to Non-wood Feedstocks. (57 pp.) 2018
212. Ghalibaf, Maryam: Analytical Pyrolysis of Wood and Non-Wood Materials from Integrated Biorefinery Concepts. (106 pp.) 2018

DEPARTMENT OF CHEMISTRY, UNIVERSITY OF JYVÄSKYLÄ
DISSERTATIONS PUBLISHED IN THE JYU DISSERTATIONS RESEARCH SERIES

1. Bulatov, Evgeny: Synthetic and structural studies of covalent and non-covalent interactions of ligands and metal center in platinum(II) complexes containing 2,2′-dipyridylamine or oxime ligands. (58 pp.) 2019. JYU Dissertations 70.
2. Annala, Riia: Conformational Properties and Anion Complexes of Aromatic Oligoamide Foldamers. (80 pp.) 2019. JYU Dissertations 84.
3. Isoaho, Jukka Pekka: Dithionite Bleaching of Thermomechanical Pulp - Chemistry and Optimal Conditions. (73 pp.) 2019. JYU Dissertations 85.
4. Nygrén, Enni: Recovery of rubidium from power plant fly ash. (98 pp.) 2019. JYU Dissertations 136.
5. Kiesilä, Anniina: Supramolecular chemistry of anion-binding receptors based on concave macromolecules. (68 pp.) 2019. JYU Dissertations 137.
6. Sokolowska, Karolina: Study of water-soluble p-MBA-protected gold nanoclusters and their superstructures. (60 pp.) 2019. JYU Dissertations 167.
7. Lahtinen, Elmeri: Chemically Functional 3D Printing: Selective Laser Sintering of Customizable Metal Scavengers. (71 pp.) 2019. JYU Dissertations 175.
8. Larijani, Amir: Oxidative reactions of cellulose under alkaline conditions. (102 pp.) 2020. JYU Dissertations 217.
9. Kolari, Kalle: Metal-metal contacts in late transition metal polymers. (60 pp.) 2020. JYU Dissertations 220.
10. Kauppinen, Minttu: Multiscale computational investigation of catalytic properties of zirconia supported noble metals. (87 pp.) 2020. JYU Dissertations 231.
11. Ding, Xin: Halogen Bond in Crystal Engineering: Structural Studies on Crystals with Ruthenium Centered Complexes and 1-(4-Pyridyl)-4-thiopyridine Zwitterion as Halogen Bond Acceptors. (59 pp.) 2020. JYU Dissertations 323.
12. Neuvonen, Antti: Toward an Understanding of Hydrogen-Bonding Bifunctional Organocatalyst Conformations and Their Activity in Asymmetric Mannich Reactions. (77 pp.) 2020. JYU Dissertations 336.
13. Kortet, Sami: 2,5-Diarylpyrrolidines and Pyroglutamic-Acid-Derived 2-Diarylmethyl-5-Aryl-Pyrrolidines: Their Synthesis and Use in Asymmetric Synthesis. (221 pp.) 2020. JYU Dissertations 337.
14. Saarnio, Ville: Fluorescent probes, noble metal nanoparticles and their nanocomposites: detection of nucleic acids and other biological targets. (80 pp.) 2021. JYU Dissertations 361.
15. Chernysheva, Maria: σ-hole interactions: the effect of the donors and acceptors nature in selenoureas, thioureas, halogenated species, substituted benzenes, and their adducts. (72 pp.) 2021. JYU Dissertations 370.
16. Bulatova, Margarita: Noncovalent interactions as a tool for supramolecular self-assembly of metallopolymers. (62 pp.) 2021. JYU Dissertations 377.